The image features a stylized profile of a human head on the right side, composed of four overlapping, wavy lines in shades of teal, green, orange, and yellow. The lines are thicker at the top and bottom, tapering towards the middle. The background is split horizontally into a light blue upper half and a white lower half. The title text is positioned on the left side, overlapping the light blue background.

**Development of  
Raman spectroscopy  
tools for surgery  
guidance in  
head & neck oncology**

**Elisa M. L. Barroso**



Development of Raman  
spectroscopy  
tools for surgery guidance in  
head & neck oncology

Elisa M. L. Barroso

Development of Raman Spectroscopy Tools for Surgery Guidance in Head & Neck Oncology

ISBN: 978-94-6299-946-6

Cover Illustrations: Inês Santos and Elisa Barroso

Printing: Ridderprint

Copyright©2018 Elisa Maria Lamego Barroso

All rights reserved. No part of the material projected by this copyright notice may be reproduced or utilized in any form or by any other means, electronic or mechanical, including photocopying, recording or by any other information storage and retrieval system, without the prior permission of the author.

# **Development of Raman Spectroscopy Tools for Surgery Guidance in Head & Neck Oncology**

De ontwikkeling van Raman spectroscopische hulpmiddelen voor  
chirurgische begeleiding in de hoofd-hals oncologie

## **Thesis**

to obtain the degree of doctor from  
Erasmus University Rotterdam  
by command of the rector magnificus

Prof. dr. H.A.P. Pols

and in accordance with the decision of the Doctorate Board.

The public defence shall be held on  
Wednesday, 30<sup>th</sup> of May 2018 at 11h30  
by

**Elisa Maria Lamego Barroso**

born in Vila Nova de Famalicão, Portugal32

**Erasmus University Rotterdam**



## **Doctoral Committee**

**Promoter:** Prof. dr. E. B. Wolvius

**Other members:** Prof. dr. R. J. Baatenburg de Jong

Prof. dr. J. M. Kros

Prof. dr. N. Stone

**Co-promoters:** dr. S. Koljenović

dr. G. Puppels



# *Contents*





CHAPTER 1 .....	11
<i>General introduction</i> .....	11
1.1 <i>Surgical Oncology</i> .....	13
1.2 <i>Head and neck cancer: epidemiology and treatment</i> .....	14
1.3 <i>Evolving techniques for intra-operative guidance of oral surgical oncology</i> .....	18
1.3.1 Fluorescence imaging technology.....	18
1.3.2 Narrow band imaging (NBI).....	20
1.3.3 Confocal microscopy (CFM).....	21
1.3.4 High resolution microendoscopy (HRME).....	21
1.3.5 Ultrasound imaging.....	22
1.3.6 Optical coherence tomography (OCT).....	23
1.3.7 Raman spectroscopy.....	24
1.4 <i>This thesis</i> .....	30
CHAPTER 2.....	39
<i>Raman spectroscopy for cancer diagnostics and cancer surgery guidance: translation to the clinics</i> .....	39
CHAPTER 3.....	85
<i>Discrimination between oral cancer and healthy tissue based on water content determined by Raman spectroscopy</i> .....	85
CHAPTER 4.....	105
<i>Characterization and subtraction of luminescence background signals in high- wavenumber Raman spectra of human tissue</i> .....	105
CHAPTER 5.....	129
<i>Water concentration analysis by Raman spectroscopy to determine the location of the tumor border in oral cancer surgery</i> .....	129
CHAPTER 6.....	149
<i>Raman spectroscopy for assessment of bone resection margins in mandibulectomy for oral cavity squamous cell carcinoma</i> .....	149
CHAPTER 7.....	171

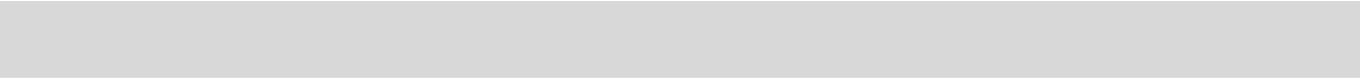
<i>Translation to the clinics:</i> .....	171
<i>development of a fiber-optic Raman needle probe for intra-operative assessment of surgical margins in oral cancer based on water concentration</i> .....	171
CHAPTER 8.....	189
<i>General discussion &amp; Outlook</i> .....	189
<i>General discussion</i> .....	191
<i>Outlook</i> .....	194
Raman pathology system for assessment of bone resection surfaces .....	194
Raman pathology system for assessment of soft tissue resection .....	195
CHAPTER 9 .....	201
<i>Summary, Sumário, Samenvatting</i> .....	201
CHAPTER 10 .....	211
<i>About the author</i> .....	211
<i>Biography</i> .....	213
<i>List of publications</i> .....	215
<i>PhD Portfolio</i> .....	216
<i>Curriculum Vitae</i> .....	218







# ***CHAPTER 1***



## ***General introduction***



## 1.1 Surgical Oncology

Surgery was, for an extended period in the past, the only treatment for cancer. Only in the last century non-surgical treatments have been used as adjunct modalities (chemotherapy and radiation therapy) or more rarely (for example, in case of leukemia), as an alternative to surgery. Although nowadays non-surgical treatments are being used, surgery is still the mainstay treatment for solid tumors.

The goal of surgical treatment is the resection of all malignant tissue with an adequate resection margin while preserving important adjacent healthy anatomical structures, and therefore maintaining their functionality. In surgical oncology, the resection margin is the smallest distance between the tumor border and the resection cut surface. The length of the needed resection margin depends on the type of tumor and its location in the body.

Unfortunately, resection margins are often positive, which means that, after surgery, tumor is present at the resection surface of the specimen, and therefore, it may also be in the wound bed of the patient. The presence of residual tumor is associated with poor survival and need for additional surgery, adjuvant chemotherapy, radiation therapy, or a combination of these. For that reason, achieving adequate resection margins is decisive for disease control and survival of the patients. However, it is challenging to attain an adequate resection. Currently, the assessment of the resection margins is based on palpation, visual inspection, and, when possible, evaluation of intra-operative frozen sections (1). Palpation and visual inspection are subjective and have low sensitivity and specificity. Evaluation of frozen sections is a much more accurate diagnostic technique, but it is labor intensive and limited to a few inspection sites. Therefore, there is a need for intra-operative guidance (IOG) tools that can be used to inspect the margins with high spatial resolution, and in real-time. Currently, there are no universal objective intra-operative guidance tools ready for use but techniques like intra-operative real-time MRI, intra-operative ultrasound, intra-operative OCT, fluorescence and Raman spectroscopy are being explored for IOG already in operating room environments (2-16). These techniques have been mainly investigated for brain cancer surgery and breast cancer surgery (9-16). Obviously, this is useful for all kinds of cancer surgeries, and especially for head and neck surgical oncology. Head and neck cancer can damage many important functional systems and sensory organs. Due to the complexity of the anatomical structures of the head and neck region, there is a fine balance between remaining function, physical appearance and adequate margins. Therefore, the development and implementation of an IOG tool for head and neck surgical oncology is a crucial step towards improvement of head and neck surgical outcomes (17,18).

The goal of this thesis was to investigate how high-wavenumber Raman spectroscopy can be used as an IOG tool for head and neck surgical oncology.

This chapter serves as an introduction to this research question and provides background information on the medical application field and the various IOG tools that are being developed, with a special focus on Raman spectroscopy. In subchapter 1.2, the epidemiology and the standard treatment method of head and neck cancer is described. The state-of-the-art regarding the techniques that are being investigated for intra-operative assessment of head and neck cancers are described in subchapter 1.3, with a focus on the advantages, disadvantages and results obtained with these techniques. The Raman effect, the history of Raman spectroscopy and the instrumentation used for Raman spectroscopy are described in detail in the subchapter 1.3.7. Finally, the subchapter 1.4 describes the scope of this thesis.

## **1.2 Head and neck cancer: epidemiology and treatment**

Every year, >680,000 new cases of head and neck cancer are diagnosed worldwide. The mortality rate of head and neck cancers is >370,000 (22). As head and neck cancers are included: cancer of the oral cavity (OCC), nasopharynx, oropharynx, hypopharynx, and the larynx. More than 90% of head and neck cancers are squamous cell carcinomas that originate from the mucosa of the oral cavity, oropharynx and larynx (23).

Oral cavity squamous cell carcinoma (OCSCC) is the most frequent type of head and neck cancer (22). The macroscopic aspect of an advanced OCSCC of the tongue is shown in the figure 1.



**Figure 1. OCSCC of the tongue.**

Worldwide, 300,000 new cases of OCSCC are diagnosed per year (22). The mortality of OCSCC is high (145,000 deaths are registered worldwide) (22,24,25). These numbers demonstrate that OCSCC is a major worldwide health issue. The most cited risk factor for developing OCSCC is the use of tobacco, which raises 3-fold the risk of developing OCSCC. Concomitant alcohol consumption increases the risk 10- to 15-fold (26). The use of smokeless tobacco also increases the risk of developing OCSCC (27). Furthermore, genetic syndromes, like Fanconi anemia and dyskeratosis congenita, are also strongly related with the development of OCSCC.

For OCSCC, the average 5-year survival is between 50-60%. Depending on stage, age, race, comorbidity, and location of the tumor in the oral cavity, the 5-year survival can vary from 10% to 82% (28,29). In addition, the presence of nodal metastases (spread of tumor cells to regional lymph nodes) can drastically affect the survival, reducing it by 50% (30,31).

Local-regional control (control of cancer spread from the primary tumor subsite) is especially difficult to achieve for tongue (even in early stage tumors) compared with the oral subsites of the oral cavity. This difficulty exists due to: lack of anatomic barriers, which could avoid the cancer spread, robust lymphatic drainage, and the capacity for contralateral spread (32).

The standard treatment options of OCSCC are: surgery, chemotherapy, radiotherapy, or a combination of these modalities.

In Erasmus University Medical Center Rotterdam, a team of different specialists (medical oncologists, radiation oncologists, head and neck surgeons, pathologists and radiologists) weekly discuss the best management option for all the head and neck patients. If, for a particular patient, surgery is selected, the main goal of the oncological surgery will be to achieve an adequate tumor resection with acceptable remaining function of the anatomical structures and appearance. According to the Royal College of Pathologists (33), the distance between tumor border and the nearest resection surface determines the adequacy of the surgical procedure. This distance is measured in millimeters and is called resection margin. A resection margin can be classified as clear (>5 mm), close (1 to 5 mm) and positive (<1 mm) (33). Clear margins are regarded as adequate, close and positive margins as inadequate. Achieving adequate resection margins is critically important because, if the tumor is not completely removed, there is a high risk of local recurrence and decrease of survival (34-39). When the margins are inadequate (i.e. <5 mm) adjuvant therapy (chemotherapy and/or radiation therapy) or re-resection is necessary. These therapies have a negative effect on patient morbidity. Therefore,

improvement of disease control, survival and patient morbidity is directly correlated with adequate resection margins (40, 41,34-38).

During resection of the tumor, surgeons rely on visual inspection and palpation, but it is often very difficult to remove the tumor in remote anatomical locations in close vicinity to critical structures, even in expert hands. These challenges are frequently encountered in the head and neck region, because of the complexity and location of this region in respect to the location of vital structures, such as cranial nerves and major vessels supplying the brain. The lack of reliable intra-operative guidance and the proximity of tumors to vital structures are the common causes of inadequate tumor resection.

Earlier, Smits et al. (2015) have reported the surgical results obtained in two Dutch centers (Erasmus University Medical Center Rotterdam and Leiden University Medical Center). For OCSCC surgery adequate resection margins were obtained in only 15% of the cases (40). A similar result was reported by the Harborview Medical Center and the University of Washington Medical Center in Seattle (USA) (41). Clearly, visual inspection and palpation of the tumor and healthy surrounding tissue by the surgeon are insufficient to warrant adequate tumor resection.

Intra-operative assessment (IOA) can be performed on the resection surface of the specimen or on the wound bed of the patient. IOA of the specimen's resection surface (i.e. specimen driven approach, see figure 2) has been reported to be superior to the assessment of the wound bed (i.e. defect driven approach).

Several studies indicate that specimen driven IOA leads to a higher surgical success rate and increase of patient survival than defect-driven or no IOA at all (38,42-44). In Erasmus University Medical Center Rotterdam, specimen driven IOA has been adopted since 2013. Additionally, the eighth edition of the American Joint Committee of Cancer (AJCC) also recommends the specimen driven IOA (45). During head and neck surgery, IOA of resection margins can be done by means of a frozen section procedure (37). This procedure, in which the pathologist performs microscopic evaluation of a piece of suspicious tissue, is currently the gold standard of intra-operative diagnostics (46-48). The main limitation of the frozen section procedure is that only a fraction of the resection margins can be investigated. The method is prone to sampling errors, which often leads to false negative results (40,46). Ideally, not only a small portion of the resection margin should be evaluated but the entire resection surface should be evaluated intra-operatively, which requires an objective and fast technology. Moreover, a study performed by McIntosh *et al* (2015) described that frozen section analysis is also limited by histologic disruption introduced by freezing of the tissue. The same study also explains that certain

tissues, such as fat and bone, do not freeze well and are difficult to cut with a microtome (instrument used to produce the thin sections). Intra-operative frozen sections consultation for bone specimen is particularly challenging. These technically difficult frozen sections can lead to an inadequate slide for review. These factors contribute to a certain degree of diagnostic inaccuracy, and as a result the frozen section procedure is not very effective in improving surgical success rate (49).

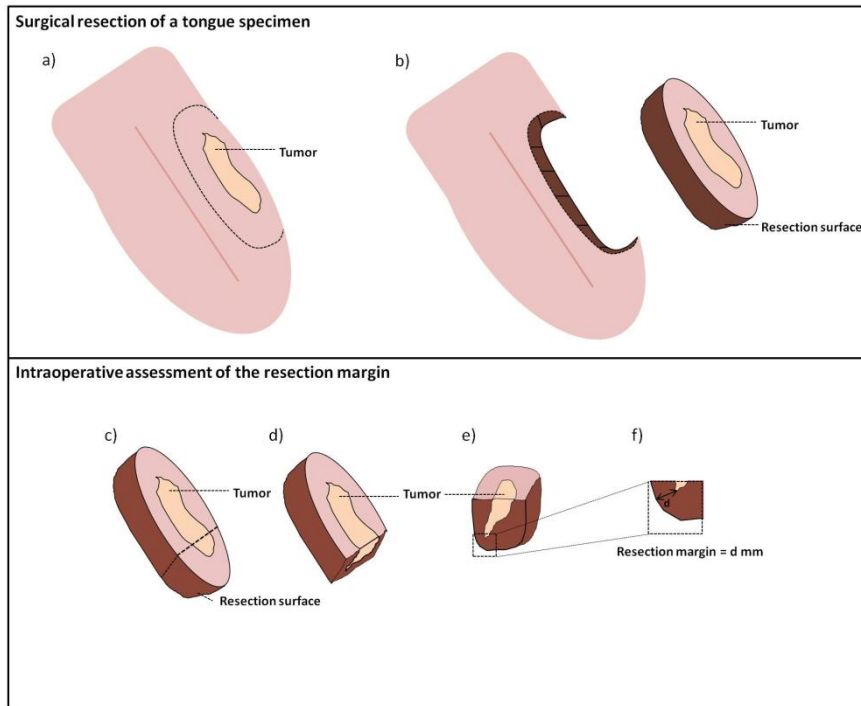


**Figure 2. Surgical resection of a OCSCC tongue specimen and the respective specimen driven IOA. Surgeon delineates where the resection will take place. b) Resection is made. c) Pathologist indicates where there is suspicion of an inadequate resection margin. e) A cross section is performed on the suspicious region. f) The resection margin is measured (d mm), which is the smallest distance between the tumor border and the resection surface.**

This clarifies that there is need for a new technique for assessment of the margin status and that does not have the limitations of the current IOA procedure. The technique should be fast enough to allow the inspection of whole resection planes, should be objective, and should not be only applicable to soft tissue but also to bone.

The high incidence, high mortality rate, high number of inadequate resections and the lack of an objective IOG tool in head and neck surgical oncology demonstrate that there is room for improvement and that this thesis may have an impact in the future of the head and neck surgical oncology field.

## **1.3 Evolving techniques for intra-operative guidance of oral surgical oncology**

Various techniques like imaging-based modalities, imprint cytology, and optical techniques have been investigated for intra-operative use in surgical oncology (50-65). The techniques that are being applied specifically, for intra-operative assessment of the resection margins of patients that underwent OCSCC surgery were recently reviewed by Ravi *et al* and Miles *et al* (48,49). The current technologies being tested for intra-operative guidance for margin control in head and neck surgery are: tissue auto-fluorescence, near infrared imaging, fluorescence imaging, narrow band imaging, confocal microscopy, high resolution microendoscopy, ultrasound imaging, optical coherence tomography, and Raman spectroscopy (19,20). These techniques and their results are described in the following sub-chapters.

### **1.3.1 Fluorescence imaging technology**

Fluorescence imaging technologies; such as: tissue auto-fluorescence, near infrared imaging and fluorescent probe imaging systems; have been used for the screening, detection, and delineation of head and neck squamous cell carcinoma (66-74).

#### *Tissue auto-fluorescence*

Auto-fluorescence is a well-known phenomenon that is caused by the presence of endogenous fluorophores in biological samples. Auto-fluorescence imaging is an optical technique that measures the intrinsic fluorescence emitted by fluorophores that are present in the tissue (e.g. flavins, collagen or hemoglobin). Tissues are illuminated with a short-wavelength light source and the fluorescence emitted is captured in real-time. Differences in emitted fluorescence can be used for lesion detection and/or characterization (75).

Several research groups have been investigating the use of auto-fluorescence imaging for intra-operative margin control.

Klatt *et al*, has described the method as having potential for head and neck oncologic surgery. This conclusion was based on time-resolved auto-fluorescence measurements in tumor and in healthy tissue of the oral cavity *ex-vivo*. Klatt *et al*, observed that the fractal dimension of malignant tissue was significantly higher than the fractal dimension of healthy mucosa (66).

Based on a retrospective study, Poh *et al* reported that patients who underwent surgery with fluorescence visualization (VELscope) for high-grade dysplasia or oral carcinoma had a dramatic reduction in the 3-year local recurrence rate. Although, they reported that fluorescence imaging is an excellent method to guide surgical resection, they have also mentioned that this technique is somewhat limited by issues related to specificity. Phase 3 clinical trials of the VELscope have demonstrated that the specificity of this technique is extremely variable. They have observed that not only malignant tissue exhibits decreased auto-fluorescence, but a variety of other tissue conditions may also exhibit less fluorescence signal, such as inflammation, keratosis, and benign lesions (67).

### *Near infrared imaging*

Biological tissue has a minimum absorption coefficient when using near infrared light (650 to 900nm). Absorption of electromagnetic radiation is characterized by the transfer of energy of a photon into internal energy of the absorber, for example as thermal energy. The near infrared optical imaging window also allows minimal light scattering, minimal nonspecific fluorescence, and an increase of the penetration of the light in the tissue. These advantages contribute to the use of NIR in applications for image-guided surgery (76,77).

In most head and neck squamous cell carcinomas the epidermal growth factor receptor (EGFR) is expressed. Cetuximab is a known therapeutic antibody that interacts with EGFR. Cetuximab has been combined with Cy 5.5 (fluorophore that has excitation at 678nm and emission at 703nm). This combination was used to guide surgical resections in head and neck mouse tumor models (78).

The production of the vascular endothelial growth factor (VEGF) is also up-regulated in tumor cells, which promotes angiogenesis. The conjugation of Cy 5.5 to bevacizumab (anti-VEGF antibody, for head and neck tumors) has also been tested in a mouse model and a study reported a sensitivity of 80.9% and a specificity of 91.7% (79).

Other different strategies have been proposed and tested in the optical imaging field of NIR light but, the clinical translation of the results is difficult. Pharmacokinetic studies are required for each fluorophore-conjugate. In addition, to use this system intra-operatively the development of better camera systems is necessary (77).

### *Fluorescence Probe imaging*

Tumor cells can be imaged using antibodies or ligands conjugated to an optically active fluorophore. The principal of fluorescence imaging is based on the signal-to-background ratio concept (equivalent to tumor-to-background ratio). The

conventional fluorescence imaging techniques use probes in the visible light spectrum (400-600nm). This is the main difference between the other two modalities.

For example, transferrin receptor (TfR), which is a cell-membrane internalizing receptor mainly responsible for iron sequestration, is overexpressed in many head and neck tumors. The conjugation of the TfR antibody to Alexa-488 (excitation at 494nm and emission at 519nm) has been used for non-invasive imaging of a head and neck tumor mouse model (80).

Some disadvantages are associated with the use of the conventional fluorescence imaging in the visible light spectrum. First, there is a relatively low tumor-to-background ratio, which is due to the relatively high-level of non-specific background. Additionally, there is another disadvantage related with the use of visible light: biological chromophores can limit the depth penetration of the light and increase the scattering of the light, such as hemoglobin. Kerweeer *et al* have mentioned that the light properties of this spectrum are not sufficient to achieve the required sensitivity and specificity for image-guided surgery (77).

### **1.3.2 Narrow band imaging (NBI)**

The narrow band imaging system has been developed to improve the quality of endoscopic images and to enhance the visualization of microvasculature on mucosal surfaces. NBI consists of a sequential electronic endoscope system and a light source unit equipped with narrow-band filters. The light source unit has a xenon lamp and a filter disk that is mounted with three interference filters (red:485-515nm, green:430-460nm and blue:400-430nm filters). Longer wavelengths propagate more deeply, while shorter wavelengths propagate to the shallow region of the mucosa. The system takes advantage of the absorption peak of haemoglobin. Therefore, NBI can image the surface characteristics of mucosal tissue as well as vascular differences between tissues. In general, areas of non-dysplastic tissue have fine capillary patterns with normal size and distribution. Areas with high-grade dysplasia have an abnormal capillary pattern (increased number, size and dilation) (81).

NBI has been investigated to guide head and neck cancer surgery. Orita *et al* used NBI to delineate intra-operative margins in a 62-year-old patient that underwent partial hypopharyngectomy. Based on the satisfactory results the authors hypothesized that this system could be used for intra-operative assessment of the resection margins (81). Another study, conducted by Tirelli *et al*, reported that NBI was used after macroscopic margin delineation. For this study, NBI showed a sensitivity of 100% and a specificity of approximately 88% (82). NBI has also been used in combination with transoral robotic surgery (TORS) to reduce the positive

margin rate. Vicini *et al*, has performed a retrospective study to compare the results obtained from 32 patients (that underwent TORS with intra-operative NBI evaluation) with the results of 21 patients (that underwent standard TORS with white light evaluation). The rate of negative superficial lateral margins in NBI-TORS group and the rate of the standard TORS group was 87.9% and 57.9%, respectively. In this study the specificity of NBI was 66.7% (83). Garafolo *et al*, compared a cohort of 82 patients that underwent cordectomies for laryngeal malignancy using lesion delineation with NBI and a cohort of patients that had a similar procedure but with standard microscopic evaluation during the surgery. Positive superficial margins were compared. The rate of positive margins for the cohort group that used NBI was 3.6%, while for the control group the rate of positive margins was 23.7% (84).

In all the previous studies described the authors have concluded that NBI of head and neck lesions dramatically decreased the rate of final positive superficial margins. However, NBI specificity varies with the endoscopic magnification system used and with the experience of the clinician that is responsible for the analysis of the images (83,84).

### 1.3.3 Confocal microscopy (CFM)

Confocal microscopy is a method for non-invasive imaging of superficial soft tissues. The confocal microscope consists of a source of light that is focused to a small 3D illuminated spot, also called as voxel (within the tissue). The light from this voxel is collected by the detector (passing through a pinhole), which forms the pixel. To look at large areas or volumes of tissue, the voxel is scanned in two dimensions (optical sectioning). The optical sections are parallel to the tissue surface. Optical sections can be taken in depth by translating the microscope lens toward or away from the tissue. This technique allows imaging of sub-cellular structures (85,86).

CFM has been extensively applied in the field of dermatology to determine the margins of skin lesions (87). Although some studies have evaluated the use of CFM for detection of oral malignancy, the application of this technique in head and neck oncology is still limited. The limitations are: CFM systems are expensive, there are relatively few experts trained in image interpretation for the oral mucosa, and the large size of the equipment limits imaging to certain areas in the mouth (88).

### 1.3.4 High resolution microendoscopy (HRME)

HRME is a non-invasive technique that uses a fluorescence microscope coupled to a flexible fiber optic probe. This imaging technology obtains images in real-time of

tissue that is topically stained with a fluorescent nuclear contrast agent (more commonly, 0.01% proflavine) (89,90). This technique allows the visualization of nuclear and cellular morphology, including: epithelial architecture, cell nuclear morphology of and nuclear size, nuclear-to-cytoplasm ratio, and nuclear dispersion. This device has been validated for detection of head and neck squamous cell carcinoma ex-vivo (sensitivity of 98% and specificity of 92%) (91). A clinical trial has reported the ability of HRME to distinguish benign from malignant tissue in 33 patients with squamous cell carcinoma of the oral cavity. The mean accuracy of the trial was 95.1%, the mean sensitivity was 96% and the mean specificity was 95%. Although the authors of the clinical trial concluded that HRME had a high reliability to distinguish benign from malignant mucosa, they reported that some issues related to the image acquisition of inflammation, keratin debris, bleeding, and contrast artifacts happened. They also noted that there is a significant limitation of the technology, at the current time the technology is limited to a reduced surface imaging (50  $\mu\text{m}$ ) (20).

### **1.3.5 Ultrasound imaging**

Ultrasonic systems are another non-invasive real-time technology. The basic principle of ultrasound is the use of pulse-echo approach with a brightness-mode display. This approach involves transmitting small pulses of ultrasound echo from a transducer into the body. The ultrasound waves penetrate the tissues with different acoustic impedances. Some waves are reflected back to the transducer (echo signals), others continue penetrating the tissue. Echo signals are processed and combined to generate an image. Therefore, an ultrasound transducer works as a speaker (generating sound waves) as well as a microphone (receiving sound waves). The ultrasound pulse can be also called as ultrasound beam (92).

Ultrasonic systems have been used for the detection of tumor prior and during surgical resection. A study conducted by Yuen *et al*, used intraoral ultrasonography to document tumor thickness prior to resection. Results demonstrated that the accuracy of ultrasound in tumors from 3-15mm thick was >91%. Although the results were very promising, this study was performed as a pre-operative evaluation and not during the surgical procedure (93). Another study used ultrasonography prior to resection of T1-T2 tongue squamous cell carcinomas (tumor with <4 cm), who underwent a partial glossectomy (tongue resection). Histologic sectioning ultrasonographical tumor thickness was compared to the tumor histologic thickness and resulted a ratio of 91.4% to 98.2% (94). Tominaga *et al*, have used ultrasonography to control resection margins right after resecting the tumor. For the study the freshly excised specimen was immersed in a gelatine solution and ultrasound measurements were performed. An excellent correlation of the depth of the tumor measured with the ultrasound and the histologic depth of the tumor was

reported. This study demonstrated that the method allows a real-time assessment of adequacy of the resection margins (95). Also, Baek *et al* reported that intraoral ultrasonography in patients with T1-T2 tongue squamous cell carcinoma resulted in a more adequate deep margin when compared with conventional resection, which is only based in palpation and visual inspection (96).

Although, these studies illustrate the real advantage of the ultrasound imaging for assessment/control of the resection margins to ensure adequate deep margin resection, this technique is associated to some limitations. The effectiveness and accuracy of the technique relies on the experience and skill of the operator for image interpretation (93-96).

### 1.3.6 Optical coherence tomography (OCT)

OCT is a non-invasive imaging technology that has been used extensively in a variety of applications in the medical field. This technology is a light interference-based optical technique that allows 3D across sectional imaging within biological samples. The spatial resolution of this technique is high (1-15 $\mu$ m). Therefore, this technique is used to perform high-resolution cross-sectional imaging of the microstructure of tissues by measuring the echo time delay and magnitude of backscattered light. OCT is analogous to ultrasound imaging however, high image resolutions can be achieved in the OCT case. In an OCT system the light (low-coherence source) is split into two paths by a coupler. The couplers direct the light along two different arms of an interferometer. One arm is the reference and the other is the sample arm. The light that exits both arms are shaped by several optical components (mirror, lenses, etc.). These components control specific beam parameters, such as depth of focus and the intensity distribution of the light. The light is back-reflected by the reference arm, into the interference system, propagating along the same path but in the opposite direction. The same happens in the sample arm, but in this case the beam is backscattered by the sample. Different structures within the sample will have different indices of refraction. The returning light is recombined at the coupler and generates an interference pattern. This pattern is recorded by the detector. The translation of the mirror along the propagation direction of the light generates interference patterns from different depths within the sample. The OCT signal recorded during complete travel of the reference mirror is called the depth scan (97).

OCT has been used in intra-operative margin detection of cutaneous, vulvar, breast and gastro-intestinal malignancy. This technique has also been investigated for detection and diagnostic applications in the head and neck (larynx, oral), however, there are not that many studies that show the ability of OCT to intra-operatively

assess resection margins from the head and neck region. Hamdoon *et al*, has used OCT for intra-operative margin evaluation of patients with T1 and T2 (NOM0) oral cavity squamous cell carcinoma (N=28). The margins were evaluated with OCT and, after, confirmed by histopathology. OCT had an overall sensitivity and specificity of 81.5% and 87%, respectively. The positive predictive value was 61.5% and the negative predictive value was 95%. The positive margins could be identified by architectural changes and an increase of the epithelial layer thickness, as mentioned by the authors (98).

The studies demonstrated that with OCT the positive superficial margins (mucosa) could be identified however, the use of OCT-technology is limited. The OCT image can be affected by the lack of normal tissue perfusion. This means that the resolution and contrast of the OCT images are influenced by the "ex-vivo nature" of the approach. Moreover, as HRME, OCT has the disadvantage that it requires complicated subjective image-interpretation (97,98).

### **1.3.7 Raman spectroscopy**

Raman spectroscopy is the optical technique that was investigated for intra-operative evaluation of the OSCC surgical margins in this thesis. Raman spectroscopy is an objective technique based on inelastic scattering of monochromatic light that provides detailed quantitative and qualitative information about the molecular composition of tissue. The technique is non-destructive and there is no need for reagents or labelling, which promotes easy translation to the clinics (76,99-102). This technique can be applied to assess the mucosa, as well as, the deep soft tissue layers (61-66).

In 2015, Cals *et al* have investigated the potential of Raman spectroscopy for oral cancer detection in surgical margins. They have acquired 88 spectra from tumor and 632 spectra from healthy surrounding tissue. Linear discriminant analysis was used to create classification models that could distinguish tumor from adipose tissue, nerve, muscle, gland, connective tissue and squamous epithelium in 100%, 100%, 97%, 94%, 93%, and 75% of the cases, respectively. This study showed how well Raman spectroscopy enables discrimination between tumor and surrounding healthy tissue structures (21).

In 2016, Cals *et al* have reported that with a 2-step PCA-LDA model tongue squamous cell carcinoma could be discriminated from healthy tissue with a sensitivity of 100% and a specificity of 78% (102).

To better understand what is Raman spectroscopy and when was for the first time found the Raman effect, the history and Raman instrumentation is below described.

### *Raman effect*

The Raman effect results from the interaction of the light with molecules through inelastic scattering of light (optical effect). Light can interact with molecules in three different ways: absorption, elastic scattering and inelastic scattering (76). Only a small part of the incident photons undergoes inelastic scattering, about 1 in a million to 1 in a 100 million (99). In the Raman scattering process, the incident light transfers energy to the illuminated molecules, which causes frequency shifts in the light that is scattered.

The energy of the scattered photon can either increase or decrease. If the photon transfers energy to a molecule, the frequency of the light decreases, and the wavelength increases (Stokes inelastic scattering). If the molecule transfers energy to the photon, the frequency of the light increases, and the wavelength of the scattered light will be shorter than the wavelength of the incident light (anti-Stokes inelastic scattering) (100).

The molecule only transfers energy to photon if it is already in an excited vibrational state, which is rare at room temperature. Therefore, Stokes scattering has higher signal than anti-Stokes scattering, and is mostly used for Raman spectroscopy applications (101).

The change between initial and final energy of the molecule is called the Raman shift, and is given by:

$$\Delta\omega = \left(\frac{1}{\lambda_0} - \frac{1}{\lambda_1}\right) \cdot 10^7 \quad (1.2.1.1)$$

where  $\Delta\omega$  is the Raman shift ( $\text{cm}^{-1}$ ),  $\lambda_0$  is the initial photon wavelength (nm), and  $\lambda_1$  is the final photon wavelength after a scattering event (nm). Raman shifts are typically expressed in relative wavenumbers ( $\text{cm}^{-1}$ ).

The energy needed to excite a molecular vibration is quantified and depends on the mass and strength of the chemical bonds between the atoms of that specific molecule. The chemical bonds behave like springs that can stretch and bend (76). There are different vibrational modes, such as: asymmetric and symmetric stretching, rocking (atoms remain in the same plane), wagging, scissoring and twisting, see figure 3.

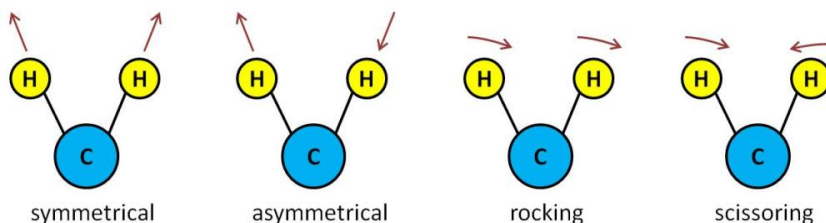


**Figure 3. Some examples of molecular vibration modes.**

Stretching modes change the chemical bond length. Rocking, wagging, and twisting modes change the angle of the chemical bonds. The independent number of vibrational modes, also known as normal modes, can be given by

$$\text{number of normal modes} = \begin{cases} 3N - 6, & \text{for nonlinear molecules} \\ 3N - 5, & \text{for linear molecules} \end{cases}$$

(1.2.1.2)

where  $N$  is the number of atoms in the molecules. Every atom inside a molecule, contributing to a specific normal mode, vibrates with a certain frequency, the frequency of the normal mode (76). This frequency depends on the mass of the atoms. Two molecules only have the same normal modes if they are identical. A Raman spectrum of a molecule shows the intensity of all possible vibrations as a function of the Raman shift. Even though two different molecules can have completely different Raman spectra caused by their composition, if they have some chemical groups in common, the Raman signal will present peaks at identical Raman shifts, but with different intensity. This means that the molecules can be identified by their vibrational properties and that the inelastic scattering of a molecule is highly specific (76).

Therefore, Raman spectroscopy is a quantitative technique: a Raman spectrum of a sample with different (non-interacting) molecules is a linear superposition of the spectra of the all individual molecules in their relative concentrations. A Raman spectrum of a tissue sample is a very complex spectrum, reflecting all different molecules (and their interactions) that are present. Therefore, a tissue spectrum is very specific and can be regarded as an optical fingerprint of the tissue. Slight changes in a tissue, induced by a disease, will lead to changes in the tissue spectrum, and therefore, tissue Raman spectra can be used to discriminate between healthy and diseased tissue (76).

The Raman spectrum is often divided in two major regions: the fingerprint region with wavenumbers ranging from about  $200 \text{ cm}^{-1}$  to  $2000 \text{ cm}^{-1}$ , and the high-

wavenumber region with wavenumbers ranging from about  $2400\text{ cm}^{-1}$  up to  $4000\text{ cm}^{-1}$ . The fingerprint region is very rich in spectroscopic information. The high-wavenumber region contains mainly information on the CH-, OH- and NH-stretching vibrations (76).

For this thesis the focus of study was the high-wavenumber region. The interest for using high-wavenumber Raman spectroscopy in-vivo and/or ex-vivo has increased in the last years. A study by Koljenović *et al.* showed that, for discriminating cancer from healthy tissue, essentially the same diagnostic information is obtained in either of the two spectral regions (fingerprint or high-wavenumber) (103). Raman spectroscopy in the high-wavenumber region demonstrates significant advantages for ex-vivo and in-vivo use when compared to the commonly used fingerprint region. The intensity of the signal in the high-wavenumber region is higher than in the fingerprint region, and measurements can be performed in shorter integrations times. Additionally, fiber-optic materials like fused silica do not have Raman signal at the high-wavenumber region of the Raman spectrum (103). This enables the use of simple and cheap single fiber optic probes that can be easily inserted in endoscopes and/or needles to perform in-vivo measurements in hollow organs or surface assessment of solid organs such as oral cavity (104,105), lung (106,107), upper gastrointestinal tract (108-110) and colorectal (111,112).

### *History of Raman spectroscopy*

The first experimental evidence of the Raman effect was reported in the afternoon of 28 February 1928 by Raman (Sir Chandrasekhara Venkata Raman) and Krishnan (Sir Kariamanickam Srinivasa Krishnan), see figure 4. They examined the scattered track through a direct vision spectroscope, using a narrow range of transmission of the incident radiation. They discovered that there was a wavelength shift between the scattered light and the incident light (101,113).



C. V. Raman



K. S. Krishnan

**Figure 4. Portraits of C. V. Raman and K. S. Krishnan.**

This work was addressed as 'New Radiation' and it was given to South India Science Association at Bangalore on 16 March 1928 (101,113). The effect became known as the 'Raman effect'. The first line of a spectrum, which was first seen on 28 February 1928 was given publicity on the following day through the Associated Press of India. Raman published the results in a letter sent to Nature on 8 March 1928, appearing on 21 April 1928 (114). It is said that the referee had rejected the letter but that the Editor of Nature (Sir Richard Gregory) took the responsibility on publishing this letter. To give maximal publicity to his discovery, Raman, after publication of his historical paper in the Indian Journal of Physics, obtained 2000 reprints of his article and posted them to all the relevant physicists that at the time were working on the scattering of light, and to scientific institutions all over the world (101).

In 1930, Professor Raman was awarded with the Nobel Prize for physics, and with the Hughes Medal of the Royal Society of England.

Raman spectroscopy started to be used for biological samples after the invention of the laser, in 1960 (115). Ten years after that, charge coupled devices (CCD) were developed. This invention was a major development in the use of Raman spectroscopy, because it allowed collection of a full spectrum at once, and tremendously decreased the time needed for collection of a high-quality spectrum (116).

In 1990, Puppels combined Raman spectroscopy with confocal microscopy. For the first time it was possible to perform Raman spectroscopy inside cells and distinguish different cellular structures (117).

Thanks to the microcomputer revolution, multivariate statistical analysis of Raman spectra can be applied in real time for extracting the relevant information that is present in the spectra. This has helped Raman spectroscopy to become a powerful analytical technique that can be used for many diagnostic applications.

More recently, fiber-optic probes have enabled the use of Raman spectroscopy for in-vivo biomedical applications. The integration of Raman spectroscopy with other diagnostic techniques has been reported as a major step towards the development of clinical applications, such as biopsy guidance and early cancer diagnosis. An example of this integration is the insertion of fiber probes into endoscopic channels, which enabled in-vivo measurements in hollow organs or surface assessment of solid organs: oral cavity (118,119), lung (120,121), upper gastrointestinal tract (37,122-126), colorectal (127,128), bladder (129), and cervical cancers (130-134). In the last years, several Raman probes have been designed for specific clinical targets, such as the specific pathophysiology of the disease, and the specific anatomy of the

region of interest, by optimizing e.g. the accessibility of the tissue, sample size, and sampling depth (1,134).

### *Raman Instrumentation*

A Raman system typically consists of four major components. These are an excitation source, illumination/collection optical system, a wavelength separator/filter and a detector.

The excitation source should be monochromatic. Because a laser has a small bandwidth compared to other types of light source, it is a proper choice for a monochromatic light source. The choice of laser wavelength depends on the Raman region of interest.

Illumination of the tissue sample and collection of the Raman scattered light can be achieved by using a lens system (e.g. a microscope) or optical fibers. An optical fiber is a very thin a circular waveguide for light that can be used to make thin Raman probes for accessing vary parts of the body that otherwise cannot be reached. One fiber or multiple fibers can be used for both illuminating and collection. The (fraction of the) scattered light that is collected is directed to the spectrometer, where the collected light is dispersed, mostly using a diffraction or transmission grating.

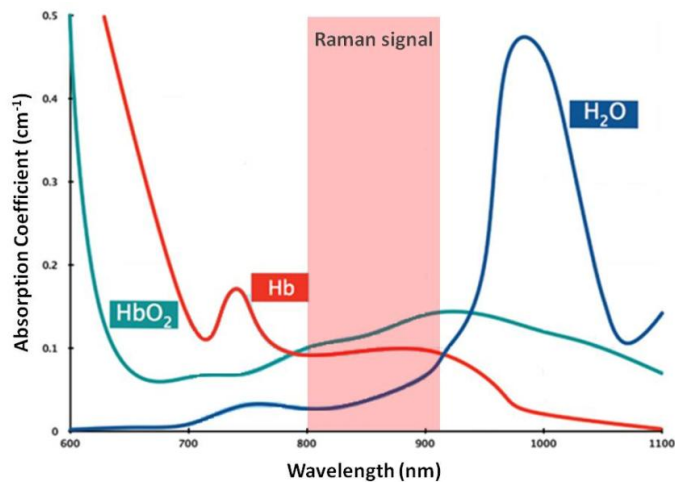


**Figure 5. The absorption spectra of main human tissue light absorbers: water and hemoglobin (Hb and HbO<sub>2</sub>). Raman signal window is marked with pink (800-920 nm). Biological tissues have very low absorption in the Raman signal window presented (with exception of melanin).**

The grating acts as a wavelength separator, because it diffracts photons with different wavelengths under different angles. The dispersed light is then focused on a multichannel detector, which is in most cases a CCD (Charge Coupled Device), but also other types are used such as a photodiode arrays, CMOS detectors, and InGaAs detectors. For this thesis the Raman region of interest is the high-wavenumber region (wavenumbers ranging from about  $2400\text{ cm}^{-1}$  up to  $4000\text{ cm}^{-1}$ ). The laser selected has an excitation wavelength of 671 nm. For the measurements described in this thesis, both, a microscope and optical fibers were used for illumination and collection of light. The separator/filter allowed the collection of Raman signal in the range 800-920 nm. The characteristics of the setup guarantee minimal absorption of the light by water and hemoglobin ( $\text{HbO}_2$  and Hb), as shown in the figure 5. These substances are in abundance in the human body.

## 1.4 This thesis

The goal of this thesis was to investigate how high-wavenumber Raman spectroscopy can be used as an IOG tool for assessment of soft tissue and bone resection margins in head and neck surgical oncology.

In chapter 2, a review on the oncological Raman spectroscopy applications developed in the last 10 years is presented. The published Raman studies aim to: detect pre-malignant lesions, detect cancer in less invasive stages, reduce the number of unnecessary biopsies and guide the surgery towards the complete removal of the tumor with adequate resection margins. Also, in chapter 2, the actual clinical needs in oncology that can be, and are being, addressed by Raman spectroscopy are summarized. Moreover, the status and the main hurdles of translation of these applications into clinical practice are discussed.

In chapter 3, the potential of high-wavenumber Raman spectroscopy to distinguish tumor from the healthy soft tissue of ex-vivo tongue resection specimens from patients that underwent surgical treatment for squamous cell carcinoma of the oral cavity was investigated using a confocal Raman microscope. Based on water concentration, calculated using the high-wavenumber Raman spectra, tumor and healthy tongue tissue could be discriminated with high sensitivity and specificity.

Based on the experience acquired during the experiments performed in chapter 3, it was noted that, even though the high-wavenumber region shows less tissue luminescence than the fingerprint region, the luminescence signal can still be orders of magnitude stronger than the Raman signal. There are not many software solutions to remove luminescence background in the high-wavenumber region. Therefore, in

chapter 4, the luminescence background signals of ex-vivo high-wavenumber region spectra of oral tissue were characterized, and the performance of two algorithms for correction of these background signals were compared. This was a major step towards a selection of the best method for non-supervised and automatic correction of fluorescence background signals.

In chapter 5, the difference in water concentration found between tumor and healthy surrounding tissue (chapter 3) was used to localize the border in soft tissue of oral cavity squamous cell carcinoma specimens. In chapter 5, The usefulness of high-wavenumber Raman spectroscopy as an objective tool for assessment of the resection margins in oral cavity squamous cell carcinoma specimens was demonstrated.

In chapter 6, the potential of high-wavenumber Raman spectroscopy for detection of OCSCC in bone resection surfaces during mandibulectomy was investigated. This chapter is a crucial step towards the use of Raman spectroscopy not only for intra-operative assessment of soft tissue resection margins, but also for bone resection margins.

In chapter 7, the first steps toward the development of IOG Raman tool for assessing the entire tumor resection surface are shown. The IOG Raman tool uses a single-fiber-optic needle probe for discriminating oral cavity squamous cell carcinoma from healthy tissue based on water concentration. The IOG Raman needle probe can be used to inspect the resection surface and the deep tissue layers, which may allow an oncological radical surgery and thereby improvement of patient outcome.

Chapter 8 contains a general discussion and the future perspectives of the application of the IOG Raman tool for assessment of the resection margins in OCSCC.

In chapter 9, a summary of this thesis is presented.

## References

1. Santos I. P., Barroso E. M., Bakker Schut T. C., *The Analyst*. 2017;142(17):3025-3047.
2. Senft C., Bink A., Franz K., *Lancet Oncol*. 2011; 12(11):997–1003.
3. Senft C., Schoenes B., Gasser T., *J. Neurosurg. Anesthesiol*. 2011; 23(3): 241–6.
4. Wong J. M., Panchmatia J. R., Ziewacz J. E., *Neurosurg. Focus*. 2012; 33(5): E16.
5. Wu J.-S., Mao Y., Zhou L.-F., *Neurosurgery*. 2007; 61(5): 935–949.
6. Claus E. B., Horlacher A., Hsu L., *Cancer*. 2005;103(6): 1227–1233.
7. Kuhnt D., Becker A., Ganslandt O., *Neuro. Oncol*. 2011;13(12):1339–1348.
8. Kubben P. L., ter Meulen K. J., M. G. Schijns O. E., *Lancet Oncol*. 2011;12(11): 1062–1070.
9. Visgauss J. D., Eward W. C. and Brigman B. E., *Orthop. Clin.North Am*. 2016; 47:253–264.
10. Prada F., Perin A., Martegani A., *Neurosurgery*. 2014;74(5): 542–552.
11. Selbekk T., Jakola A. S., Solheim O., *Acta Neurochir.(Wien)*. 2013;155(6):973–980.
12. Erickson-Bhatt S. J., Nolan R. M., Shemonski N. D., *Cancer Res*. 2015;75(18): 3706–3712.
13. Stummer W., Pichlmeier U., Meinel T., *Lancet Oncol*. 2006;7(5): 392–401.
14. Widhalm G., Kiesel B., Woehrer A., *PLoS One*. 2013. DOI:10.1371/journal.pone.0076988.
15. Stummer W., Tonn J.-C., Mehdorn H. M., *J. Neurosurg*. 2011;114(3): 613–623.
16. Roberts D. W., Valdes P. A., Harris B. T., *J. Neurosurg*. 2011;114(3):595–603.
17. Cognetti D. M., Weber R. S., and Lai S. Y., *Cancer*. 2008;113(7 0):1911-1932.
18. Chaturvedi A. K., Anderson W. F., Lortet-Tieulent J., *J. Clin. Oncol*. 2013; 31:4550-4559.
19. Ravi S. P., *J. of Clinical and Diagnostic Research*. 2014;8(9):ZE01-ZE05.
20. Miles B. A., Patsias A., Quang T., *The Laryngoscope*. 2015;125:2308-2316.
21. Cals F. L. J., Schut T. C. B., Hardillo J. A., *Laboratory Investigation*. 2015.
22. Ferlay J., Soerjomataram I., Dikshit R., *Int. J.Cancer*. 2015;136(5): E359–E386.
23. Vigneswaran N., Williams M. D., *Oral Maxillofac Surg Clin North Am*. 2014;26(2):123-141.
24. Karim-Kos H. E., de Vries E., Soerjomataram I., *Eur. J. Cancer*. 2008;44:1345–89.

25. Patel S. C., Carpenter W. R., Tyree S., *J Clin Oncol.* 2011;29:1488-1494.
26. Hashibe M., Brennan P., Chuang S. C., *Cancer Epidemiol Biomarkers Prev.* 2009;18:541-550.
27. Neville B. W., Day T. A., *CA Cancer J Clin.* 2002;52:195-215.
28. Datema F. R., Ferrier M. B., van der Schroeff M. P., *Head & Neck.* 2009;32:728-736.
29. van der Ploeg T., Datema F., Baatenburg de Jong R., *PLoS One.* 2014;9(6):e100234.
30. Myers J. N., Greenberg J. S., Mo V., *Cancer.* 2001;92:3030-3036.
31. Greenberg J. S., Fowler R., Gomez J., *Cancer.* 2003;97:1464-1470.
32. Chinn S. B., Spector M. E., Bellile E. L., *Otolaryngol Head Neck Surg.* 2013;149:893-3036.
33. Helliwell T. R., Woolgar J. A., *London: Royal College of Pathologists Publications,* 2000.
34. Helliwell T., Woolgar J., *The Royal College of Pathologists.* 2013.
35. Dillon J. K., Brown C. B., McDonald T. M., *J Oral Maxillofac Surg.* 2015;73:1182-8.
36. Slootweg P. J., Hordijk G. J., Schade Y., *Oral Oncol.* 2002;38:500-503.
37. Al-Rajhi N., Khafaga Y., El-Husseiny J., *Oral Oncol.* 2000;36:508-514.
38. Binahmed A., Nason R. W., Abdoh A. A., *Oral Oncol.* 2007;43:780-4.
39. Loree T. R., Strong E. W., *Am J Surg.* 1990;160:410-4.
40. Smits R. W. H., Koljenović S., Hardillo J. A., *Head & Neck.* 2015; doi: 10.1002/hed.24075.
41. Varvares M. A., Poti S., Kenyon B., *Laryngoscope.* 2015; doi: 10.1002/lary.25397.
42. Hinni M. L., Ferlito A., Brandwein-Gensler M. S., *Head Neck.* 2013;35:1362-70.
43. Yahalom R., Dobriyan A., Vered M., *J Surg Oncol.* 2008;98:572-8.
44. Chang A. M., Kim S. W., Duvvuri U., *Oral Oncol.* 2013;49:1077-82.
45. Amin M. B., Edge S., Greene S., eds. *AJCC Cancer Staging Manual.* 8th edition. New York, USA: Springer; 2017.
46. Gokavapura S., Rao L. M. C., Mahajan M., *British Journal of Oral and Maxillofacial Surgery.* 2015;(53):875-879.
47. Brown J. S., Kalavrezos N., D'Souza J., *British Journal of Oral and Maxillofacial Surgery.* 2002;40:275-284.
48. Williams D. W., *Curr Oncol Rep.* 2016;18:54.
49. McIntosh E. R., Harada S., Drwiega J., *Annals of Diagnostic Pathology.* 2015;19:326-329.
50. Nijssen A., Koljenović S., Schut T. C. B., *J Biophoton.* 2009;2:29-36.
51. Barman I., Dingari N. C., Saha A., *Cancer Res.* 2013;73:3206:3215.

52. Nieberler M, Häußler P, Kesting MR, *Ann Surg Oncol*. 2016.
53. Francisco A. L. N. Correr W. R., Pinto C. A. L., *Oral Oncology*. 2014;50:593-599.
54. Stephen M. M., Jayanthi J. L., Unni N. G., *BMC Cancer*. 2013;13:278.
55. Sharwani A., Jerjes W., Salih V., *Oral Oncology*. 2006;42:343-349.
56. Vila P. M., Park C. H., Pierce M. C., *Ann Surg. Oncol*. 2013;19(11):3534-3539.
57. Lee A. M. D., Cahill L., Lane P., *Biomedical Optics Express*. 2015;6(7):2664-2674.
58. Singh S. P., Deshmukh A., Chaturvedi P., *J Biomed Opt*. 2012;10:105002.
59. Keereweer S., Kerrebijn J. D. F., Mol I. M., *Head & Neck*. 2012;34:1002:1008.
60. Keereweer S., Mieog J. S. D., Mol I. M., Van Driel P. B. A. A., *Archives of Otolaryngology - Head and Neck Surgery*. 2011;137:609-615.
61. Malini R., Venkatakrishna K., Kutien J., *Biopolymers*. 2006;81:179-193.
62. Oliveira A. P., Bitar R. A., Silveira L., *Photomed Laser Surg*. 2006;24:348-353.
63. Su L., Sun Y. F., Chen Y., *Laser Phys*. 2012;22:311-316.
64. Bergholt M. S., Lin K., Zheng W., *J Biomed Opt*. 2012;17:077002.
65. Liu H., Zhao J., McLean D., *Cancer Res*. 2012;72:2491-2500.
66. Klatt J., Gerich C. E., Grobe A., *J Craniomaxillofac Surg*. 2014; 42:852-854.
67. Poh C. F., Anderson D. W., Durham J. S., *JAMA Otolaryngol Head Neck Surg*. 2016; 142:209-216.
68. Scheer M., Fuss J., Derman M. A., et al. *Oral Maxillofac Surg*. 2016; 20:27-33.
69. Nagi R., Reddy-Kantharaj Y. B., Rakesh N., *Med Oral Patol Oral Cir Bucal*. 2016; PMID: 26946209
70. Lue N., Kang J. W., Yu C. C., *PloS one*. 2012; 7:e30887.
71. Atallah I., Milet C., Coll J. L., *Eur Arch Otorhinolaryngol*. 2015; 272:2593-2600.
72. Tanaka N., Lajud S. A., Ramsey A., *Head Neck*. 2016; 38 Suppl 1:E1351-1357.
73. Zheng J., Muhanna N., De Souza R., *Biomaterials*. 2015; 67:160-168.
74. Rosenthal E. L., Warram J. M., de Boer E., *Clin Cancer Res*. 2015; 21:3658-3666.
75. Croce A. C., Bottiroli G. *European Journal of Histochemistry*. 2014; 58:2461.
76. Hecht. *Optics*. 4th ed. 2002.
77. Keereweer S. Mol I.M., Vahrmeijer A. L., *International Journal of Cancer*. 2012; 131:1633-1640.
78. Kulbersh B. D., Duncan R. D., Magnuson J. S., *Arch Otolaryngol Head Neck Surg*. 2007;133:511-515.

79. Cohen E. E., Davis D.W., Karrison T. G., *Lancet Oncol.* 2009;10:247–257.
80. Shan L., Hao Y., Wang S., *Mol Imaging.* 2008;7:42–49.
81. Orita Y., Kawabata K., Mitani H., *Acta Medica Okayama.* 2008; 62(3).
82. Tirelli G., Piovesana M., Gatto A., *Oral Onc.* 2015; 51:908-13.
83. Vicini C., Montevecchi F., D'Agostino G., *Acta Otorhinolaryngol Ital.* 2015; 35:157-161.
84. Garofolo S., Piazza C., Del Bon F., *Ann Otol Rhinol Laryngol.* 2015; 124:294-298.
85. Nwaneshiudu A., Kuschal C., Sakamoto F., *J Invest Dermatol.* 2012;132:e3.
86. Rajadhyaksha M., González S., Zavislan J., *J Invest Dermatol.* 1999;113:293–303.
87. Nehal K., Gareau D., Rajadhyaksha M., *Semin Cutan Med Surg.* 2008;27:37–43.
88. Maher N. G., Collgros H., Uribe P., *Oral Onc.* 2016; 54:28-35.
89. Muldoon T.J., Pierce M.C., Nida D.L., *Opt Express.* 2007; 15:16413-23.
90. Muldoon T. J., Anandasabapathy S., Maru D., *Gastrointest Endosc.* 2008; 68:737-44.
91. Levy L. L., Vila P. M., Park R. W., *ISRN Minim Invasive Surg.* 2012; PMID: 23641314
92. Chan V., Perlas A., *Springer*, 2011.
93. Yuen A. P., Ng R. W., Lam P. K., Ho A., *Head Neck.* 2008; 30:230-234.
94. Kodama M., Khanal A., Habu M., *J Oral Maxillofac Surg.* 2010; 68:1746-1752.
95. Tominaga K., Yamamoto K., Khanal A., *Dentomaxillofac Radiol.* 2007; 36:409-411.
96. Baek C. H., Son Y.I., Jeong H. S., *Otolaryngol Head Neck Surg.* 2008; 139:805-810.
97. Popescu D. P., Choo-Smith L.-P., Flueraru C., *Biophys Rev.* 2011;3(3):155.
98. Keereweer S., Sterenborg H. J., Kerrebijn J. D., *Head Neck.* 2012; 34:120-126.
99. Koningstein. *Introduction to the theory of the Raman effect.* 1st ed. 1972.
100. Srinivasan. *Vibrational spectroscopic imaging for biomedical applications.* 1st ed. 2010.
101. Krishna R. S., Shankar R. K., *Journal of Raman Spectroscopy.* 1981;10:1-7.
102. Cals F. L. J., Koljenović S., Hardillo J. A., *Oral Oncology.* 2016; 60:41-47.
103. S. Koljenović, T. C. Bakker Schut, R. Wolthuis, *Journal of Biomedical Optics.* 2005;10(3): :031116.
104. H. Krishna, S. K. Majumder, P. Chaturvedi, *J Biophotonics.* 2014;7(9):690–702.
105. Guze K., Pawluk H. C., Short M., *Head Neck.* 2015;37(4):511–7.

106. Short M. A., Lam S., McWilliams A., *Opt Lett.* 2008;33(7):711–3.
107. McGregor H. C., Short M. A., McWilliams A., *J Biophotonics.* 2017;10(1):98-110.
108. Teh S. K., Zheng W., Ho K. Y., *Br J Cancer.* 2008;98(2):457–65.
109. Bergholt M. S., Zheng W., Lin K., *Analyst.* 2010;135(12):3162–8.
110. Duraipandian S., Bergholt M. S., Zheng W., *J Biomed Opt.* 2012;17(10).
111. Bergholt M. S., Lin K., Wang J., *J Biophotonics.* 2016;9(4):333–42.
112. Barroso E. M., Smits R. W. H., Bakker Schut T. C., *Anal Chem.* 2015;87(4):2419–26.
113. Raman C. V., *Indian J. Phys.* 1928;2,387.
114. Raman C. V., *Nature London.* 1928; 212,619.
115. Maiman, *Nature.* 1960;187(8):493-494.
116. Boyle, *Bell systems technical journal.* 1970;49(4):587-593.
117. Puppels G. J., de Mul F. F., Otto C., *Nature.* 1990;347(6290):301-303.
118. Barroso E. M., Smits R. W. H., Van Lanschot C. G. F., *Cancer Res.* 2016;76:5945–5953.
119. Wong E. T. and Wu J. K., [https://www.uptodate.com/contents/clinical-presentation-and-diagnosis-of-brain-tumors?source=search\\_result&search=bra](https://www.uptodate.com/contents/clinical-presentation-and-diagnosis-of-brain-tumors?source=search_result&search=bra) in cancer&selectedTitle=1~150#H22, (accessed 12 May 2017).
120. McGregor H. C., Short M. A., McWilliams A., *J. Biophotonics.* 2016;13:n/a-n/a.
121. Rees J., Lao-Sirieix P., Wong A. and Fitzgerald R., *Cochrane Database Syst. Rev.* 2011;2010–2012.
122. Duraipandian S., Bergholt M. S., Zheng W., *J. Biomed. Opt.* 2012, 17, 81418.
123. Bergholt M. S., Zheng W., Ho K. Y., *Proc. SPIE.* 2014;8939:89390M.
124. Lin K., Wang J., Bergholt M. S., *Proc. of SPIE*, eds. M. J. Suter, S. Lam, M. Brenner, G. J. Tearney and T. D. Wang, Nature Publishing Group. 2015;9304:93040V.
125. Ishigaki M., Maeda Y., Taketani A., *Analyst.* 2015;141:1027–33.
126. Wang J., Lin K., Zheng W., *Sci. Rep.* 2015; 5:12957.
127. Bergholt M. S., Lin K., Wang J., *J. Biophotonics.* 2016;9:333–342.
128. Nanda K., Mccrory D. C., Myers E. R., *Ann Intern Med.* 2000;132:810–819.
129. Ruijter E., Van De Kaa C., Miller G., *Endocr. Rev.* 1999;20:22–45.
130. Duraipandian S., Zheng W., Ng J., *Analyst.* 2011;136:4328.
131. Duraipandian S., Zheng W., Ng J., *Anal. Chem.* 2012;84:5913–5919.

132. Ramos I. R. M., Malkin A. and Lyng F. M., *Biomed Res. Int.* 2015;20151–9.
133. Rubina S., Amita M., Kedar K. D., *Vib. Spectrosc.* 2013;68:115–121.
134. Desroches J., Jermyn M., Mok K., *Biomed. Opt. Express.* 2015;6:2380–97.



## ***CHAPTER 2***

# ***Raman spectroscopy for cancer diagnostics and cancer surgery guidance: translation to the clinics***

Inês P. Santos<sup>†</sup>, Elisa M. Barroso<sup>†</sup>, Tom C. Bakker Schut, Peter J. Caspers, Cornelia G. F. van Lanschot, Da-Hye Choi, Martine F. van der Kamp, Roeland W. H. Smits, Remco van Doorn, Rob M. Verdijk, Vincent Noordhoek Hegt, Jan H. von der Thüsen, Carolien H. M. van Deurzen, Linetta B. Koppert, Geert J. L. H. van Leenders, Patricia C. Ewing-Graham, Helena C. van Doorn, Clemens M. F. Dirven, Martijn B. Busstra, Jose Hardillo, Aniel Sewnaik, Ivo ten Hove, Hetty Mast, Cees Meeuwis, Tamar Nijsten, Eppo B. Wolvius, Robert J. Baatenburg de Jong, Gerwin J. Puppels<sup>†</sup>, and Senada Koljenović<sup>†</sup>

<sup>†</sup> These authors contributed equally to this work.

**The Analyst 2017;142(17):3025-3047**



## Abstract

Oncological applications of Raman spectroscopy have been contemplated, pursued, and developed at academic level for at least 25 years. Published studies aim to detect pre-malignant lesions, detect cancer in less invasive stages, reduce the number of unnecessary biopsies and guide surgery towards the complete removal of the tumor with adequate tumor resection margins. This review summarizes actual clinical needs in oncology that can be addressed by spontaneous Raman spectroscopy and it provides an overview over the results that have been published between 2007 and 2017. An analysis is made of the current status of translation of these results into clinical practice. Despite many promising results, most of the applications addressed in scientific studies are still far from clinical adoption and commercialization. The main hurdles are identified, which need to be overcome to ensure that in the near future we will see the first Raman spectroscopy-based solutions being used in routine oncologic diagnostic and surgical procedures.

## General introduction

In 2012 the World Health Organization (WHO) reported 14.1 million new cancer cases, 8.2 million cancer deaths and 32.6 million people living with cancer (within 5 years of diagnosis). These numbers are increasing, which motivates development of cancer treatment possibilities and technology for early detection of (pre-) malignancies (1). The high mortality rate of cancer can be reduced by early and accurate diagnosis, and by adequate surgical treatment (2). The reference standard for cancer diagnosis is histopathologic assessment of biopsies or diagnostic excisions of suspicious tissue. After biopsy/excision the tissue specimen is fixed, micro-sectioned and routinely stained with haematoxylin and eosin (H&E). The pathologist makes a diagnosis based on microscopic examination of the H&E stained section. Because only small portions of the lesional tissue are biopsied or excised for histopathological examination, there is the risk of sampling error and the pathology report remains a subjective assessment (with its inter and intra operator variability) (3). Studies have demonstrated that most tumor types develop through pre-malignant stages (4,5). Therefore, the treatment of premalignant tissue can prevent the further development of cancer. Because the distinction between early-stage malignant, premalignant and benign tumors can be difficult to make, repeated biopsies/excisions are often taken. For sampling of tissue, literature reports positive predictive values as low as 22% for prostate cancer diagnosis (6), 14% for breast cancer (7), 18.5% in lung cancer screenings (8) and 7-23% for melanoma diagnosis

(9). Despite the risk of these unnecessary biopsies/excisions, a substantial number of early stage tumors are still missed, which increases the risk of progression to a metastatic stage.

### **Introduction – early diagnosis/guided biopsy**

A technique that helps to achieve representative biopsies and that would enable accurate and early in-vivo diagnosis is needed. This tool should detect lesions in pre-malignant/early stages and assess large tissue areas in real-time to decrease sampling errors. Several techniques have been tested for biopsy guidance, such as optical coherence tomography (OCT), white light reflectance (WLR), auto-fluorescence and Raman spectroscopy (10–14). OCT and WLR rely on the visualization of changes in tissue structure. These techniques provide little or no information about the molecular tissue composition and, therefore, generally have a low specificity (10,12). Auto-fluorescence imaging is an optical technique that detects natural fluorescence emitted by fluorophores present in the tissues (e.g. flavins, collagen or hemoglobin), after excitation by a short-wavelength light source. This emission can be captured in real-time, for example during endoscopy, and can be used for lesion detection or characterization (13,14). Auto-fluorescence imaging has shown to improve the sensitivity of detection of early cancer, like epithelial neoplasia in esophagus and colon (sensitivities are 90% and 99%, respectively) (14). It also improves the diagnostic sensitivity (from 67% to 89%) for pre-malignant stages of lung cancer (e.g., dysplasia and carcinoma in situ). It also improves the diagnostic sensitivity compared to white-light endoscopic imaging (from 67% to 89%) for pre-malignant stages of lung cancer. However, the specificity of this technique is low; a specificity of 64% for diagnosing pre-malignant stages of lung cancer, a specificity of 81% for detecting high-grade dysplasia and early cancer in Barrett's esophagus and a specificity of 35% for detection of pre-malignant colon polyps were reported (14-16). Optical vibrational spectroscopic techniques, such as Raman spectroscopy (RS), can provide high molecular specificity. The gradual changes from healthy tissue to tumor are reflected by their Raman spectra (2,17–19). Raman spectroscopy is a technique for characterizing biological tissue in-vivo, ex-vivo or in-vitro and for non-invasive detection of the molecular differences between tumor and healthy tissue. It does not require any labelling, reagents or other preparation of the tissue, which facilitates translation to the clinic. With the use of optical fibers many anatomical locations can be assessed in-vivo (20). Raman spectroscopy-based biopsy guidance can reduce the number of false positive biopsies and increase the accuracy of cancer diagnosis, with reported overall sensitivities and specificities between 73% - 100% and 66% - 100%, respectively (18,21).

## Introduction – guided surgery

After diagnosis the primary treatment for solid tumors is often surgery. The objective of surgical treatment is resection of all malignant tissue with adequate resection margins while preserving important healthy structures. Achieving adequate surgical margins is important for disease control and survival. Residual tumor after surgery is associated with poor survival and the need for additional surgery, adjuvant chemotherapy, radiation therapy, or a combination of these (22–25). A number of studies have shown that the 5-year survival decreases significantly when tumor is not completely removed (22–25). Intra-operative guidance tools can help to achieve adequate surgery. However, there are no widely used intra-operative guidance tools available yet. Current surgical resection techniques are based on subjective methods, such as palpation and visual inspection, to judge the border between normal and cancerous tissue. In order to support the intra-operative assessment of resection margins, frozen sections can be used (26–28). A small piece of suspicious tissue is usually sampled from the wound bed (i.e. wound-driven assessment) by the surgeon. A microscopic evaluation of the frozen section is performed by the pathologist, directing operative management (28). It has been reported that the frozen section procedure increases the rate of adequate resections and thereby decreases local recurrence and improves the survival rate (29). Even though this procedure is successful for intra-operative assessment of the resection margins, it has its limitations: 1) it is time consuming, extending the duration of surgery and anesthesia (30); 2) it is likely prone to sampling errors because only a small fraction of the resection margin can be investigated, and 3) it can introduce histologic disruption caused by rapid freezing, which makes the analysis more difficult (31). Rosenthal *et al.*, reported that at most 5% to 10% of the wound bed can be sampled and assessed with frozen section (32). These limitations can lead to false negative results (23,27,33–35). Consequently, there is much room for improvement in performing intra-operative assessment of the resection margins. In order to guide oncological surgery, techniques like intra-operative real-time MRI, intra-operative ultrasound, intra-operative OCT, fluorescence and Raman spectroscopy have been investigated in operating room environments.

Real-time intra-operative MRI has been tested during surgical resection of brain cancer (i.e. glioma). Several studies have demonstrated that this modality can be used for surgery guidance and improves the extent of the tumor resection without increasing neurological deficits. This also has a positive impact on survival (36–42). Some drawbacks of intra-operative MRI include: 1) operative defects that can affect the MRI image and decrease its accuracy (43); 2) interpretation of the image by the surgeon and his capability to correlate the location of the lesion to the brain anatomy (17,43); 3) significant surgical disruptions that prolong the operation time; 4) it

requires a considerable investment to implement MRI-capable operating rooms; and 5) there is a need for contrast agents (43).

Intra-operative ultrasound has been used to localize the tumor, guide the resection especially among highly vascular tumors (breast, e.g.), using probes that enhance contrast (43,44). However, it is less sensitive for tumor margins and has shown lower resolution and accuracy compared to intra-operative MRI. Besides, its accuracy is affected by previous surgery, as almost any imaging modality (43,45). A portable label-free optical coherent tomography (OCT) imaging system has been tested intra-operatively to assess breast resection margins and lymph nodes ex-vivo (46). The study showed promising results for real-time microscopic image-guide breast cancer surgery. Structural-based imaging techniques (like OCT and intra-operative MRI) show promising results. Unfortunately, they lack chemical disease-specific information, which is essential for adequate tumor removal.

Fluorescence imaging is another technique that has been applied to assess surgical resection margins. The technique requires administration of fluorescence agents and is based on the detection of fluorescently labelled structures during surgery. Various studies have reported that complete resection was achieved in a significantly higher percentage when fluorescence imaging was used, as compared to only regular white light (47–50). The major disadvantages of fluorescence imaging are: 1) the need for fluorescence agents, and 2) the need to switch off the room lighting to maximize the detection of the weak fluorescence (46). In addition, translational problems have been identified, related to the need of consistent manufacturing, to costs related with toxicology studies, and to the strict procedures for submission of a new investigational drug (51). An interesting alternative would be a label-free imaging method, which avoids the risks associated with dye/drug reactions and the challenges associated with specific tumor targeting and non-specific binding.

Raman spectroscopy has also been implemented to guide oncological surgery. Several studies have demonstrated that this technique can be used for surgical guidance. For example, in brain cancer surgery, an intra-operative Raman system that measures directly brain tissue in the patient, has proven to distinguish dense and low-density cancer infiltration from benign brain tissue with a sensitivity of 93% and a specificity of 91% (52). In another study, a real-time Raman intra-operative system was used during breast cancer surgery for assessment of freshly resected specimens. This study has demonstrated that Raman spectroscopy could discriminate cancerous tissue from normal breast tissue with a sensitivity of 83% and a specificity of 93% (53). Implementing Raman spectroscopy in the clinical setting can have important benefits: 1) it can enable representative sampling for correct pathological diagnosis (biopsy guidance); 2) it can accurately assist in defining adequate resection margins

during surgery; 3) it can reduce the sampling problem, during intra-operative assessment; 4) it can introduce a more objective assessment and 5) it can reduce the need for adjuvant therapies (20). In the last years, several review articles reported the advances of Raman spectroscopy with the ultimate goal the clinical application for cancer diagnosis in different anatomical locations (17,18,20,21,54–57). In these reviews the latest developments of technology adaptations for Raman cancer diagnostic applications are described. The latest clinical outcomes of Raman spectroscopy on (early) cancer detection at different sites in-vitro, ex-vivo and in-vivo have been also reported. However, specifically the translation of Raman spectroscopic developments into oncological applications has not been addressed extensively before.

The scope of this article is to provide an analysis of the translation of R&D results, obtained in oncological applications of Raman spectroscopy, into clinical practice. We discuss problems that still need to be solved in order to bring the technique successfully to the end-users in the hospital setting. The importance of defining the clinical needs and requirements, for different applications, is also explored in this review. We have limited our review to spontaneous Raman spectroscopy applications on ex-vivo and/or in-vivo human tissue samples. We refer to the other recent review articles for biomedical applications of non-linear Raman spectroscopy, such as coherent and surface-enhanced Raman scattering (55,58,59).

## Methods

### Literature search

A search was carried out using the Web of Science™ library. Web of Science™ comprises the following databases: Web of Science™ Core Collection, KCI-Korean Journal Database, MEDLINE, Russian Science Citation Index and SciELO Citation INdex. For research articles the included period was from 2006 to 2017. For review articles the included period was from 2011 to 2017. The date of the final search was on 16th of January 2017. The search filter comprehended a combination of the keyword “Raman” with two of the following keywords: "tumo(u)r", "patient", "biopsy", "carcinoma", "assessment", "intra-operative", "cancer", "guidance", "surgery", "human", "diagnostics" and "translation". These keywords were searched as a topic in the article. Articles that had at least three of the topic words were considered for inclusion. Commentaries and opinion articles were excluded. Furthermore, studies on non-human samples and performed in-vitro were not selected. Studies that used non-linear Raman spectroscopy were excluded.

Cytological screening methods based on Raman Spectroscopy are also being developed (60,61), however to limit the scope we have chosen not to include such studies in this review. Articles that were not written in English were also discarded.

### **Definition of the clinical need**

The clinical needs (clinical problems and their relevance) that could be solved by Raman spectroscopy applications were defined per cancer type as reported by the studies selected in this review. Furthermore, the information on clinical needs from current (inter)national guidelines and clinical articles (PubMed) were included. For clinical articles the included period from 1990 to 2017 was regarded. Moreover, opinion from pathologists and surgeons was obtained based on personal interviews. During the interviews clinical needs for other types of cancer than those addressed in the included studies were identified and discussed.

### **Raman spectroscopy applications**

All the eligible Raman application studies were included, regardless the cancer type addressed. The included studies were divided considering two major oncological applications of Raman spectroscopy: (A) biopsy guidance/early diagnosis and (B) surgery guidance.

### **Progress of the companies**

To address the progress of the companies that are developing/ have developed commercial Raman spectroscopy oncological applications towards implementation in the clinics, we have contacted leading companies in Raman spectroscopy to collect information. The contacted companies were: Tokyo Instruments Inc., Princeton Instruments Inc., Verisante Inc., ODS Medical Inc., Endofotonics Pte. Ltd., RiverD International B.V., EmVision LLC, Invenio Imaging Inc., Artphotonics GmbH, Carl Zeiss GmbH, Kaiser Optical systems Inc., Lambda solutions Inc., Horiba Jobin-Yvon Inc., B&W Tek Inc., Snowy Range instruments Inc., Wasatch Photonics Inc., Witec GmbH, Avantes B.V., Photonetc Inc. and Renishaw Plc.. A questionnaire was sent to the companies with the following questions: 1) “Are you actively developing or collaborating in the development of oncological Raman in-vivo and/or ex-vivo tools for the clinics?”; 2) “Can you indicate what is the application?”; 3) “Do you have any scientific publication, or can you share with us more information about the subject?”; 4) “When do you think that it will be available in the market? What is the prognosis?”, and 5) “About the translation to the clinics, what hurdles have you encountered?”.

## Technology readiness level (TRL) classification of the studies

In order to provide an overview of the current status of the technology towards clinical translation we classified all the included studies based on the Technology Readiness Level (TRL). The TRL is an index used to measure the maturity and usability of an evolving technology (62). There are 10 levels (TRL 0 to TRL 9): at TRL 0 there is just an idea, but the concept is not yet proven or not yet tested; TRL 1 is related to basic research, when the principles are observed and postulated, but not experimentally proven; TRL 2 is associated with technology development, when the concept and application have been formulated; TRL 3 consists of applied research/proof of concept, when the first laboratory tests are completed; at TRL 4 a small scale prototype has been realized, which is still working in a laboratory environment; at TRL 5 the prototype has been tested in intended environment; at TRL 6 the prototype system has been tested in the intended environment close to the expected performance; at TRL 7 use of the system has been demonstrated in an operational environment at a precommercial scale; TRL 8 is characterized by the first version of a commercial system, when manufacturing issues are solved; finally, at TRL 9, the technology is available for end users. We have grouped the TRL levels of the Raman applications into 4 main categories: (A) the proof of concept has been tested in the laboratory (TLR 0-3), (B) first hardware and software have been developed, including the algorithms for detection of (pre-) malignant lesions, and experiments have been performed close to the intended environment (TLR 4), (C) the developed hardware and software were tested with an independent dataset in the intended environment and preferably at different centers (TLR 5-7), and (D) the first of a kind commercial system(s) are/will be available soon for end users (TLR 8-9).

## Results

### Clinical need and Raman applications

*Definition of the clinical need.* Prior to the development of technological tools aiming to improve diagnosis and/or treatment of cancer, it is important to define the actual clinical needs, because various clinical problems have different needs and solutions. Currently, two main oncological clinical needs, which could be fulfilled by Raman spectroscopy, have been identified: (A) diagnostic tools for biopsy guidance for early diagnosis of (pre-) malignant, and (B) tools for surgery guidance, which can be used for intra-operative assessment of resection margins to achieve

adequate tumor resection. In this section we review several clinical problems in the process of diagnosis and surgical treatment of cancer.

*Literature search for Raman spectroscopy applications.* Raman spectroscopy has been explored for oncological applications in numerous studies, employing various types of measurement systems, and targeting various types of cancers. This section also provides a review of the use of Raman spectroscopy ex-vivo and in-vivo for early diagnosis, biopsy guidance and surgery guidance of different types of cancer. Based on the search terms, 42 research papers on oncological applications of Raman spectroscopy were included. From those, 36 studies regarded early diagnosis and biopsy guidance applications and 6 studies regarded surgery guidance applications.

## **Breast Cancer**

*Clinical need:* The second leading cause of cancer-related deaths in women worldwide is breast cancer with a worldwide incidence rate of more than 1,670,000 and a mortality rate of 522,000 (1). Presently, screening mammography is used to identify breast lesions. When suspicious lesions are found histopathological diagnosis is the next step, based on fine-needle aspiration cytology and/or histological biopsy (63). High sensitivity for fine-needle aspiration cytology (82-99.7%) and for biopsy (90.1-93%) is reported (64-68). The treatment of choice for ductal carcinoma in situ and early stage invasive cancer is breast conserving surgery. The surgery aims to preserve as much healthy tissue as possible while achieving negative resection margins (69). This procedure is performed in 58-70% of the patients (70,71). As a standard of treatment, patients receive adjuvant radiotherapy after surgery. In the Netherlands, resection margins are considered adequate when 'no tumor touches ink' (72). Concerning pure DCIS resection margins of 2 mm are considered adequate. It is proven that patients with more than focal tumor positive resection margins have higher risk of developing recurrent disease (73,74). When final histopathology shows a more than focal positive margin (concerning pure ductal carcinoma in situ) an additional resection is performed. Reresection rates varying between 7%-73% have been reported by different institutes (73). Therefore, an intra-operative guidance with an objective and rapid tool is needed to achieve high adequate resection rates.

*Raman applications for early diagnosis/biopsy guidance:* Saha *et al.*, developed a Raman spectroscopic tool for detecting microcalcifications, as an adverse sign, in breast tissue. An ex-vivo study was conducted, and Raman spectra were acquired in fresh stereotactic breast needle biopsies from 33 patients using a portable compact clinical multi-fiber Raman spectroscopy probe system. This first

study resulted in a positive predictive value of 97% for detecting microcalcifications, demonstrating potential of Raman spectroscopy as real-time feedback tool for radiologists and to reduce unnecessary biopsies (75).

*Raman applications for surgery guidance:* Barman *et al*, looked at the utility of Raman spectroscopy as a guidance tool for mastectomy procedures. Spectra were acquired ex-vivo on freshly excised specimen from a total of 33 patients. The Raman instrument was a portable clinical fiber probe system. A classification algorithm was developed to differentiate breast cancer from healthy tissue. The reported sensitivity was 62.5% with a specificity of 100%. The accuracy obtained for differentiation between normal, fibrocystic change, fibroadenoma, and breast cancer was 82.2% (76).

## Skin Cancer

*Clinical Need:* The clinical diagnosis of skin cancer is conventionally based on visual inspection of morphologic characteristics of the lesions, usually supported by a dermoscope. This manner of diagnosing cancer is subjective and largely depends on the experience of the clinician.

Keratinocytic cancers: Keratinocytic cancers, such as the basal cell carcinoma (BCC) and squamous cell carcinoma (SCC), are two of the most common cancers in fair-skinned populations (77). Only in the United States of America, about 3 million people are diagnosed with keratinocytic cancers per year. Although keratinocytic cancers are associated with low mortality rates both, BCC and SCC, can destruct surrounding tissue, recur and/or metastasize (78). SCC can be locally aggressive, difficult to treat and it is associated with a 0.5% - 5% risk of metastasis. An effective management can be challenging in cases of patients with multiple lesions, or patients that in the past were diagnosed with keratinocytic cancers, demonstrating the need for early diagnosis (79). Standard type of treatment for keratinocytic cancers is complete removal of the lesion by 1) standard surgical excision or 2) Mohs micrographic surgery (MMS). In standard surgical excision, resection margins are examined by the pathologist after the procedure. In low risk BCC a tumor free resection margin of 3 mm is recommended, and in high risk BCC a margin of 5 mm is advised (78,80). In MMS, complete resection margins are examined by the specifically trained dermatologist and/or pathologist during the procedure, aiming to spare healthy tissue while removing completely the cancer cells. MMS leads to fewer recurrences; however, this procedure is labour-intensive and time consuming (81). Therefore, a tool that could quickly detect the cancer cells at the resection margins, could guide the excision towards an adequate surgical margin and accelerate the surgical procedure (21,82).

Melanoma: Melanoma is the most commonly fatal form of skin cancer with a worldwide incidence of 232,130 and mortality rate as high as 55,488 (1). Melanoma is preferably diagnosed at an early stage because of its metastatic disease. The vertical depth of growth in a primary melanoma, the Breslow thickness, is significantly correlated with metastatic propensity and thus prognosis. Melanoma with < 1mm thickness can be treated surgically with a high cure rate without reducing life expectancy (5year survival is approximately 97%) (83,84). Once the melanoma is diagnosed at an invasive stage, the survival rate decreases enormously to approximately 40% for melanomas with a Breslow thickness >4 mm (83,85). Patients with thick melanomas and signs of distant metastasis are submitted to surgery and/or immunotherapy, which places a high burden on the patient's quality of life. Moreover, the effect of current treatments on patient survival is very limited. Even with the use of a dermoscope by an experienced clinician, the sensitivity in diagnosing melanoma is between only 68% and 96% and it is very much depending on the clinician's experience (9,86,87). Despite the large number of excised benign pigmented lesions (false positive suspicious lesions), 30% of early stage melanomas is still missed at the first clinical presentation and thereby present a risk to progress to a metastatic stage (88). Because of the severe consequences when a melanoma is missed, many suspicious pigmented skin lesions are surgically removed. The clinical positive predictive values are as low as 7% to 23% for melanoma diagnosis by dermatologists in a specialized pigmented lesion clinic (9,89). Therefore, a rapid, objective, real-time tool for clinical diagnosis could reduce the number of unnecessary excisions, guarantee early detection of melanoma, and, at the same time, could be used for lesions surveillance.

*Raman applications for early diagnosis/biopsy guidance:* Investigations of Raman spectroscopy for skin cancer focus primarily on (early) detection of skin cancer and discrimination of benign from malignant and pre-malignant skin tumors (2,18,79,90-95). In 2008, Raman experiments were performed in-vivo by Zhao *et al*, on 289 patients using a single fiber Raman probe; Raman spectra were measured from 9 different types of lesions, including BCC and SCC. The authors report a sensitivity of 91% and a specificity of 75% in differentiating malignant lesions from benign lesions. Malignant melanoma could be distinguished from pigmented benign lesions with reported sensitivity of 97% and specificity of 78% (96). In the same year, Lieber *et al*, used a portable Raman system with handheld probe for non-melanoma skin cancer diagnosis (97). Lieber *et al*, performed an in-vivo study on 19 patients. Using the same handheld probe, Lieber *et al*, report classification of the BCC, SCC, inflamed scar tissues and normal tissues with sensitivity of 100% and specificity of 91%. The reported overall classification accuracy was 95% (98). In 2012, Lui *et al*, measured 518 in-vivo skin lesions from 453 patients. Malignant and

pre-malignant lesions could be separated from benign skin lesions using a single fiber Raman probe with a reported sensitivity of 90% and a specificity of 64%. Benign pigmented lesions could be distinguished from melanoma with reported sensitivity of 90% and specificity of 68%. Melanomas could be separated from seborrheic keratosis with a reported sensitivity of 90% and specificity of 68% (90). The specificities were 15%, 17% and 25% for a sensitivity of 99%, when three distinct discrimination tasks were investigated: melanoma vs pigmented benign lesions, all cancers vs benign lesions and melanoma vs seborrheic keratosis, respectively. In 2012, Silveira *et al*, reported an in-vivo study using a Raman fiber probe in which they demonstrated differentiation of BCC from normal skin with an accuracy of 85% (99). Lim *et al*, determined the diagnostic capability of a multimodal spectral diagnosis for in-vivo non-invasive disease diagnosis of melanoma and non-melanoma skin cancers. Measurements were performed with a custom-built clinical system that combines three fiber optic-based optical spectroscopy modalities: diffuse optical spectroscopy, laser-induced fluorescence spectroscopy, and Raman spectroscopy. Raman, fluorescence and reflectance spectra were acquired from 137 lesions in 76 patients. From the measured set, the number of lesions considered for the study were 100 (12 melanomas, 19 BCC, 38 SCC, 14 actinic keratosis and 17 nonmelanoma pigmented lesions). When combining the three modalities, they reported a sensitivity of 100% and specificity of 100% for classifying melanoma vs non-melanoma pigmented lesions. BCC and SCC vs actinic keratosis were classified with a sensitivity of 95% and specificity of 71% also when combining the three modalities (100). In 2015, using a multi-fiber Raman probe, Schleusener *et al*, performed in-vivo measurements on 104 subjects with lesions clinically suspected of being skin cancer (36 melanomas, 39 BCC and 29 SCC). Additionally, 67 measurements on benign pigmented nevi from 33 subjects were also included. Sensitivity and specificity for discriminating histopathologically confirmed melanoma from lesions clinically suspected of being melanoma (not histopathologically confirmed) were 52% and 67%, respectively. For discriminating histopathologically confirmed BCC from lesions clinically suspected of being BCC (not histopathologically confirmed) the sensitivity was 54% and specificity was 48%. The results for discriminating histopathologically confirmed SCC from lesions clinically suspected of being SCC (not histopathologically confirmed) were sensitivity of 52% and specificity of 27%. Discriminating histopathologically confirmed malignant lesions from lesions clinically suspected of being skin cancer, but not histopathologically confirmed, was not successful (93). Zhao *et al*, in 2015, performed an independent clinical test on a total of 645 lesions from 409 patients. The sensitivity and specificity for discriminating skin cancers and pre-cancers (including melanoma, BCC, SCC, and actinic keratoses) from benign skin disorders were 99% and 24%, respectively. This study provided an independent confirmation

of in-vivo skin cancer diagnosis by Raman spectroscopy (92). Santos *et al*, measured 82 freshly excised melanocytic lesions suspected of melanoma (89). The measurements were performed using an in-house built Raman micro spectrometer optimized for measurements on pigmented skin lesions (101). All 24 melanomas were correctly identified with a specificity of 45%. The authors indicated that Raman spectroscopy might lead to a 3-fold reduction of the ratio of unnecessary skin excisions and that their results should encourage the use of Raman spectroscopy in-vivo systems by general practitioners and non-experienced dermatologists to discriminate melanoma from suspicious lesions and reduce unnecessary skin excisions (89). In 2017, Bratchenko *et al*, tested a combination of Raman spectroscopy with auto-fluorescence for melanoma and BCC diagnosis. They performed ex-vivo measurements on 39 melanomas, 40 BCC's and respective healthy skin within the excised samples. The authors show that the combination of Raman spectroscopy with auto-fluorescence has an accuracy of 97.3% in discriminating BCC's from melanoma, whereas the determined accuracy for each modality separately is 79% (102).

*Raman applications for surgery guidance:* Kong *et al*, combined auto-fluorescence with Raman spectroscopy for intra-operative detection of BCC in skin. This approach was developed to reduce the measuring time of whole tissue sections during the Mohs surgery procedure. First, the auto-fluorescence images, which were taken at excitation wavelengths of 377 nm and 292 nm (corresponding to collagen and tryptophan excitation) were segmented. In this way, the normal dermis, which is dominated by collagen, was discarded and only the suspicious segments were sampled by Raman spectroscopy. Based on this approach, Kong *et al*, demonstrated that BCC could be automatically detected with a sensitivity of 95% and a specificity of 94% (94).

## Lung Cancer

*Clinical need:* Lung cancer is one of the leading causes of cancer-related deaths in the world, with an incidence of 1,824,701 and mortality rate of 1,589,925. Reasons for the high mortality rate are the fact that patients tend to be diagnosed at an advanced stage and a lack of effective treatments. Part of the diagnostic process is white light bronchoscopy (whether or not combined with auto-fluorescence) combined with tissue biopsy for definitive pathology. A problem with this technique is that it suffers from either low sensitivity or specificity (103) and it is mainly accessible for centrally located lesions. Moreover, the representativeness and quality of the transbronchial and endobronchial biopsies is difficult to assess during the procedure (104). Cytologic evaluation also plays an important role in the initial

evaluation and diagnosis of patients with lung cancer, especially in the evaluation of suspicious lymph nodes (105). Sampling errors and numerous mimics are the main pitfalls of the technique (105). An objective optical tool that could be adapted to bronchoscopy or incorporated in a biopsy needle would be beneficial for biopsy guidance and early diagnosis of lung cancer. In early stage disease, surgical management is the treatment of choice. Several studies showed better 5-year survival rate for lobectomy (complete removal of the pulmonary lobe where the tumor is situated) than for sublobar resection, where less than an entire pulmonary lobe is removed (106-108). The sublobar resection procedure has been adopted in a number of centers. This procedure has been used for diagnosis and is considered sufficient for early stage disease and for non-cancerous lesions. Technical limitations that preclude negative surgical margins are a more challenging issue for sublobar resection than conventional lobectomy (108). Ideally, complete tumor resection with resection margins of  $\geq 2$ cm by sublobar resection would be favorable, maintaining lung volume and function (108) while reducing the risk of local recurrence. Intra-operative frozen section has traditionally been the sole modality for achieving negative resection margins. However, in some cases, frozen sections are not representative enough to predict the final pathology. Thus, the histopathological evaluation of the frozen section is difficult, especially between non-invasive stage of the disease and minimally invasive stage (109). The difficulty to predict the predominant pattern based on frozen section has been reported to be due mostly to sampling errors (110). Moreover, the intra-operative assessment of margins is challenging owing to an underestimation of the margin distance in lung tissue. If the tumor is peripheral, it is easier to guarantee a large resection margin. However, when the tumor is centrally located it is more challenging to assure that adequate resection margins are achieved. Improvement of intra-operative assessment of resection margins is essential to amend sublobar surgery and reduce the local recurrence rate.

*Raman applications for early diagnosis/biopsy guidance:* The first study that demonstrated the technical feasibility of measuring in-vivo lung lesions using Raman spectroscopy was conducted in 2008 by Short *et al*, (111). A multi-fiber Raman probe was implemented to complement white light and auto-fluorescence bronchoscopy for in-vivo detection of lung cancer. Preliminary research on 26 patients demonstrated that the combination of Raman spectroscopy with white light bronchoscopy and auto-fluorescence bronchoscopy can improve the diagnostic specificity of lung cancer (reducing the number of unnecessary biopsies). With these combined technologies, the sensitivity and specificity achieved were above 90% for detection of lung cancer and high-grade dysplasia lesions. The authors stated that the use of Raman spectroscopy has potential for substantially reducing the number of false-positive biopsies associated with white light bronchoscopy and auto-

fluorescence bronchoscopy (112). Recently, the same group used the bronchoscopic Raman spectroscopy in-vivo in 80 patients (280 samples), using signal acquisition times of 1s. The detection of high grade dysplasia and malignant lung lesions resulted in a reported sensitivity of 90% at a specificity of 65% (113).

## Esophageal Cancer

*Clinical need:* Esophageal cancer has a worldwide incidence rate of 455,784 and mortality rate of 400,169 (114). There are two main types of esophageal cancer: squamous cell carcinoma and adenocarcinoma. Diagnosis is established with endoscopic guided biopsy. Esophageal adenocarcinoma develops in sequential stages of change in the mucosa. Firstly, there is a change from a normal squamous epithelium to a columnar cell epithelium (i.e. intestinal metaplasia), known as "Barrett's esophagus". The "Barrett's esophagus" is considered a pre-malignant stage because it is associated with 100 times higher risk of developing esophageal cancer (115). Endoscopic identification of this pre-cancerous stage may enable early, minimally invasive therapeutic intervention (i.e. endomucosal resection). The greater the number of biopsies taken from the border of the lesion (at least six), the higher the diagnostic accuracy (116,117). However, the increase in the number of biopsies performed may cause an increased risk of complications, such as gastrointestinal bleeding. Furthermore, still 11.3% of upper gastrointestinal tract cancers are missed with this technique (118). Therefore, an objective, real-time tool for biopsy guidance could reduce the number of unnecessary biopsies and improve the diagnostic accuracy. Surgical resection is the treatment of choice in early staged esophageal cancer. The optimal extent of esophageal resections is still controversial, but completeness of surgical resection is an important determinant for a better outcome. There are recommendations for clearance of tumor from proximal and distal margins, but this may vary depending upon the type of tumor (119,120). The presence of tumor at a distance  $\leq 1$  mm of the circumferential resection appears to be a significant cause of local tumor recurrence and decreased survival (121,122). An intra-operative assessment of the resection margins of esophageal excisions is essential to reduce the local recurrence rate and increase the survival rate.

*Raman applications for early diagnosis/biopsy guidance:* Teh *et al*, studied 21 dysplastic gastric lesions and 44 normal samples from 44 patients using in-vivo multi-fiber Raman probe system. A sensitivity of 95% and specificity of 91%, between dysplastic and healthy stomach tissue was found (123). Bergholt *et al*, measured 924 Raman spectra in-vivo from normal tissue and 111 from benign ulcers from 71 patients with an endoscopic multi-fiber Raman probe system. Malignant ulcers were correctly classified with a sensitivity of 82.1% and a

specificity of 95.3% (124). An endoscopic multi-fiber Raman probe system for in-vivo and online diagnosis of gastric cancer was developed by the group of Huang (125). Using this system, they obtained a total of 2748 in-vivo gastric tissue spectra from 305 patients: 2465 diagnosed as normal and 283 as cancer. The reported diagnostic accuracy for gastric cancer was 85.6% (sensitivity of 80.5% and specificity of 86.2%). Gastric cancer detection algorithms were further applied on 10 patients undergoing gastroscopy (Figure 1). The authors report a predictive accuracy of 80.0% (sensitivity of 90.0% and specificity of 73.3%) (125). In 2014, Bergholt *et al*, performed an in-vivo study for diagnosis of gastric dysplasia in Barrett's esophagus. A total of 450 patients underwent endoscopy in the upper gastrointestinal tract, Raman measurements were performed, biopsies were taken and submitted for histopathological evaluation. High grade dysplasia in Barrett's esophagus, non-dysplastic Barrett's esophagus and normal columnar lined epithelium could be discriminated with a reported sensitivity of 87% and a specificity of 84.7% (126). Wang *et al*, demonstrated that, using the in-vivo endoscopic multifiber Raman probe system and acquisition times of 0.1-0.5s esophageal squamous cell carcinoma can be detected with sensitivity of 97% and specificity of 97%, based on the results from 48 patients (127).

Ishigaki *et al*, used a micro Raman probe system to examine ex-vivo early-stage (stages 0 and I) esophageal cancer samples from 15 patients. They demonstrated a sensitivity of 81% and a specificity of 94% using leave-one-out cross validation (128). Using a Raman endoscopic multi-fiber probe during routine endoscopy examination, Lin *et al*, demonstrated in-vivo that simultaneous use of the fingerprint and high-wavenumber part of the Raman spectrum can improve early diagnosis of gastric precancers (sensitivity of 93% and specificity of 94%) in an independent dataset.

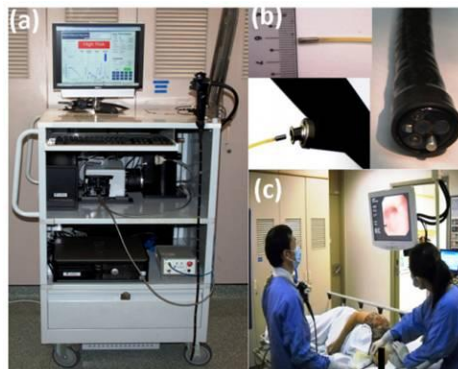


**Figure 1. (a) Photograph of Raman endoscopy system in clinic; (b) insertion of the 1.8 mm Raman endoscopic probe into the working channel of an endoscope during**

**gastroscopy; and (c) routine Raman endoscopy procedure in clinic (125). From Duraipandian *et al*, (125). Reprinted with permission from SPIE.**

A total of 48 patients were included. From this dataset, 80% of the spectra were used for training and 20% for testing. Using exclusively either the fingerprint or the high-wavenumber part, the area under the ROC curve was 0.972 and 0.928, respectively. When combining fingerprint spectral range and high-wavenumber range, the area under the ROC curve was 0.995 (129).

## **Head and Neck Cancer**

*Clinical need:* Head and neck cancer includes cancer of the oral cavity, nasopharynx, oropharynx, hypopharynx, and the larynx. Head and neck cancer has an overall incidence rate of 686,328 and a mortality rate of 375,665 (114). The most frequent type of cancer in head and neck region is oral cavity squamous cell carcinoma (OCSCC). When a patient is suspected for a tumor in the head and neck region, all subsites will be examined to screen for a synchronous second primary tumor. Biopsies are taken for tissue diagnosis and for staging purposes. Surgery is the mainstay of treatment for most oral cancers and for early stages in the other subsite. Advanced disease usually requires multimodality treatment consisting of surgery, radiation and/or chemo/biotherapy. Very recently immunotherapy was added as a promising option. An acceptable balance between remaining function and physical appearance on one side and clear margins on the other, is the main goal of surgery. Inadequate resection margins influence negatively local control and prognosis (130,131). In head and neck cancer, clear resection margins impact on disease control and survival (132,133). Achieving adequate resection margins is challenging. The lack of reliable intra-operative guidance and the proximity of tumors to vital structures are common causes of inadequate tumor resection. Recent studies show poor surgical success rates with inadequate tumor resection in oral cavity cancer surgery from 30% up to 85% (23,33,134). Intra-operative assessment by means of frozen-section is the standard procedure. However, these can only be used for soft tissue and not for bone. Additionally, only a small proportion of the resection margins can be investigated by this procedure and the selection of suspicious tissue depends on the surgeon's and/or the pathologist's experience. These factors also contribute to a high recurrence rate of oral cancer (21,135). The two primary clinical needs are early diagnosis of OCSCC and intra-operative assessment of the complete resection margins, not only for soft tissue but also for bone margins.

Raman applications for early diagnosis/biopsy guidance: In 2014, Krishna *et al*, created an in-vivo multi-fiber Raman probe system and measured a total of 28

healthy volunteers and 171 patients with oral lesions. Spectra were annotated, based on histology or by clinical assessment, as oral squamous cell carcinoma (OSCC), oral submucosa fibrosis (OSMF), oral leukoplakia (OLK) and normal mucosa. Each group (OSCC, OSMF, OLK and normal) was correctly classified, when applying the developed diagnostic algorithm, in 89%, 85%, 82% and 85% of the cases, respectively (136). In 2015, Guze *et al*, conducted an in-vivo pilot study with a Raman probe and measured oral diseases from 18 patients. Benign and malignant oral lesions were classified correctly with sensitivity of 100% and specificity of 77% using a multi-fiber Raman probe. Although, a larger study group was preferable, the results indicate that Raman spectroscopy is a promising diagnostic tool (137).

*Raman applications for surgery guidance:* In 2015, the feasibility of identifying oral cancer tumor based on water concentration was demonstrated ex-vivo, using high-wavenumber Raman spectra obtained from freshly excised resection specimens from oral cavity (135). Barroso *et al*, investigated how the water concentration changes across the border between tumor and the healthy surrounding tissue on ex-vivo specimens from patients that underwent surgery for oral cavity squamous cell carcinoma. Measurements were performed on 20 patients using a confocal Raman microscope system. The results revealed consistent changes in the water concentration across the tumor border. Over distances of 4 to 6 mm across the tumor border, water concentrations changed from 76%  $\pm$ 8% in the tumor to 54% $\pm$ 24% in the healthy surrounding tissue (138).

## Brain cancer

*Clinical need:* The estimated incidence of brain cancer in the developed world is 7.1/100,000 with a high mortality of 5.3/100,000 (1). Neuroradiology is usually sufficient as the initial diagnostic modality for brain cancer. In some cases, stereotactic biopsy is needed to decide for primary resection versus chemoradiation. For accurate histopathological diagnosis multiple tissue samples are obtained (139). Brain biopsy may be complicated by sampling error and cerebral hemorrhage (140,141). Therefore, a rapid and objective tool is needed for optimal biopsy guidance to provide one representative brain tumor tissue sample, thus minimizing the risk of cerebral hemorrhage. Treatment of choice for most primary brain cancer is surgery (17). In low-grade gliomas the extent of tumor tissue resection is associated with improved patient outcome (141-143). Three-dimensional stereotactic navigation, 5-ALA-fluorescence and intra-operative magnetic resonance imaging (MRI) are currently used to achieve optimal surgical results (141,144). Unfortunately, distinguishing cancer from healthy tissue during surgery still is a challenge (140,145). Generally, postoperative MRI demonstrates residual tumor in

69.6% of the cases (145). The accuracy of navigation is influenced by the intent to preserve vital brain structures, inter-observer disagreement on the tumor transformation zone, and brain edema (146). In the current practice, adoption of navigation techniques is limited owing to high costs and hampered by low evidence of survival benefit (147). An optical, intra-operative tool to guide the surgeon towards tumor tissue in stereotactic biopsy and to identify adequate resections while preserving function brain structures with resection may improve patient outcome.

*Raman applications for surgery guidance:* Jermyn *et al*, in Montreal have developed a Raman system with a hand-held probe for intra-operative use during brain tumor resection. In an in-vivo study, spectra were obtained from 17 patients with 0.2s acquisition time (Figure 2). Patients with grade 2 to 4 gliomas were included (66 normal spectra and 92 cancer spectra). They reported a sensitivity of 93% and a specificity of 91% in distinguishing normal brain tissue from dense cancer and normal brain invaded by cancer cells (148).

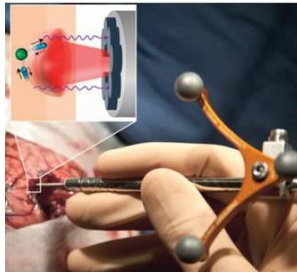


**Figure 2.** The handheld contact fiber-optic probe for Raman spectroscopy. The probe (Emvision, LLC) was used to interrogate brain tissue during surgery. A schematic diagram illustrated the excitation of different molecular species, such as cholesterol and DNA, to produce Raman spectra of cancer versus normal brain tissue (52). From Jermyn *et al*, (52). Reprinted with permission from the authors and AAAS.

## Colorectal Cancer

*Clinical need:* Colorectal cancer (CRC) has a worldwide incidence rate of 1,360,602 and mortality rate of almost 700,000 (1). CRC is diagnosed after onset of symptoms or through screening by colonoscopy (149). Screening detects early-stage malignancies or premalignant polyps (adenomas) and improves prognosis for the patient (149). Colonoscopy miss rates are 2-6% for CRC and 20-26% for adenomas (150,151). Additionally, many polyps with minimal malignant potential are removed

without benefit to the patient (149,152). Despite its contribution to the effectiveness of colonoscopy, polypectomy is associated with increased risk of major complications (perforation, hemorrhage) (153). An objective biopsy guidance tool is therefore of clinical importance to reduce these limitations. Surgery is the only curative modality for localized colon cancer. Proximal and distal resection margins should be at least 5 cm from the tumor (154). Satisfyingly, positive margins in colon cancer resections are rare (155). The most important indicator of outcome following resection of colon cancer is the tumor pathologic stage (156).

*Raman applications for early diagnosis/biopsy guidance:* In 2008, Widjaja *et al*, measured 105 colon specimens ex-vivo with an inhouse built Raman probe (157). From the 105 colon specimens 41 were normal, 18 were hyperplastic polyps and 46 were adenocarcinomas. In this study, the diagnostic accuracy was 98% (157). Short *et al*, conducted a study using Raman spectroscopy on ex-vivo colon tissue from 18 patients, measuring both the fingerprint and high-wavenumber spectral regions. The results indicated that, using the high-wavenumber region, the non-malignant and the malignant groups could be classified correctly with a specificity of 89%. The authors referred that high-wavenumber region could be used in-vivo to improve the identification of neoplastic lesions (158). Bergholt *et al*, tested the same approach in-vivo (combined fingerprint and high-wavenumber spectral regions) on adenomatous polyps measured from 50 patients using an endoscopic multi-fiber Raman probe. Adenomatous polyps were separated from hyperplastic polyps with a sensitivity of 91% and specificity of 83%. The authors demonstrated that the analysis based on the combination of fingerprint and high-wavenumber spectral regions is superior to considering either region alone (12).

## Cervical Cancer

*Clinical need:* Cervical cancer has a worldwide yearly incidence of 528,000 women and mortality of 266,000 (1). In recent years incidence and mortality rates have decreased because of the emergence of screening (159). The primary method of screening is by cervical cytology with the Papanicolaou test (PAP). This has a high specificity (95–98%) but a low sensitivity (<50%) (160). This sensitivity of screening is increased by testing for Human Papilloma Virus (HPV) in the cervical swab (161). Final diagnosis of cervical cancer is based on histopathology. For this colposcopy guided biopsy is recommended, with a sensitivity of 92% and specificity of 67% (73). In low resource settings visual inspection of the cervix with biopsies is used with a specificity and sensitivity of 88-92% and 10-84% (162,163). Treatment of cervical cancer is based on stage. Small tumors will be treated by surgery, and higher stages with chemoradiation. It is not to be expected that Raman spectroscopy

has any value in the diagnostic or treatment of cervical cancer since the diagnostic accuracy of colposcopy guided biopsies will not be improved and precision treatment is not applicable for cervical cancer.

*Raman applications for early diagnosis/biopsy guidance:* Mo *et al*, measured Raman spectra from 46 patients in-vivo with high-wavenumber Raman spectroscopy, to investigate cervical precancer diagnosis. The Raman instrument used a ball-lens fiber-optic Raman probe. Cervical dysplasia could be distinguished from normal tissue with a reported sensitivity of 94% and specificity of 98% (164). Kanter *et al*, performed a clinical study on a total of 43 patients that underwent colposcopy-guided biopsy to investigate dysplasia. Using a portable Raman system with a fiber-optic probe spectra were acquired of low grade squamous intraepithelial lesions, high grade squamous intraepithelial lesions, metaplastic lesions and normal tissue. The classification accuracy for discriminating diseased from normal tissue was 88%, the sensitivity was 86% and the specificity was 97% (165). The same group reported, in 2011, a sensitivity of 70% and a specificity of 83% for cervical pre-cancer diagnosis. In this study a total of 29 patients were included. Measurements were done in-vivo using fiber-optic Raman probe with a ball-lens (166). To improve diagnostic accuracy, Duraipandian *et al*, combined high-wavenumber and fingerprint Raman spectroscopy for cervical and pre-neoplasia detection. The obtained sensitivity and specificity were 85% and 81.7%, respectively (167). Rubina *et al*, performed ex-vivo Raman measurements on 49 abnormal cervical specimens and 45 negative control cytology samples using a fiber-optic Raman microprobe system. Abnormal lesions were classified correctly in 84.5% of the cases. The authors suggested that presence of blood in abnormal specimens was a major cause of discrimination (168,169).

## **Vulvar Cancer**

*Clinical need:* Vulvar cancer has a worldwide incidence of 1,300 women and mortality of 450 women per year (170). This malignancy has a high curability in early-stage disease, but a poor prognosis for advanced-stage disease and recurrent disease. Diagnosis is based on histopathology of a biopsy of the vulva at the peripheral edge of the lesion (171), whereby underlying stroma is included, and possible necrotic tissue avoided (172). In-vivo diagnosis and biopsy guidance can be of great value for accurate diagnosis. Surgery is the main choice of treatment. In recent years surgical management has changed, were large radical and disfiguring resections make place for conservative surgery (172). The multifocality of this type of cancer, the presence of dysplasia and/or small resection margins result in local recurrence rates of 23-50% (173,174). Surgical management of vulvar carcinoma

aims to achieve a fine balance between adequate resection margins and preservation of sexual and urinary function (172,175). An intra-operative tool for surgery guidance is therefore needed.

*Raman applications for early diagnosis/biopsy guidance:* During the literature search we have noticed that Raman applications have not been greatly developed for vulvar cancer. The most recent study, was developed by Frost *et al*, (176). They have evaluated the diagnostic performance of Raman Spectroscopy for differentiating a pre-malignant vulvar lesion (lichen sclerosus, LS) from other inflammatory vulvar conditions in fresh vulvar biopsies from 27 women. Biopsies resulted in circular discs of skin 3-4 mm in diameter (full thickness of the epidermis with underlying dermal tissue). Spectra were measured with a Raman micro-spectrometer (modified Renishaw system 1000 dispersion), which was coupled to a diode laser of 830nm excitation wavelength and had a spot size of 15x17 $\mu$ m. A classification model was created using principal components and multivariate linear discriminant analysis. Leave one sample out cross validation was used to validate the model. The model was able to correctly differentiate LS from other inflammatory vulvar conditions with a sensitivity of 91% and specificity of 80%. The authors suggested that the study demonstrates that Raman spectroscopy has potential for in-vivo non-invasive diagnosis of vulvar skin conditions and when applied in the clinical setting may reduce the need for invasive tissue biopsy (177).

## Bladder Cancer

*Clinical need:* The global incidence rate for bladder cancer is 430,000 and mortality is 165,000 (1). The standard for diagnosis is cystoscopy, with biopsies of suspicious lesions, and transurethral resection (TUR) to confirm the diagnosis (178). Unfortunately, small papillary bladder tumors and flat urothelial carcinoma-in-situ (CIS) can easily be overlooked (179). This contributes to increased residual rates and a recurrence rate of 50% within 18 months. TUR is the standard of treatment for small (Ta) bladder tumors. Incomplete resection results in a second operation and/or increased recurrence rate, resulting in poor long-term prognosis (180-183). Thereby, high risk tumors grow fast with a mortality rate of 50%, despite treatment. Urinary markers are emerging but not able to outperform cystoscopy. These findings suggest that in-vivo biopsy, biopsy guidance and surgery guidance is needed for early detection, accurate diagnosis and adequate resections, to improve patient outcome.

*Raman applications for early diagnosis/biopsy guidance:* The first in-vivo Raman probe that was used in bladder was an Emvision® probe with a filtered six-around-one fiber configuration. The excitation wavelength was 785nm. The probe used had a large measurement volume (~1cm<sup>3</sup>) and did not have any lenses.

As a result, the probe collected Raman spectra not only from the upper urothelium surface of the bladder (where transitional cell carcinoma has its origin) but also from deeper layers. During the procedure of transurethral resection of bladder tumors (TURBT), spectra were collected from suspicious and non-suspicious locations (collection times of 1 to 5s). Bladder cancer could be distinguished from normal bladder with a reported sensitivity of 85% and a specificity of 79%. Even though the results show the possibility of discerning normal from malignant bladder tissue using Raman spectroscopy, the authors suggest that using a Raman probe that collects shallower signal from the urothelium surface of the bladder would be ideal for early diagnosis. Also, the combination of auto-fluorescence with Raman spectroscopy could potentially improve the diagnostic capability, by using the sensitive auto-fluorescence modality to indicate suspicious regions for “optical biopsy” by the highly specific Raman spectroscopy modality (184,185). In 2012, a confocal Raman probe was designed by Barman *et al*, and it was used *ex-vivo* for bladder cancer diagnosis in 14 patients. The confocal probe had depth of field of approximately 280 $\mu$ m. The result of the confocal system had a significantly higher specificity with respect to large-volume Raman spectral data, with a sensitivity that was comparable to the large-volume Raman system (60,177).

## **Prostate Cancer**

*Clinical need:* Prostate cancer is among the most common cancers in men worldwide, with an incidence of 1,094,916 and mortality rate of 307,481 (1). The diagnosis of prostate cancer is often made through transrectal ultrasound guided prostatic biopsy (186). Ten to twelve core biopsies are recommended, with > 12 biopsies not being significantly more conclusive (187,188). While the majority of prostate cancer patients are treated by radical prostatectomy or radiation therapy, an increasing number of men are actively surveyed for their disease without immediate treatment. In a significant number of men, radical prostatectomy is complicated by urinary and/ or erectile dysfunctions, which is related to eradication of the neurovascular bundles (NVB) localized in the dorsolateral peri-prostatic fat tissue. Operative removal of the prostate leaving the NBV intact can reduce post-operative complications. Decision making on nerve-sparing surgery can be optimized by intra-operative assessment of the prostatic surgical margins. In practice, the urologist can only remove the prostate initially leaving the NVB in situ. In case intra-operative assessment of the prostatic surgical margin is negative, the NVB will remain intact; in case the margin is positive the urologist can remove the NVB at a second term. Although intra-operative frozen-section assessment is able to increase nerve-sparing surgery from 81% to 97%, it is labor-intensive requiring an optimized work-flow for the fast throughput of a large number of frozen sections 189. Intra-operative

assessment of surgical margins using Raman spectroscopy might be a good alternative for extensive pathologic frozen sections and could be implemented at large scale in operation theatres or departments of pathology.

*Raman spectroscopy applications:* Spontaneous Raman spectroscopy has not been explored yet in-vivo and/or ex-vivo using human prostate cancer material. Raman-based studies were developed in the last years in-vitro, using cell cultures and, more recently, ex-vivo using peripheral nerves of rats (177,190,191).

## Instrumentation

When developing instrumentation for in-vivo and ex-vivo applications, the main technical problems are: speed of measurement, adaptation in clinical workflow, interference of background from tissue auto-fluorescence and high instrumentation costs. In the last years we consider that the major technological advances in Raman spectroscopic systems for clinical applications have been in: 1) detector technology, 2) fiber-optic probe design, 3) combination with other techniques, and 4) new laser opportunities for low-cost systems.

### 1) InGaAs detectors for short-wave infrared Raman spectroscopy

Until now the detection of Raman signals in the short-wave infrared (SWIR) region ( $>1100$  nm) was constrained by limitations of the state-of-the-art detector technology for visible to NIR excitation (CCDs). An alternative in this spectral range is the Indium-GalliumArsenide (InGaAs) detector, which enables detection at wavelengths well above 1100nm. Several companies have recently moved towards the SWIR range, and have introduced InGaAs-based Raman devices (e.g. Andor™, Anton Paar™, Horiba™, B&W Tek™). Xenics™ introduced an InGaAs camera that has a read-out noise at comparable levels as a CCD detector, and that consequently can achieve shot-noise limited Raman spectra in clinically acceptable integration times (101). This development in detector technology enabled the use of longer excitation wavelengths for clinical applications on tissues with would otherwise suffer from strong laser-induced fluorescence of fluorophore-containing tissues. Santos *et al.*, could measure melanocytic skin lesions without overwhelming tissue auto-fluorescence interference using a SWIR Raman system, with NIR 967nm laser and an extreme low-noise InGaAs detector (Figure 3) (89).

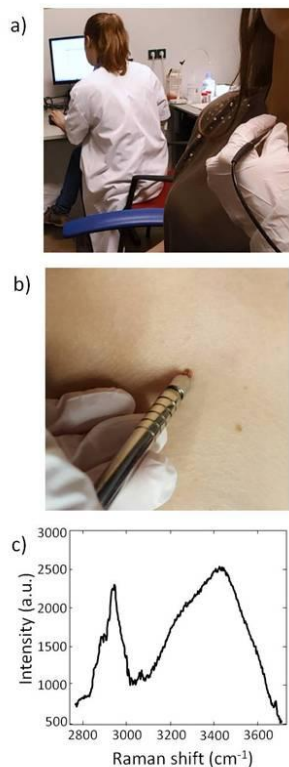


**Figure 3. Implementation of SWIR Raman system in the dermatology out-patient clinic of Leiden University Medical Center for in-vivo measurements (a). Photograph of a pigmented skin lesion (b). This was measured using a 976-nm laser excitation, the SWIR Raman instrument and a single fiber probe. The corresponding Raman spectrum measured in-vivo is shown in (c). Exposure time: 30 s.**

Also, Patil *et al*, and Pence *et al*, have reported dispersive Raman spectroscopy of tissues with strong auto-fluorescence (liver and kidney human tissues) using 1064 nm excitation in combination with an InGaAs detector array (192,193). Laser-induced tissue fluorescence was significantly reduced compared to excitation with lasers in the visible wavelength range.

## 2) Fiber-optic probes

*Fiber-optic probes for early diagnosis:* Fiber-optic probes have enabled the use of Raman spectroscopy for in-vivo clinical applications. The integration of Raman spectroscopy with other diagnostic techniques has been a major step in the development towards improved efficiency in biopsy guidance and early cancer

diagnosis. Fiber probes that could be inserted into endoscopic channels enabled in-vivo measurements in hollow organs or surface assessment of solid organs: oral cavity (136,137), lung (111,113), upper gastrointestinal tract (123-127,129), colorectal (12,158), bladder (185), and cervical cancers (164-167,194). Also, handheld fiber-based systems have been used for in-vivo assessment of skin cancer (88,90,91,94–96), and of brain cancers (148,195). In the last years numerous Raman probe designs have been developed, optimized and tested for clinical purposes. There has been an increased effort to tailor Raman probes to clinical needs and constraints defined by the specific clinical targets, specific pathophysiology of diseases, and specific anatomies of the region of interest (e.g. accessibility of the tissue, sample size, sampling depth).

Stevens *et al*, and Wang *et al*, have reviewed Raman fiber-optic probe designs and construction concerns, considering different oncological applications and respective clinical needs (18,196). Depth-selective fiber-optic Raman probes have been investigated for use in epithelial tissue associated with dysplasia (197). Wang *et al*, developed a confocal fiber-optic Raman probe coupled with a ball lens to enhance in-vivo Raman measurements from gastric premalignant epithelial tissue during endoscopy (197,198). With a beveled fiber-optic probe coupled with a ball lens, the authors could limit their collection depth to 300  $\mu\text{m}$ . Since gastric dysplasia initially evolves in the epithelial tissue layer ( $\sim 300 \mu\text{m}$ ), it is especially relevant for selective interrogation of the gastric epithelium. Further work from the same group, featured a fully automated real-time Raman spectral diagnostics framework integrated with a multimodal image-guided Raman technique that enabled real-time in-vivo cancer detection at routine endoscopy procedure, as shown in Figure 1 (199). The same fingerprint/high-wavenumber fiber-optic Raman endoscopic system was developed further by Bergholt *et al*, for routine clinical colonoscopy diagnosis, making use of a foot pedal control switch and an auditory feedback to the gastroenterologist (199). Using a similar probe in a hand-held confocal design, Duraipandian *et al*, measured in-vivo fingerprint and high-wavenumber Raman spectra during colposcopy (167). Agenant *et al*, used a novel clinical Raman probe for sampling superficial tissue to improve in-vivo diagnosis of (superficial) urothelial carcinoma. This probe had a measurement depth of 0-200 $\mu\text{m}$ , which corresponds to the average urothelium depth. The probe is comprehended by 7 collection fibers, 1 excitation fiber and two component front lens (200).

*Fiber-optic probes for guided surgery:* In the field of brain cancer, Jermyn *et al*, performed in-vivo Raman measurements during human brain cancer surgery for real-time identification of invasive cancer, using a handheld contact Raman spectroscopy probe (52,195). Each measurement covered a 0.5mm diameter tissue

area with a depth sampling up to ~1 mm in 0.2s. During the tumor resection, Raman signals were measured in the surgical cavity.

The probe is comprehended by filters that were placed directly at the tip of the optical fibers. The spectra acquired with the handheld Raman probe (Figure 2) do indicate that there are still some challenges in developing probes and methods for correcting for spectral distortions mainly caused by the filter characteristics of the probes and subtraction of fluorescence signal backgrounds (201). A Raman system comprehended by a single fiber needle probe is currently being tested ex-vivo by Head and Neck surgeons and pathologists from Erasmus University Medical Center Rotterdam, The Netherlands. This probe aims intra-operative inspection of the entire resection margin of specimens from patients that underwent surgery for oral cavity SCC (Figure 4).

### **3) Combined Raman systems for guided surgery**

In the field of dermatology, Kong *et al*, developed a scanning device that combines auto-fluorescence imaging and Raman spectroscopy to guide Mohs micrographic surgery in the excision/treatment of high-risk skin basal cell carcinoma (94). Although Mohs micrographic surgery provides the highest cure rates, it is a time-consuming technique (1 - 3 hours) needing highly trained personnel.

With the purpose of reducing the duration of scanning large areas of tissue, tissue auto-fluorescence imaging is used to determine the main spatial histological features of the sample, and this information is used to select and prioritize the sampling points for Raman spectroscopy (Figure 5) (94,202).

### **4) New lasers**

Recent developments in vertical-external-cavity surface-emitting laser (VECSEL) technology have brought their characteristics in the realm of Raman spectroscopy, with special interest for low-cost hand-held devices (203). VECSELs are semiconductor lasers based on a vertical-cavity surface-emitting geometry.

These types of lasers achieve a combination of high continuous wave output power, due to a large gain area, and a low- divergence near-diffraction-limited beam, due to the transverse mode control of the extended cavity. The advantages of VECSELs over edge emitting semiconductor lasers are circular output beam, easy array fabrication, small size, and low cost at mass production (56,203-205).

## Transferability

The Raman applications described above demonstrate potential of Raman spectroscopy to affect patient care. The major requirements for translation of a Raman equipment into clinical practice are: 1) well defined clinical need, 2) patient benefit proven and/or cost benefit, 3) equipment changes clinical practice, 4) demonstrated safety, reproducibility, robustness, and reliability (e.g. large clinical trials) and 5) regulatory approval. First, it is important to verify beforehand that the developed Raman application addresses an actual clinical need and that the application can provide results of clinical relevance. This does not mean that the Raman instrument needs to give perfect results, as long as it can bring about measurable and cost-effective improvements in patient care. Moreover, it is required that the instrument is introduced in the clinical workflow and is used/tested by clinicians.

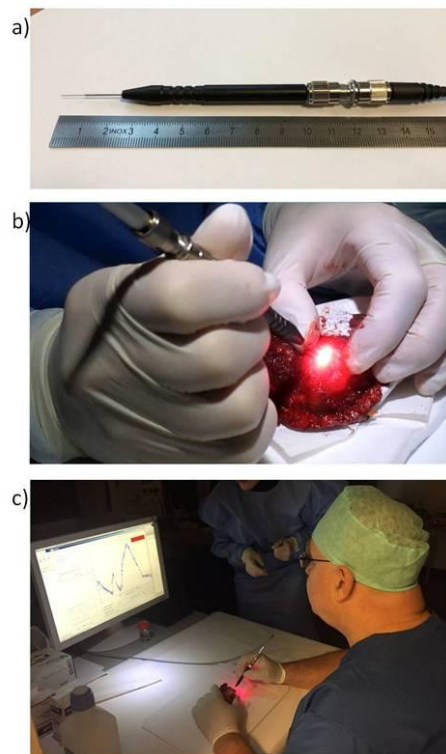


**Figure 4. Single fiber needle probe for intra-operative assessment of the oral cavity SCC resection margins, developed by Artphotronics GmbH in collaboration with RiverD International B. V. and Erasmus University Medical Center, Rotterdam. a) Close up of**

**the single fiber needle probe. b-c) Testing the single fiber needle probe for inspection of the freshly excised oral cavity specimens.**

Second, it is essential to demonstrate the safety, reproducibility, robustness, and reliability of the developed application in large clinical trials, to the end-users. And finally, receive approval from regulatory agencies. Many of these aspects are now increasingly being addressed, which is a good sign of progress in the field towards clinical translation. However, for this translation continued effort is needed by searching for close collaboration and input from the medical community.

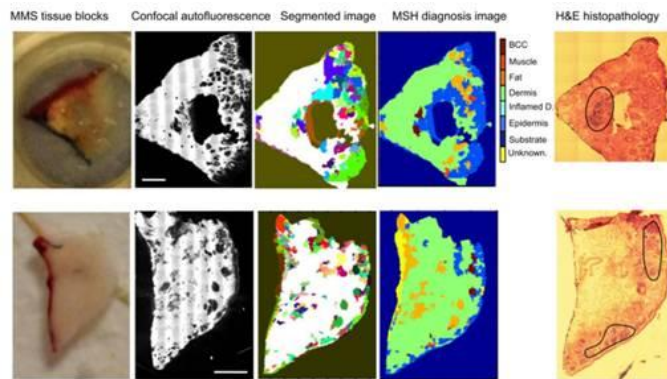


**Figure 5. Multimodal spectral histopathological diagnosis of BCC in unsectioned tissue blocks as received from surgery. H&E histopathology images for adjacent sections are included for comparison (Scale bars: 2 mm) (94). Reprinted with permission from the authors and PNAS.**

Additionally, to gain the confidence of clinicians to the potential value of Raman-based applications, it is essential to expose the results of Raman technologies over or in line with existing medical devices (2,206). This should be done in large cohorts' studies based on patient outcomes and in direct comparison with the current gold standards. Multidisciplinary networks are now being developed, such as the International Society for Clinical Spectroscopy (ClirSpec), European Photonics Industry Consortium (EPIC) and Raman4Clinics (EU COST Action BM1401), which target especially these translational aspects. ClirSpec is a society, comprehended by spectroscopists and clinicians, that facilitates and promotes the translation of spectroscopy into the clinical environment, for the general benefit of patients (clirspec.org). Raman4Clinics (EU COST Action BM1401) is a platform for scientific communication, exchange, collaboration and for new research activities, combining the partners' expertise in technology, component, system and methodology development and medical application (www.raman4clinics.eu). EPIC is a network that promotes awareness of opportunities for the European photonic

industry in healthcare (www.epic-assoc.com). To provide an overview of the current status of the technology towards clinical translation, we classified all reviewed R&D results, based on the TRL. Figure 6 (2008-2017) shows the result from the technology readiness classification of the different Raman studies mentioned in the Raman applications section. From this figure, it is immediately clear that the majority of the developed applications appears to get stuck in category B (TRL 4). These studies presented results of algorithms for (pre-) malignant tissue detection with data either collected in-vivo or ex-vivo with prototype Raman systems. However, validation of algorithms with an independent large dataset has not been proven yet. Some of the systems used in the analyzed studies are already further towards actual clinical use, and were classified as C, such as Zhao *et al.*, Wang *et al.*, Kong *et al.*, and Duraipandian *et al.* (92,94,125,127).

### **Development of commercial instruments for oncological applications**

We realized that most of the studies do not report a fully commercial product (ready to be used in the clinic). We therefore contacted the companies that are collaborating directly with the research groups presented in the Raman applications section. We also investigated the progress/potential interest of the companies which are developing or have developed commercial Raman spectroscopic systems for oncological applications. We received information from the following leading companies in Raman spectroscopy: Avantes B.V., B&W Tek, EmVision LLC, Invenio B.V., Horiba Jobin-Yvon Inc. (HORIBA Scientific), ODS Medical Inc., Renishaw, RiverD International B.V., Verisante Technology Inc., and WITec B.V.. Based on the information received we have created a future perspective of clinical translation, which is presented in figure 6 (2017-2021).

*Progress reported by companies:* B&W Tek has developed a Raman spectroscopic system, for the identification and qualification of cytostatics (in-vitro). B&W Tek is a company that provides instruments looking for R&D partners. Invenio Imaging Inc. is developing a stimulated Raman scattering microscope for histological examination of fresh tissue. The most recent publication was in Nature Biomedical Engineering, early 2017 (207). The perspective of the company is to have the equipment ready to be commercialized later this year. EmVision LLC does not manufacture or develop clinical systems, but the company is active in selling components, such as fiber-optic probes, to companies that are pursuing clinical systems. HORIBA Scientific is an active member of Raman4Clinics European project and provides research and analytical Raman instruments for all kind of applications, including oncology. ODS Medical Inc. is developing an in-vivo Raman

tool for surgical brain tumor resection (148,208-211). The company predicts that the system will be commercialized within approximately 3 years (in 2020) following approval by regulatory bodies, including FDA. Renishaw has been actively developing a Raman system for ex-vivo analysis of tissue cells and bio fluids for clinical use. The company is upgrading fiber-optic probe designs for clinical use during oncological surgery. This company has an ex-vivo Raman spectroscopy platform (InVia series, Renishaw, Gloucestershire, U.K.) for a number of life-science and clinical applications including tissue pathology, neurobiology, stem cell research. Renishaw is currently developing a fast tissue imaging platform, which is based on the RA802 Pharmaceutical Analyser, for measuring uneven tissue surfaces with a minimum of sample preparation (212-214). The new fast tissue imaging platform should be available in the summer of 2017.

RiverD International B.V. collaborates with the University of Nottingham in the development of an auto-fluorescence/Raman system for Mohs' micrographic surgery of basal cell carcinoma. Two prototype systems are currently being tested at the University of Nottingham, in UK, and at Erasmus MC University Medical Center Rotterdam, in the Netherlands. The systems are based on the concept described by the Nottingham group (94). RiverD International B.V. is developing a Raman tool for surgical guidance of Head and Neck tumor resection, which they predict to be ready for clinical trials in 2019. Currently, an ex-vivo fiber-optic probe system is being developed for intra-operative inspection of resection margins of excised tissue. The company is also collaborating in an R&D project that aims to the development of a Raman spectroscopic device for use by dermatologists and general practitioners for objective assessment of pigmented skin lesions clinically suspected of melanoma (89,101).

Verisante Technology Inc. is developing in-vivo Raman technology for clinical oncology applications focused on: 1) in-vivo non-invasive detection of skin cancers including melanoma and non-melanoma skin cancers; 2) endoscopy detection of cancers of internal organs such as lung cancers and gastro-intestinal cancers (90,111,113,215-217). Currently, Verisante Technology Inc. is commercializing a skin cancer detection device (Verisante Aura, see Figure 7) in Canada, Europe and Australia. Aura systems are being in use in several clinics in Canada. In figure 6, Verisante Aura is identified by [\*]. WITec B.V. develops and commercializes confocal Raman microscope systems. The company is not actively involved in development of applications in the clinical oncology field. However, various users of the confocal Raman microscopes have applied their instruments in oncology-relevant research (218-221).

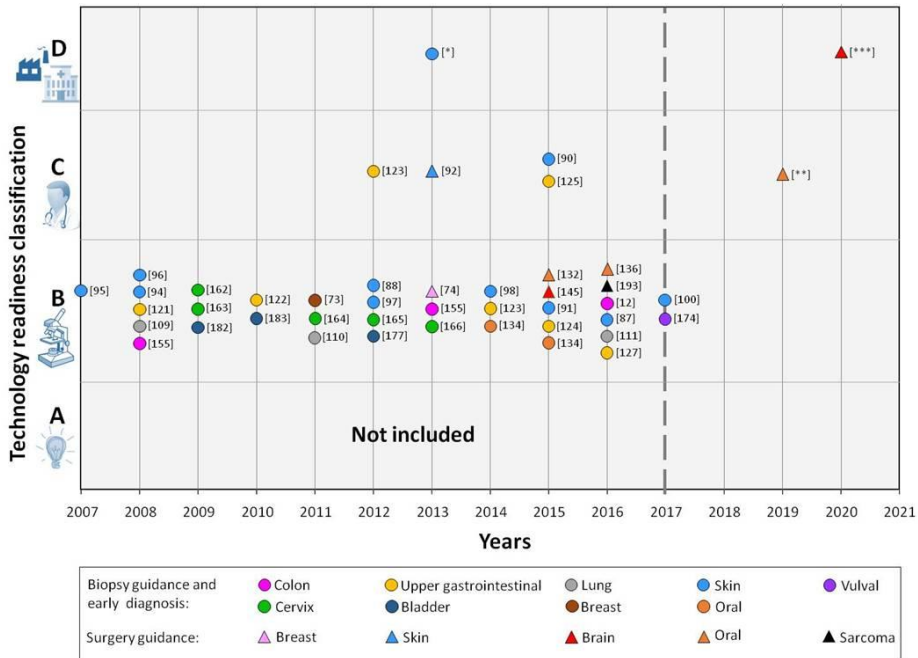


**Figure 6. Illustration of the result from the technology readiness classification of the different Raman studies, mentioned in the Raman applications section. Verisante Technology Inc. is commercializing a device (Verisante Aura) for skin cancer detection [\*]. In the graph is also plotted the prognosis (2017-2021) of further development/commercialization given by the companies RiverD International B.V. [\*\*] and ODS Medical Inc. [\*\*\*].**

*Hurdles in translation reported by companies:* Some of the companies have indicated what hurdles they have encountered when translating Raman systems into the clinics. One important issue can be assuring that high-quality data can be acquired consistently and robustly under intra-operative conditions, with minimal disruption of the surgical workflow (210). It is also important to ensure that real-time high-accuracy tissue classification is provided to surgeons in an intuitive way and by simple metrics (user-friendliness).

Another referred problem is to find funding/investors that can help to bring the product into the market. The fact that Raman spectroscopy is still a relatively unknown technique for most clinicians, was yet another hurdle mentioned. This can be partially explained by the fact that from all the scientific studies reviewed in this article only approximately 30% were published in medical oriented journals. Another explanation for Raman spectroscopy to be relatively unknown might be also partly due to this technique not being widely incorporated in the curriculum of

clinicians or clinical researchers. To resolve this, more effort should be done towards publication of clinical Raman studies in medical oriented journals. Additionally, current academic leaders in the medical field, who have knowledge of clinical spectroscopy, should encourage the introduction of this subject in medical school curriculums alongside other medical imaging and diagnostic topics.



**Figure 7 - Verisante Aura system for skin detection. Courtesy of Verisante Technology, Inc. ([http://www.verisante.com/aura/medical\\_professional/](http://www.verisante.com/aura/medical_professional/))**

## Discussion

In the last decade a strong effort has been made towards clinical implementation of Raman spectroscopy as an adjunct technique for early diagnosis, biopsy guidance and oncologic surgery guidance. The most recent studies aim to: 1) detect pre-malignant lesions (113,125,126,136,164,222), 2) detect cancer in less advanced stages (101,113,125,157,158), 3) reduce the number of unnecessary biopsies (91,96,112,113), and 4) guide surgery towards complete removal of the tumor (76,94,138,148,206). This means that Raman spectroscopy is used to detect (pre-)malignant lesions for guidance of clinical procedures. A next step would be to use Raman spectroscopy in diagnosis of (pre-)malignant lesions; i.e. differentiating between different types of cancer and grading (pre-)malignant lesions (e.g., differentiating high-grade from low-grade dysplasia) (12,111,126,127,136). Raman spectroscopy may address all the clinical needs mentioned, because, in fact, all show the same fundamental problem: lack of pre- and intra-operative methods with sufficient or clinically relevant sensitivity and specificity. Raman spectroscopy is an objective technique that can add biochemical information, can be performed in-vivo and can be used in real-time. Raman spectroscopy can help pathologists and surgeons to assure adequate resection margins intra-operatively (2,20,21,82,148).

Consequently, the use of this technique may help to improve the surgical outcome of the patients and to decrease the need for adjuvant therapy. Raman spectroscopy can also give an objective and reliable decision about malignancy and early malignant stages (2,20,21,82,223). This technique could help medical professionals in assessing with a clinically relevant specificity and sensitivity the location for most representative biopsies (2,21,223). In-vivo and ex-vivo trials that aim for detection of malignant tissue have achieved sensitivities varying between 77% and 100% and specificities varying between 45% and 100%. Studies that aimed for detection of pre-malignant lesions presented specificities (ranging between 63% and 97.8%) and sensitivities (ranging between 70% and 93.5%). Although these numbers are not perfect they demonstrate that Raman spectroscopy can help to improve current clinical practice. In the past, a disadvantage of Raman spectroscopy was the low measurement speed. One way to overcome this is to complement Raman spectroscopy with other techniques, such as auto-fluorescence imaging. For instance, Kong et al. and McGregor *et al.*, (94,113,224) have used auto-fluorescence imaging to quickly scan large areas of tissue for selection of the measurement locations for Raman spectroscopy, thereby reducing the time spent on redundant or non-relevant Raman measurements (94,202). Although spontaneous Raman spectroscopy is a mature technology there is still considerable development in instrumentation that further enable development towards clinical applications, in particular 1) advances in the detector technology, 2) in-vivo miniature fiber-optic probes to be used as an adjunct device to conventional endoscopes for biopsy targeting or for surgery guidance, 3) combined fluorescence microscopy and Raman spectroscopy systems for guided surgery, and 4) new lasers for low-cost Raman devices. The number of scientific groups that are working towards implementation of Raman spectroscopy devices in clinical procedures is remarkable. Most of the studies (89%) still take place at the same technology readiness level (TRL-4, or class B). In these studies, algorithms have been developed for detection of (pre-) malignant tissue based on in-vivo or ex-vivo measurements, under conditions that approach the intended clinical environment. Validation of these algorithms based on large independent datasets obtained in the actual clinical workflow still needs to happen. We have observed that approximately 30% of the reviewed studies were published in medical journals. In order to raise awareness and increase acceptance of Raman technologies among clinicians and clinical researchers results of Raman cancer diagnostic studies should be presented at medical conferences and published in medical journals. Better communication between clinicians and spectroscopists will facilitate understanding of the clinical requirements and challenges. The gap between technology developers and clinicians is narrowing due to the contribution of multidisciplinary networks like ClirSpec, Raman4Clinics (EU COST Action BM1401) and EPIC. These networks also actively pursue standardization of sample preparation, measurements, data

analysis protocols, which will help to form a basis for transferability and thereby accelerate the developments discussed in this review. These networks can also play an important role in presenting Raman spectroscopy as a technology that can complement and facilitate the work of the clinicians and improve patient outcome. In summary, based on the expectation given by the companies, we believe that within 5 years Raman-based oncological products will advance into routine clinical settings.

## References

1. World Health Organization, GLOBOCAN 2012: Estimated Cancer Incidence, Mortality and Prevalence Worldwide in 2012, <http://globocan.iarc.fr>, (accessed 22 March 2017).
2. Çulha M., *Bioanalysis*, 2015; 7, 2813–2824.
3. Mendoza P., Lacambra M., Tan P.-H., *Patholog. Res. Int.* 2011; 2011, 1–8.
4. Quail D. and Joyce J., *Nat. Med.* 2013; 19, 1423–1437.
5. Menakuru S. R., Brown N. J., Staton C. A., *Br. J. Cancer*. 2008; 99, 1961–1966.
6. Bokhorst L. P., Zhu X., Bul M., *BJU Int.* 2012; 110, 1654–1660.
7. Rominger M., Wisgickl C. and Timmesfeld N., *RoFo*. 2012; 184, 1144–1152.
8. McWilliams A., Tammemagi M. C., Mayo J. R., *N. Engl. J. Med.* 2013; 369, 910–9.
9. Carli P., Mannone F., De Giorgi V., *Melanoma Res*, 2003; 2, 179–182.
10. Kuo W.-C., Kim J., Shemonski N. D., *Biomed. Opt. Express*. 2012; 3, 1149–61.
11. Hariri L. P., Mino-Kenudson M., Applegate M. B., *Chest*. 2013; 144, 1261–1268.
12. Bergholt M. S., Lin K., Wang J., *J. Biophotonics*. 2016; 9, 333–342.
13. Shin D., Vigneswaran N., Gillenwater A., *Future Oncol.* 2010; 6, 1143–54.
14. Wong Kee Song L. M., Banerjee S., Desilets D., *Gastrointest. Endosc.* 2011; 73, 647–650.
15. Wang Y., Wang Q., Feng J., *Patient Prefer. Adherence*. 2013; 7, 621–631.
16. Nijssen A., Koljenović S., Bakker Schut T. C., *J. Biophotonics*. 2009; 2, 29–36.
17. Broadbent B., Tseng J., Kast R., *J. Neurooncol.* 2016, 130; 1–9.
18. Wang W., Zhao J., Short M., *J. Biophotonics*. 2015; 8, 527–545.
19. Li X., Wang Y., Zhang X., *Conf. Proc. IEEE Eng. Med. Biol. Soc.* 2005; 2, 1453–6.
20. Kallaway C., Almond L. M., Barr H., *Photodiagnosis Photodyn. Ther.* 2013; 10, 207–219.
21. McGregor H., Wang W., Short M., *Adv. Heal. Care Technol.* 2016; 2, 13.
22. Binahmed A., Nason R. W. and Abdoh A. A., *Oral Oncol.* 2007; 43, 780–784.
23. Smits R. W. H., Koljenović S., Hardillo J. A., *Head Neck*. 2016; 38, E2197–E2203.

24. Dillon J. K., Brown C. B., McDonald T. M., *J. Oral Maxillofac. Surg.*. 2015; 73, 1182–1188.
25. Neuzillet Y., Soulie M., Larre S., *BJU Int.*. 2013; 111, 1253–1260.
26. Gokavarapu S., Rao L. M. C., Mahajan M., *Br. J. Oral Maxillofac. Surg.*. 2015; 53, 875–879.
27. Williams M. D.. *Curr. Oncol. Rep.*. 2016; 18, 54.
28. Miedema J. R. and Hunt H. V. *J. Gastrointestin. Liver Dis.*. 2010; 19, 181–5.
29. Olson T. P., Harter J., Muñoz A., *Ann. Surg. Oncol.*. 2007; 14, 2953–2960.
30. Emmadi R. and Wiley E. L.. *Int. J. Surg. Oncol.*. 2012; 2012, 1–9.
31. Trejo Bittar H. E., Incharoen P., Althouse A. D., *Mod. Pathol.*. 2015; 28, 1058–63.
32. Rosenthal E. L., Warram J. M., Bland K. I., *Ann. Surg.*. 2015; 261, 46–55.
33. Varvares M. A., Poti S., Kenyon B., *Laryngoscope.* 2015; 125, 2298–2307.
34. Magee N. D., Beattie J. R., Carland C., *J. Biomed. Opt.*. 2010; 15, 026015(1-8).
35. McIntosh E. R., Harada S., Drwiega J., *Ann. Diagn. Pathol.*. 2015; 19, 326–329.
36. Senft C., Bink A., Franz K., *Lancet Oncol.*. 2011; 12, 997–1003.
37. Senft C., Schoenes B., Gasser T., *J. Neurosurg. Anesthesiol.*. 2011; 23, 241–6.
38. Wong J. M., Panchmatia J. R., Ziewacz J. E., *Neurosurg. Focus.* 2012; 33, E16.
39. Wu J.-S., Mao Y., Zhou L.-F., *Neurosurgery.* 2007; 61, 935–949.
40. Claus E. B., Horlacher A., Hsu L., *Cancer.* 2005; 103, 1227–1233.
41. Kuhnt D., Becker A., Ganslandt O., *Neuro. Oncol.*. 2011; 13, 1339–1348.
42. Kubben P. L., ter Meulen K. J., Schijns O. E. M. G., *Lancet Oncol.*. 2011; 12, 1062–1070.
43. Visgauss J. D., Eward W. C. and Brigman B. E.. *Orthop. Clin. North Am.*. 2016; 47, 253–264.
44. Prada F., Perin A., Martegani A., *Neurosurgery.* 2014; 74, 542–552.
45. Selbekk T., Jakola A. S., Solheim O., *Acta Neurochir. (Wien)*. 2013; 155, 973–980.
46. Erickson-Bhatt S. J., Nolan R. M., Shemonski N. D., *Cancer Res.*. 2015; 75, 3706–3712.
47. Stummer W., Pichlmeier U., Meinel T., *Lancet Oncol.*. 2006; 7, 392–401.
48. Widhalm G., Kiesel B., Woehrer A., *PLoS One*, DOI:10.1371/journal.pone.0076988.
49. Stummer W., Tonn J.-C., Mehdorn H. M., *J. Neurosurg.*. 2011; 114, 613–623.

50. Roberts D. W., Valdés P. A., Harris B. T., *J. Neurosurg.* 2011; 114, 595–603.
51. Agdeppa E. D. and Spilker M. E., *AAPS J.* 2009; 11, 286–299.
52. Jermyn M., Mok K., Mercier J., *Sci. Transl. Med.* 2015; 7, 274ra19–274ra19.
53. Haka A. S., Volynskaya Z., Gardecki J., *J. Biomed. Opt.* 2009; 14, 54023.
54. Kourkoumelis N., Balatsoukas I., Moulia V., *Int. J. Mol. Sci.* 2015; 16, 14554–14570.
55. Austin L. A., Osseiran S. and Evans C. L., *Analyst.* 2016; 141, 476–503.
56. Pence I. and Mahadevan-Jansen A., *Chem. Soc. Rev.* 2016; 45, 1958–1979.
57. Shipp D. W., Sinjab F. and Notingher I., *Adv. Opt. Photon.* 2017; 9, 315–428.
58. Krafft C., Schie I. W., Meyer T., *Chem. Soc. Rev.* 2016; 45, 1819–1849.
59. Camp Jr C. H. and Cicerone M. T., *Nat. Photonics.* 2015; 9, 295–305.
60. Kerr L. T., Lynn T. M., Cullen I. M., *Anal. Methods.* 2016; 8, 4991–5000.
61. Isabelle M., Stone N., Barr H., *Spectr.* 2008; 22, 97–104.
62. European Commission, *Horizon 2020; Work programme. 2014-2015, 2014.*
63. Johnson J. M., Dalton R. R., Wester S. M., *Arch Surg.* 1999; 134, 712–716.
64. Wang M., He X., Chang Y., *The Breast.* 2017; 31, 157–166.
65. Sun W., Li A., Abreo F., *Diagn. Cytopathol.* 2001; 24, 421–5.
66. Lieske B., Ravichandran D. and Wright D., *Br. J. Cancer.* 2006; 95, 62–66.
67. Yu Y.-H., Wei W., Liu J.-L., *BMC Cancer.* 2012; 12, 41.
68. Kazi M., Suhani, Parshad R., *World J. Surg.* 2017; 41, 1528–1533.
69. van Maaren M. C., de Munck L., Jobsen J. J., *Breast Cancer Res. Treat.* 2016; 160, 511–521.
70. Onitilo A. A., Engel J. M., Stankowski R. V., *Clin. Med. Res.* 2015; 13, 65–73.
71. Agarwal S., Pappas L., Neumayer L., *JAMA Surg.* 2014; 149, 267.
72. Ellis I. O., Carder P., Hales S., *Pathology reporting of breast disease in surgical excision specimens incorporating the dataset for histological reporting of breast cancer.* 2016.
73. Vos E. L., Siesling S., Baaijens M. H. A., *Breast Cancer Res. Treat.*, DOI:10.1007/s10549-017-4232-6.
74. Jacobs L., *Ann. Surg. Oncol.* 2008; 15, 1271–1272.
75. Saha A., Barman I., Dingari N. C., *Biomed. Opt. Express.* 2011; 2, 2792.

76. Barman I., Dingari N. C., Saha A., *Cancer Res.* 2013; 73, 3206–3215.
77. Lomas A., Leonardi-Bee J. and Bath-Hextall F., *Br. J. Dermatol.* 2012; 166, 1069–1080.
78. Lewis K. G. and Weinstock M. A., *Arch Dermatol.* 2004; 140, 837–842.
79. Drakaki E., Vergou T., Dessinioti C., *J. Biomed. Opt.* 2013; 18, 61221.
80. Basaalcarcinoom-Klinische marges BCC,  
[https://richtlijndatabase.nl/richtlijn/basaalcelcarcinoom/conventionele\\_chirurgische\\_excisie\\_bcc/klinische\\_marges\\_bcc.html](https://richtlijndatabase.nl/richtlijn/basaalcelcarcinoom/conventionele_chirurgische_excisie_bcc/klinische_marges_bcc.html), (accessed 25 April 2017).
81. van Loo E., Mosterd K., Krekels G. A. M., *Eur. J. Cancer.* 2014; 50, 3011–3020.
82. Jermyn M., Desroches J., Aubertin K., *Phys. Med. Biol.* 2016; 61, R370–R400.
83. Siegel R., Ma J., Zou Z., *CA. Cancer J. Clin.* 2014; 64, 9–29.
84. Balch C. M., Gershenwald J. E., Soong S. J., *J. Clin. Oncol.* 2009; 27, 6199–6206.
85. Dickson P. V. and Gershenwald J. E., *Surg. Oncol. Clin. N. Am.* 2011; 20, 1–17.
86. Kittler H., Pehamberger H., Wolff K., *Lancet Oncol.* 2002; 3, 159–65.
87. Morton C. A. and Mackie R. M., *Br. J. Dermatol.* 1998; 138, 283–7.
88. van der Rhee J. I., Bergman W. and Kukutsch N., *Acta Derm. Venereol.* 2011; 91, 428–31.
89. Santos I. P., Caspers P. J., Bakker Schut T. C., *Anal. Chem.* 2016; 88, 7683–7688.
90. Lui H., Zhao J., McLean D., *Cancer Res.* 2012; 72, 2491–2500.
91. Lieber C., Majumder S. K., Billheimer D., *J. Biomed. Opt.* 2008; 13, 24013.
92. Zhao J., Lui H., Kalia S., *Anal. Bioanal. Chem.* 2015; 407, 8373–8379.
93. Schleusener J., Gluszczynska P., Reble C., *Exp. Dermatol.* 2015; 24, 767–772.
94. Kong K., Rowlands C. J., Varma S., *Proc. Natl. Acad. Sci. U. S. A.* 2013; 110, 15189–94.
95. Eberhardt K., Stiebing C., Matthäus C., *Expert Rev. Mol. Diagn.* 2015; 15, 773–87.
96. Zhao J., Lui H., McLean D. I., *Conf. Proc. IEEE Eng. Med. Biol. Soc.* 2008; 2008, 3107–3109.
97. Lieber C. and Mahadevan-Jansen A., *Opt. Express.* 2007; 15, 11874–11882.
98. Lieber C. A., Majumder S. K., Ellis D. L., *Lasers Surg Med.* 2008; 40, 461–467.
99. Silveira L., Silveira F. L., Bodanese B., *Proc. SPIE.* 2012; 8207, 82070X–1–7.
100. Lim L., Nichols B., Migden M. R., *J.*

- Biomed. Opt.*. 2014; 19, 117003.
101. Santos I. P., Caspers P. J., Bakker Schut T., *J. Raman Spectrosc.*. 2015; 652–660.
  102. Bratchenko I. A., Artemyev D. N., Myakinin O. O., *J. Biomed. Opt.*. 2017; 22, 27005.
  103. Sun J., Garfield D. H., Lam B., *J Thorac Oncol.*. 2011; 6, 1336–1344.
  104. Jain P., Hadique S. and Mehta A. C.. *Interventional Bronchoscopy*, Humana Press, Totowa, NJ, 2013; vol. 100, pp. 15–44.
  105. Idowu M. O. and Powers C. N.. *Int. J. Clin. Exp. Pathol.*. 2010; 3, 367–385.
  106. Ginsberg R. J. and Rubinstein L. V.. *Ann. Thorac. Surg.*. 1995; 60, 615–623.
  107. Landreneau R. J., Sugarbaker D. J., Mack M. J., *J. Thorac. Cardiovasc. Surg.*. 1997; 113, 691–700.
  108. Blasberg J. D., Pass H. I. and Donington J. S., *J Thorac Oncol.*. 2010; 5, 1583–1593.
  109. Liu S., Wang R., Zhang Y., *J. Clin. Oncol.*. 2016; 34, 307–313.
  110. Yeh Y.-C., Nitadori J., Kadota K., *Histopathology*. 2015; 66, 922–938.
  111. Short M. A., Lam S., McWilliams A., *Opt. Lett.*. 2008; 33, 711–3.
  112. Short M. A., Lam S., McWilliams A. M., *J. Thorac. Oncol.*. 2011; 6, 1206–1214.
  113. McGregor H. C., Short M. A., McWilliams A., *J. Biophotonics*. 2016; 13, n/a-n/a.
  114. Ferlay J., Soerjomataram I., Dikshit R., *Int. J. Cancer*. 2015; 136, E359–E386.
  115. Rees J., Lao-Sirieix P., Wong A., *Cochrane Database Syst. Rev.*. 2011; 2010–2012.
  116. Lal N., Bhasin D. K., Malik K., *Gut*. 1992; 33, 724–6.
  117. Choi Y., Choi H. S., Jeon W. K., *J. Korean Med. Sci.*. 2012; 27, 36–39.
  118. Menon S. and Trudgill N., *Endosc. Int. Open*. 2014; 2, E46–E50.
  119. Tsutsui S., Kuwano H., Watanabe M., *Ann. Surg.*. 1995; 222, 193–202.
  120. Casson A. G., Darnton S. J., Subramanian S., *Ann. Thorac. Surg.*. 2000; 69, 205–209.
  121. Sagar P. M., Johnston D., McMahon M. J., *Br. J. Surg.*. 1993; 80, 1386–1388.
  122. Dexter S. P., Sue-Ling H., McMahon M. J., *Gut*. 2001; 48, 667–670.
  123. Teh S. K., Zheng W., Ho K. Y., *Br. J. Cancer*. 2008; 98, 457–65.
  124. Bergholt M. S., Zheng W., Lin K., *Analyst*. 2010; 135, 3162–3168.
  125. Duraipandian S., Bergholt M. S., Zheng W., *J. Biomed. Opt.*. 2012; 17, 81418.
  126. Bergholt M. S., Zheng W., Ho K. Y., *Proc. SPIE*. 2014; 8939, 89390M.

127. Lin K., Wang J., Sylvest Bergholt M., *Proc. of SPIE*, eds. M. J. Suter, S. Lam, M. Brenner, G. J. Tearney and T. D. Wang, Nature Publishing Group, 2015; vol. 9304, p. 93040V.
128. Ishigaki M., Maeda Y., Taketani A., *Analyst*. 2015; 141, 1027–33.
129. Wang J., Lin K., Zheng W., *Sci. Rep.*. 2015; 5, 12957.
130. Slootweg P. J., Hordijk G. J., Schade Y., *Oral Oncol.*. 2002; 38, 500–503.
131. Al-Rajhi N., Khafaga Y., El-Husseiny J., *Oral Oncol.*. 2000; 36, 508–514.
132. Helliwell T. and Woolgar J.. *Dataset for histopathology reporting of mucosal malignancies of the nasal cavities and paranasal sinuses*. 2013.
133. Helliwell T. and Woolgar J.. *Dataset for histopathology reporting of mucosal malignancies of the larynx*. 2013.
134. Hoffmannová J., Foltán R., Vlk M., *Int. J. Oral Maxillofac. Surg.*. 2010; 39, 561–567.
135. Barroso E. M., Smits R. W. H., Schut T. C. B., *Anal. Chem.*. 2015; 87, 2419–2426.
136. Krishna H., Majumder S. K., Chaturvedi P., *J. Biophotonics*. 2014; 7, 690–702.
137. Guze K., Pawluk H. C., Short M., *Head Neck*. 2015; 37, 511–517.
138. Barroso E. M., Smits R. W. H., Van Lanschot C. G. F., *Cancer Res.*. 2016; 76, 5945–5953.
139. Wong E. T. and Wu J. K.. Clinical presentation and diagnosis of brain tumors, [https://www.uptodate.com/contents/clinical-presentation-and-diagnosis-of-brain-tumors?source=search\\_result&search=brain-cancer&selectedTitle=1~150#H22](https://www.uptodate.com/contents/clinical-presentation-and-diagnosis-of-brain-tumors?source=search_result&search=brain-cancer&selectedTitle=1~150#H22), (accessed 12 May 2017).
140. Hollon T., Lewis S., Freudiger C. W., *Neurosurg. Focus*, 2016; 40, E9.
141. Koljenović S., Choo-Smith L.-P., Bakker Schut T. C., *Lab. Investig.*. 2002; 82, 1265–1277.
142. Marko N. F., Weil R. J., Schroeder J. L., *J. Clin. Oncol.*. 2014; 32, 774–782.
143. Sanai N., Chang S. and Berger M., *J Neurosurg*. 2011; 115, 945–947.
144. Lu F. K., Calligaris D., Olubiyi O. I., *Cancer Res.*. 2016; 76, 3451–3462.
145. Albert F., Forsting M., Sartor K., *Neurosurgery*. 1994; 34, 45–61.
146. Ulmer S., *World J. Radiol.*. 2014; 6, 538–43.
147. Ji M., Lewis S., Camelo-Piragua S., *Sci. Transl. Med.*. 2015; 7, 309ra163-309ra163.
148. Jermyn M., Mok K., Mercier J., *Science Translational Medicine*, eds. R. R. Alfano and S. G. Demos, 2015; vol. 7, p. 93180D.
149. Wallace M. B. and Keisslich R., *Gastroenterology*. 2010; 138, 2140–2150.

150. Bressler B., Paszat L. F., Chen Z., *Gastroenterology*. 2007; 132, 96–102.
151. Quintero E., Hassan C., Senore C., *Gastroenterol. Res. Pract.*. DOI:10.1155/2012/846985.
152. Stallmach A., Schmidt C., Watson A., *J. Biophotonics*. 2011; 4, 482–489.
153. Kessler W. R., Imperiale T. F., Klein R. W., *Endoscopy*. 2011; 43, 683–691.
154. Nelson H., Petrelli N., Carlin A., *J Natl Cancer Inst*. 2001; 93, 591.
155. Amri R., Bordeianou L. G., Sylla P., *JAMA Surg.* 2015; 150, 890–8.
156. O'Connell J. B., Maggard M. and Ko C. Y., *J. Natl. Cancer Inst.* 2004; 96, 1420–1425.
157. Widjaja E., Zheng W. and Huang Z., *Int. J. Oncol.* 2008; 32, 653–662.
158. Short M. A., Tai I. T., Owen D., *Opt. Express*. 2013; 21, 5025–34.
159. Peirson L., Fitzpatrick-Lewis D., Ciliska D., *Syst. Rev.*, 2013; 2, 35.
160. Nanda K., Mccrory D. C., Myers E. R., *Ann Intern Med.* 2000; 132, 810–819.
161. Cuzick J., Clavel C., Petry K.-U., *Int. J. Cancer*. 2006; 119, 1095–1101.
162. Mustafa R. A., Santesso N., Khatib R., *Int. J. Gynecol. Obstet.* 2016; 132, 259–265.
163. Eftekhari Z., Rahimi-Moghaddam P., Yarandi F., *Asian Pac. J. Cancer Prev.* 2005; 6, 69–71.
164. Mo J., Zheng W., Low J. J. H., *Anal. Chem.* 2009; 81, 8908–15.
165. Kanter E. M., Vargis E., Majumder S., *J. Biophotonics*. 2009; 2, 81–90.
166. Duraipandian S., Zheng W., Ng J., *Analyst*. 2011; 136, 4328.
167. Duraipandian S., Zheng W., Ng J., *Anal. Chem.* 2012; 84, 5913–5919.
168. Ramos I. R. M., Malkin A. and Lyng F. M., *Biomed Res. Int.* 2015; 2015, 1–9.
169. Rubina S., Amita M., Kedar K. D., *Vib. Spectrosc.* 2013; 68, 115–121.
170. Vulval cancer mortality statistics, (accessed 4 April 2017), <http://www.cancerresearchuk.org/health-professional/cancer-statistics/statistics-by-cancer-type/vulval-cancer/mortality#heading-Zero>.
171. Wessels R., de Bruin D. M., Faber D. J., *J. Biomed. Opt.* 2012; 17, 116022.
172. Dellinger T. H., Hakim A. A., Lee S. J., 1999; 15, 1–5.
173. Heaps J. M., Fu Y. S., Montz F. J., *Gynecol. Oncol.* 1990; 38, 309–314.
174. Chan J. K., Sugiyama V., Pham H., *Gynecol. Oncol.*; 2007, 104, 636–641.
175. Wessels R., van Beurden M., de Bruin D. M., *Int. J. Gynecol. Cancer*. 2015; 25, 112–118.
176. Frost J., Ludeman L., Hillaby K.,

- Analyst*. 2017; 142, 1200–1206.
177. Minamikawa T., Harada Y. and Takamatsu T., *Sci. Rep.*. 2015; 5, 17165.
178. Clark P. E., Agarwal N., Biagioli M. C., *J. Natl. Compr. Cancer Netw.*. 2013; 11, 446–75.
179. Barman I., Dingari N. C., Singh G. P., *Anal. Bioanal. Chem.*. 2012; 404, 3091–3099.
180. Jocham D., Stepp H. and Waidelich R., *Eur. Urol.*. 2008; 53, 1138–1150.
181. Seltz L. M. and Herrell S. D., *Curr. Opin. Urol.*. 2016; 26, 259–263.
182. Dotan Z. A., Kavanagh K., Yossepowitch O., *J. Urol.*. 2007; 178, 2308–2313.
183. Novara G., Svatek R. S., Karakiewicz P. I., *Urol.*. 2010; 183, 2165–2170.
184. Grimbergen M. C. M., van Swol C. F. P., Draga R. O. P., 2009; vol. 7161, p. 716114.
185. Draga R. O. P., Grimbergen M. C. M., Vijverberg P. L. M., *Anal. Chem.*. 2010; 82, 5993–5999.
186. Ruijter E., Van De Kaa C., Miller G., *Endocr. Rev.*. 1999; 20, 22–45.
187. Eichler K., Hempel S., Wilby J., *J. Urol.*. 2006; 175, 1605–1612.
188. Mottet N., Bellmunt J., Bolla M., *Eur. Urol.*. 2016; 71, 1–12.
189. Schlomm T., Tennstedt P., Huxhold C., *Eur. Urol.*. 2012; 62, 333–340.
190. Li M., Banerjee S. R., Zheng C., *Chem. Sci.*. 2016; 7, 6779–6785.
191. Kast R. E., Tucker S. C., Killian K., *Cancer Metastasis Rev.*. 2014; 33, 673–693.
192. Patil C. A., Pence I. J., Lieber C. A., *Opt. Lett.*. 2014; 39, 303–306.
193. Pence I. J., Patil C. A., Lieber C. A., *Biomed. Opt. Express*. 2015; 6, 2724–37.
194. Duraipandian S., Zheng W., Ng J., *J. Biomed. Opt.*. 2013; 18, 67007.
195. Desroches J., Jermyn M., Mok K., *Biomed. Opt. Express*. 2015; 6, 2380–97.
196. Stevens O., Iping Petterson I. E., Day J. C. C., *Chem. Soc. Rev.*. 2016; 45, 1919–1934.
197. Wang J., Bergholt M. S., Zheng W., *Opt. Lett.*. 2013; 38, 2321–3.
198. Wang J., Lin K., Zheng W., *Anal. Bioanal. Chem.*. 2015; 407, 8303–8310.
199. Duraipandian S., Bergholt M. S., Zheng W., *J. Biomed. Opt.*. 2012; 17, 81418.
200. Agenant M., Grimbergen M., Draga R., *Biomed. Opt. Express*. 2014; 5, 1203–16.
201. Puppels G. J., *Cancer Res.*. 2017; 77, 2775–2778.
202. Takamori S., Kong K., Varma S., *Biomed. Opt. Express*. 2015; 6, 98.
203. Santos I. P., van der Lee A., Gu X.,

- J. Raman Spectrosc.*  
DOI:10.1002/jrs.5124.
204. Kuznetsov M. in *Semiconductor Disk Lasers. Physics and Technology*, ed. O. G. Okhotnikov, WILEY-VCH, Weinheim, 2010.
205. Pallmann W. P., Zaugg C. A., Mangold M., *Opt. Express.* 2012; 20, 24791.
206. Nguyen J. Q., Gowani Z. S., O'Connor M., *Lasers Surg. Med.* 2016; 48, 774–781.
207. Orringer D. A., Pandian B., Niknafs Y. S., *Nat. Biomed. Eng.* 2017; 1, 27.
208. St-Arnaud K., Aubertin K., Strupler M., *Opt. Lett.* 2016; 41, 4692–4695.
209. Jermyn M., Desroches J., Mercier J., *Biomed. Opt. Express.* 2016; 7, 247–248.
210. Desroches J., Laurence A., Jermyn M., *Analyst.* 2017; 142, 1185–1191.
211. Jermyn M., Desroches J., Mercier J., *J. Biomed. Opt.* 2016; 21, 94002.
212. Isabelle M., Dorney J., Lewis A., *Faraday Discuss.* 2016; 187, 87–103.
213. Gaifulina R., Maher A. T., Kendall C., *Int. J. Exp. Pathol.* 2016; 97, 337–350.
214. Lau K., Isabelle M., Lloyd G. R., *Biomedical Vibrational Spectroscopy*, eds. A. Mahadevan-Jansen and W. Petrich, 2016; vol. 9704, p. 97040B.
215. Short M. A., Wang W., Tai I. T., *J. Biophotonics.* 2016; 9, 44–48.
216. Zhao J., Lui H., McLean D. I., *Appl. Spectrosc.*, 2007; 61, 1225–32.
217. Zhao J., Lui H., McLean D. I., *Skin Res. Technol.*, 2008; 14, 484–92.
218. Abramczyk H., Brozek-Pluska B., Surmacki J., *Analyst.* 2014; 139, 5547–59.
219. Mavarani L., Petersen D., El-Mashtoly S. F., *Analyst.* 2013; 138, 4035–9.
220. Tolstik T., Marquardt C., Matthäus C., *Analyst.* 2014; 139, 6036–43.
221. Lech G., Słotwiński R., Słodkowski M. I., *World J. Gastroenterol.* 2016; 22, 1745–1755.
222. Wang J., Lin K., Zheng W., *Faraday Discuss.* 2015; 187, 377–392.
223. Devpura S., Barton K. N., Brown S. L., *Med. Phys.* 2014; 41, 50901.
224. Kong K., Zabar F., Rakha E., *Phys. Med. Biol.* 2014; 59, 6141–6152.



## ***CHAPTER 3***

# ***Discrimination between oral cancer and healthy tissue based on water content determined by Raman spectroscopy***

E. M. Barroso<sup>†</sup>, R. W. H. Smits<sup>†</sup>, T. C. Bakker Schut, I. ten Hove, J. A. Hardillo, E. B. Wolvius, R. J. Baatenburg de Jong, S. Koljenović, and G. J. Puppels

<sup>†</sup> These authors contributed equally to this work.

**Analytical Chemistry 2015;87(4):2419-2426**



## Abstract

Tumor-positive resection margins are a major problem in oral cancer surgery. High-wavenumber Raman spectroscopy is a reliable technique to determine the water content of tissues which may contribute to differentiate between tumor and healthy tissue. The aim of this study was to examine the use of Raman spectroscopy to differentiate tumor from surrounding healthy tissue in oral squamous cell carcinoma. From fourteen patients undergoing tongue resection for squamous cell carcinoma, the water content was determined at 170 locations on freshly excised tongue specimens using the Raman-bands of the OH-stretching vibrations ( $3350\text{-}3550\text{cm}^{-1}$ ) and of the CH-stretching vibrations ( $2910\text{-}2965\text{cm}^{-1}$ ). The results were correlated with histopathological assessment of hematoxylin and eosin stained thin tissue sections obtained from the Raman measurement locations. The water content values from squamous cell carcinoma measurements were significantly higher than from surrounding healthy tissue (p-value  $<0.0001$ ). Tumor tissue could be detected with a sensitivity of 99% and a specificity of 92% using a cut-off water content value of 69%. Because the Raman measurements are fast and can be carried out on freshly excised tissue without any tissue preparation, this finding signifies an important step towards the development of an intra-operative tool for tumor resection guidance with the aim of enabling oncological radical surgery and improvement of patient outcome.

## Introduction

The primary goal of oncological surgery is the complete removal of cancerous tissue. However, in practice this goal is often not achieved. A recent retrospective study of oral cavity squamous cell carcinoma (OCSCC) surgery showed tumor-positive resection margins in up to 43% of cases (1). Tumor-positive resection margins are well known to lead to a significantly worse clinical outcome after surgery for oral cancer (2,3). The most notable cause of tumor-positive resection margins is the surgeon's inability to reliably differentiate between tumor and healthy tissue by ocular inspection and by palpation. Intra-operative histopathological assessment of suspicious tissue by means of frozen-section procedures have been shown to be unreliable and time-consuming (4-6). This is due to the fact that only a very small percentage of the resection margins can be investigated by this procedure and that the selection of apparently suspicious tissue still depends on the eyes and hands of the surgeon and/ or the pathologist. Intra-operative tools are needed which enable support to the surgeon in his assessment of the resection margin.

As early as 1971, water content was described as a possible discriminator between tumor and healthy tissue (7). Subsequently, tissue water content has been explored using several techniques, such as magnetic resonance imaging (MRI) (8-15) and terahertz imaging (16). Research on nuclear MRI showed that the main cause of the differences observed between the relaxation times of normal and malignant tissues is the higher water content in the latter (7,9,13-15). MRI is a standard imaging modality for localization of a tumor in the oral cavity and for estimating its relation to surrounding tissues and size prior to surgery. However, intra-operative application of these imaging technologies is unfeasible in oral cancer surgery for practical and financial reasons (17).

Another promising technique is terahertz (THz) imaging, which is used to measure water concentration and water distribution in tissues. For breast cancer, cervical cancer, skin cancer and liver cirrhosis, high absorption coefficients were measured using this technique (16,18). These high absorption coefficients reflect high water content. THz imaging is a surface and/or a sub-dermal technique. For measuring the skin this technique can be used quite easily and without extensive preparation. Unfortunately, this technique is still in its infancy with only a few studies describing small numbers of measurements (19). Future research will determine whether THz imaging merits a place in the competitive world of cancer diagnostics.

García-Flores et al. (2011), using Fourier-Transform (FT) Raman Spectroscopy, demonstrated that cancerous tissue in mammary gland tumors in rats shows a higher signal intensity in the OH-stretching region of water ( $3100\text{-}3500\text{ cm}^{-1}$ ) than normal mammary gland tissue. In that study a  $1064\text{nm}$  laser was used for excitation and signal was detected in the  $2800\text{-}3600\text{ cm}^{-1}$  spectral region (20). Philipsen et al. (2013), using near infrared Fourier Transform (NIR-FT) Raman spectroscopy, showed that the diagnosis of malignant and nonmalignant skin lesions is also possible due to significant differences found in the bands around  $3250\text{cm}^{-1}$  (due to OH-stretching vibrations and N-H stretching vibrations) in combination with other specific proteins (21). Confocal Raman imaging and infra-red (IR) spectroscopy have also indicated that the amount of water in breast cancer is remarkably higher than in non-cancerous tissue (22).

Abramczyk *et al.* (2014) demonstrated that the vibration properties of water at the biological interfaces of human breast tissues, acquired from IR and Raman spectroscopy, are sensitive to the cellular environment of the human tissue. These differences in the vibrational properties allow distinguishing between malignant and normal human breast tissue (23).

Raman spectroscopy is very suitable for rapid quantitative (in-vivo) determination of the water concentration of tissue (24,25). In the current study, we have applied high-wavenumber Raman spectroscopy (HWNRS) to quantify the water concentration in freshly excised tissue immediately after OCSCC surgery. The primary goal of this study was to assess the possibility to distinguish tumor from surrounding (healthy) tissue in fresh resection specimens immediately after the surgical procedure.

## Materials and Methods

### Tissue Samples

Resection material of patients undergoing surgery for squamous cell carcinoma (SCC) of the tongue was examined. Tongue resection specimens from 14 patients were included in this study. The resections were part of the normal therapeutic surgical procedures performed at the Erasmus MC Cancer Institute, University Medical Center Rotterdam. Informed consent was obtained prior to the operation according to the protocol approved by the Medical Ethics Committee (MEC-2013-345) of the Erasmus MC Cancer Institute, University Medical Center Rotterdam. The maximum time allowed for the experimental procedure described below was fixed at 30 minutes, to keep tissue preservation optimal and to avoid interference with the routine histopathological examination of the resection specimen.

Measurement locations were chosen by the surgeon and the pathologist aiming to obtain spectra of both tumor and normal tissue. Every chosen location was digitally noted with a number on a photograph of the specimen (figure 1.3). Immediately after a Raman measurement, each measured position was marked with a colored pin (exactly at the place of laser spot) and with the respective digital number. In this way, it was possible to relocate measurement positions after routine histopathological handling of the resection specimen.

### Raman Instrumentation

Raman measurements were obtained using a confocal Raman microscope (CRM), built in-house.

The instrument was placed in a room adjoining the examination room of the pathology department, enabling Raman measurements without delay.

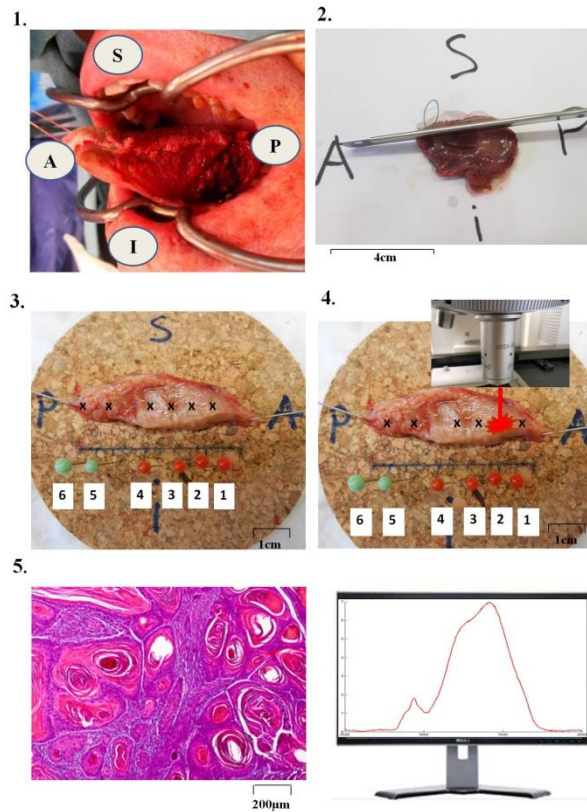


**Figure 1. Overview of specimen handling and measurement protocol. 1. Resection of SCC of the tongue in the surgery room with the orientation shown (anterior (A), posterior (P), superior (S), inferior (I)). 2. Immediately after operation, the resection specimen was transferred to the pathology department in close proximity to the operating room. Here, blood was rinsed from the surface of the tissue using physiological salt solution. Under supervision of the pathologist an incision was made through the tumor and the surrounding healthy tissue. In this way both tumor and normal tongue tissue were made accessible for Raman measurements (see also figure 1.3). 3. Pins were used to fix the tongue specimen to a cork plate. The orientation of the specimen was indicated on the cork plate (Anterior (A), Posterior (P), Superior (S), Inferior (I)). Figures 1.3 and 1.4 also show the demarcation of the locations selected for Raman measurements by means of digital labels; red for locations presumed to be tumor and green for locations presumed to be surrounding normal tongue tissue. 4. Specimen is then transported to the adjoining Raman spectroscopy room. Raman spectra were obtained from the marked locations. 5. After the Raman measurements, the specimen was placed in formalin and processed for routine clinical histopathological evaluation as well as histopathological assessment of each of the locations marked for**

**Raman measurements.** These assessments were used for definitive histopathological annotation of the measured spectra.

The setup consisted of a multichannel Raman Module (HPRM 2500, RiverD International B.V, the Netherlands), equipped with a 671 nm laser (Crystal Laser, CL671-150-SO) and a Charge-Coupled Device (CCD-) camera, fitted with a back-illuminated deep depletion CCD-chip, which was thermo-electrically cooled to -65 °C (Andor iDus 401, DU401A BR-DD, Andor Technology Ltd., UK). The Raman Module was coupled to a microscope (Leica DM RXA2, Leica Microsystems Wetzlar GmbH, Germany) and a computer-controlled sample stage (Leica DM STC). A 20x, 0.4 numerical aperture dry objective with a free working distance of 1.1 mm (N PLAN 11566026, Leica Microsystems B.V, the Netherlands) was used to focus 30-80 mW of laser light to a spot of 4  $\mu\text{m}$  in diameter. Spectral data were collected in the wavenumber interval from 2500  $\text{cm}^{-1}$  to 4000  $\text{cm}^{-1}$  with a resolution  $<5 \text{ cm}^{-1}$ .

### Measurement Protocol

Raman spectra were collected at the selected tissue locations. At each measurement location up to 30 measurements were carried out with a signal collection time of 1 second to assure high signal to noise, until all the selected positions were measured, or the maximum period of 30 minutes available for this study had passed.

After performing the Raman measurements, the specimen was immediately immersed in formalin according to the standard protocols of the pathology department.

### Histological Examination

Histopathological evaluation of the measurement locations (marked with pins) was performed by means of routine hematoxylin and eosin (H&E) stained thin tissue sections (figure 1.5). Each H&E-stained section was photographed and archived.

### Data Analysis

#### *Calibration and preprocessing of spectra:*

After data acquisition, the spectra were calibrated to a relative wavenumber axis and corrected for the wavelength dependent detection efficiency of the setup according to the directions of the spectrometer supplier (RiverD International B.V., the Netherlands). Spectral preprocessing was applied comprising removal of cosmic ray events and subtraction of background signal generated in the optical path of the

setup itself. After pre-processing an average spectrum was calculated for each measurement point.

### *Calculation of water concentration:*

The ratio of the Raman bands at  $3390\text{cm}^{-1}$  and  $2935\text{cm}^{-1}$  was used to determine the concentration of water from the average spectra of each measurement point, according to the method developed by Caspers *et al.* (2001).

The method uses the background corrected bands of protein (P:  $2910\text{-}2966\text{ cm}^{-1}$ ) and water (W:  $3350\text{-}3550\text{ cm}^{-1}$ ), as illustrated in figure 2, to calculate the water concentration using the following equation:

$$\text{water concentration (\%)} = \frac{\frac{W}{P}}{\frac{W}{P} + R} * 100 \quad (3.1)$$

In this equation  $W$  is the integrated Raman signal of water,  $P$  is the integrated Raman signal of protein and  $R$  is proportionality constant describing the ratio between the Raman bands of water and protein in a solution with a water concentration of 50 % (24).

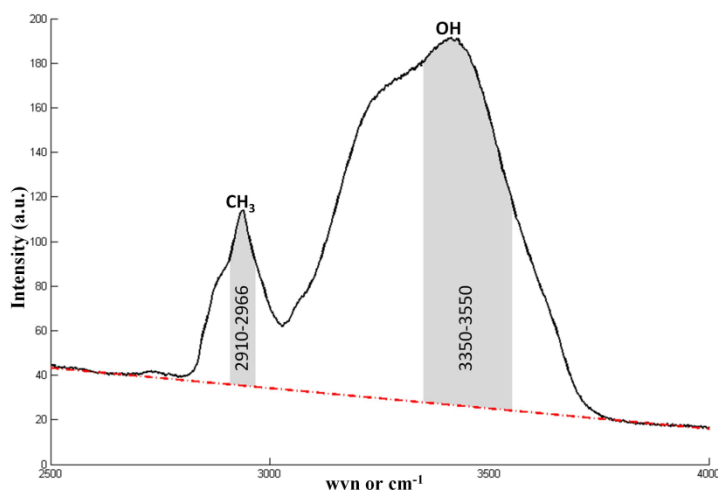


**Figure 2.** Example of a HWNR spectrum used to illustrate the factors  $W$  and  $P$  of equation 1.  $P$  is the Integrated Raman signal intensity of protein, represented by the gray bar located between  $2910$  and  $2966\text{ cm}^{-1}$ .  $W$  is the Integrated Raman signal intensity of water is represented the gray bar, located between  $3350$  and  $3550\text{ cm}^{-1}$ .

Signal background was estimated by a linear fit to the first 20 points (2600-2638  $\text{cm}^{-1}$ ) and the last 20 points (3762-3800  $\text{cm}^{-1}$ ) of the signal. The CH-band intensity (P) and the OH-stretching band intensity (W) were calculated with respect to this linear signal background.

The error in determining the water concentration is mainly caused by the error in estimating the linear background, represented by the red line in figure 2. The error is estimated by calculating the two most extreme possible baselines, one with the highest possible slope, and one with the lowest possible slope. The error in the water calculation is defined as half of the difference between the maximum and minimum water concentration values, calculated using these two extreme baselines (25).

### *Statistical analysis:*

A Mann-Whitney U-test was used to determine if the water content of squamous cell carcinoma and the water content of healthy tissue showed a statistically significant difference.

The power to discriminate between healthy tissue and SCC was determined using a ROC (Receiver Operating Characteristic) curve. The ROC curve was obtained by determining the number of correct and incorrect classifications as a function of the threshold water concentration value to discriminate between the two groups. The Youden Index (highest combined specificity and sensitivity) was used to determine an optimal threshold value for using the water concentration as a diagnostic marker (26).

## **Results and Discussion**

One hundred and seventy Raman point measurements were performed on tongue resection specimens obtained from 14 patients. Each point measurement is represented by the average of acquisitions performed in the respective point.

### **Histology and Spectral Analysis**

Seventy one of the 170 Raman point measurements were labeled SCC and 99 were labeled normal tissue after histopathological assessment of H&E stained tissue sections obtained from the measurement locations. Normal tissue comprised muscle, fat, connective tissue, blood vessels, salivary glands and/or nerve.

After normalization of the intensity of the spectra to the signal in the CH-stretching band ( $2800\text{ cm}^{-1}$  to  $3040\text{ cm}^{-1}$ ), the intensity of the OH-stretching vibration ( $3450\text{ cm}^{-1}$ ) is seen to be higher in spectra of SCC than in spectra of normal tissue, as shown in figure 3. The spectra in figure 3 were normalized with an extended multiplicative signal correction (emsc) to clearly illustrate the differences between normal and SCC measurements (27). This normalization was not used for calculation of the water concentrations, but only to better illustrate the intensity differences for the OH band.

The Raman experiments did not lead to tissue degeneration and did not interfere with routine histopathological evaluation of the resection specimen. The H&E sections performed as routine histopathological work-up showed, for all the measured locations, tissue without degeneration and without any damages.

### **Statistical significance of water concentration to differentiate normal tissue and SCC**

For each spectrum the water concentration was calculated according to equation 3.1. Figure 4a shows a graphical representation of all water concentrations, arranged according to their histopathological annotation. For the majority of cases the water content of SCC was higher than that of normal tissue, as illustrated in figure 4a. The clear separation of data points indicates that the groups are significantly different, which was confirmed by a Mann-Whitney U-test confirming that the water concentration in SCC is significantly higher than in surrounding normal tissue ( $p < 0.0001$ ). This difference is illustrated in figure 5a, where a typical spectrum of SCC is shown together with the respective H&E stained tissue section.

Based on the distribution of the water concentration we identified two groups within the normal tissue, one with very low water concentration (0-30%) and one with moderate water concentration (>30%). The spectrum of the tissue with low water concentration is shown in figure 5b, characterized by a high intensity of the CH symmetric stretch of lipids ( $2724\text{ cm}^{-1}$  and  $2926\text{ cm}^{-1}$ ),  $\text{CH}_2$  symmetric stretch of lipids ( $2860\text{ cm}^{-1}$ ),  $\text{CH}_2$  asymmetric stretch of lipids and proteins ( $2900\text{ cm}^{-1}$ ) and unsaturated  $=\text{CH}$  stretch ( $3010\text{ cm}^{-1}$ ) (28). Histopathological correlation revealed adipose tissue at this measurement location, as shown in figure 5b1.

This holds true in general. Whenever we encountered low water concentration this was in adipose tissue, which therefore is easy to distinguish from SCC (figure 4a). The second group of normal tissue is characterized by CH-stretching vibration typical for proteins, which corresponds to muscle and connective tissue based on

histopathological evaluation, as shown in figure 5c1 (28) and water concentration values higher than 30%. Figure 6c2 shows a representative spectrum of this group.

In order to verify whether adipose tissue was of major influence on the statistical significance of the differences in water concentration between SCC and all normal tissues measured, a new calculation was made after removing the adipose tissue measurements from our dataset. The difference between the water concentration in healthy tissue and SCC remained statistically significant ( $p < 0.0001$ ).

To investigate the use of the water concentration as a diagnostic marker during tumor resection surgery, a ROC curve was generated based on all measurements, where the true positive rate (sensitivity) was plotted against the false positive rate for different values of water concentration threshold (29). This is displayed in figure 4b.

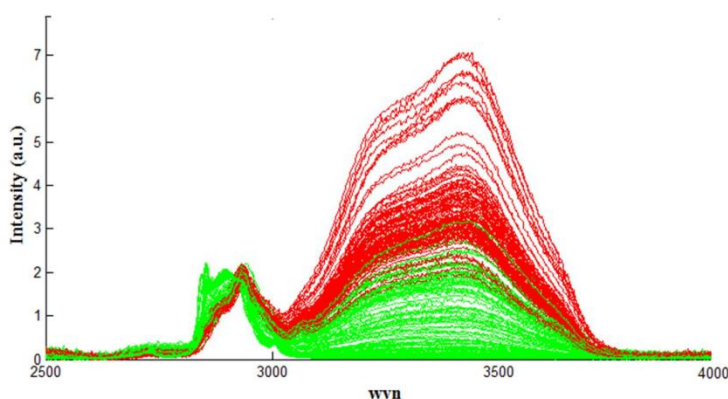


**Figure 3.** All 170 HWNR spectra normalized on the CH-stretching band ( $2800 \text{ cm}^{-1}$  to  $3040 \text{ cm}^{-1}$ ). Spectra are colored according to the histopathological evaluation. The green color represents spectra from healthy tissue and the red color represents spectra from SCC tissue.

The area under the curve proved to be 0.98. This further illustrates the high discriminatory power of water content as a diagnostic marker for SCC detection. The Youden Index was used as the optimum cut-off value, since it represents the best combination of specificity and sensitivity (26). The Youden index is a water concentration of 69%, with a sensitivity of 99% and a specificity of 92%.

The mean error in the estimation of the water concentration for healthy non-adipose tissue and SCC is 0.95%. For a cut-off of  $69 \pm 0.95\%$  the sensitivity stays 99% but the specificity ranges between 86 and 92%. Therefore, errors in determination of the water content will only affect the specificity of the discrimination between healthy tissue and SCC.

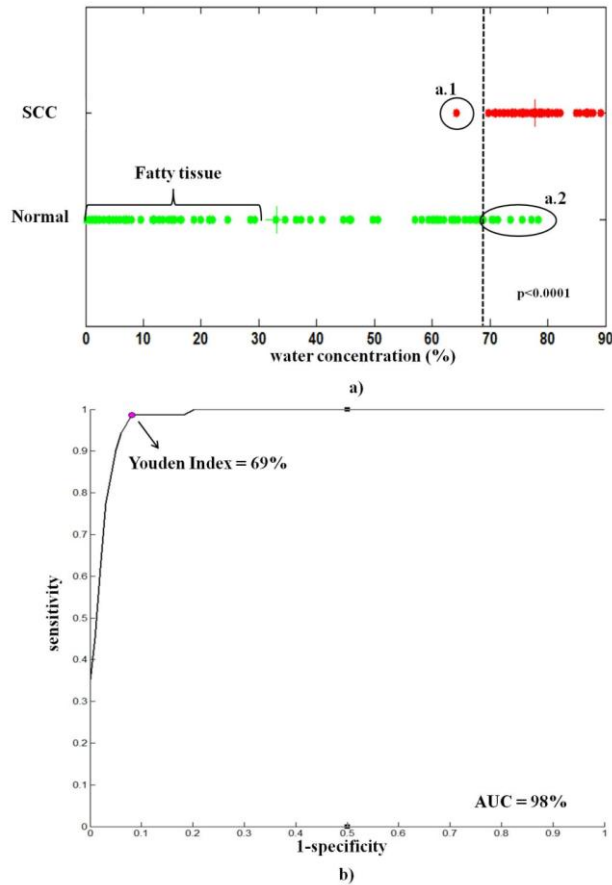


**Figure 4.** Scatter plot of the water concentration for all measurements (a) and the ROC-curve for discriminating SCC from normal tissue (b). (a) - the red points present the water concentration values for measurements in SCC and the green points show the water concentration values measured in healthy tissue. The  $p(<0.0001)$  value was calculated according with the Mann-Whitney u test. The vertical broken line represents the position of the cut off value calculated as Youden Index. (b) - at the Youden Index (water concentration of 69%) the sensitivity is 0.99 and the specificity is 0.92. The calculated area under the curve (AUC), representative for the discriminative power, is 0.98.

In figure 4a the highlighted points labeled a.1 and a.2 represent a measured water concentration in SCC below the cut-off concentration of 69% and a water concentration in healthy tissue above this cut-off value, respectively.

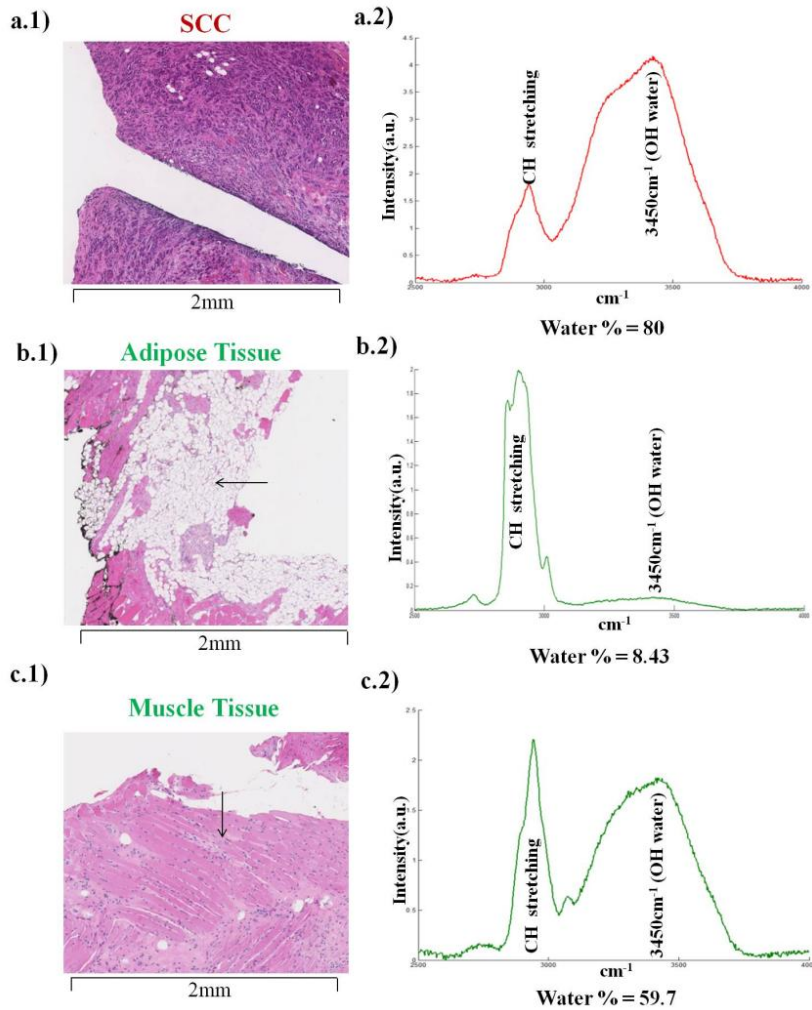


**Figure 5.** Examples of H&E stained thin tissue section of SCC a.2) typical Raman spectrum of SCC. b.1) H&E stained thin tissue section showing adipose tissue (arrow) b.2) Raman spectrum of adipose tissue. c.1) H&E stained thin tissue section showing muscle tissue (arrow) c.2) representative Raman spectrum of muscle.

The SCC-measurement showing a water concentration below the cut-off value of 69% is shown in figure 6. We cannot exclude that normal tissue is also present in the

measured region, however, histopathologically, this H&E stained section was identified as SCC.

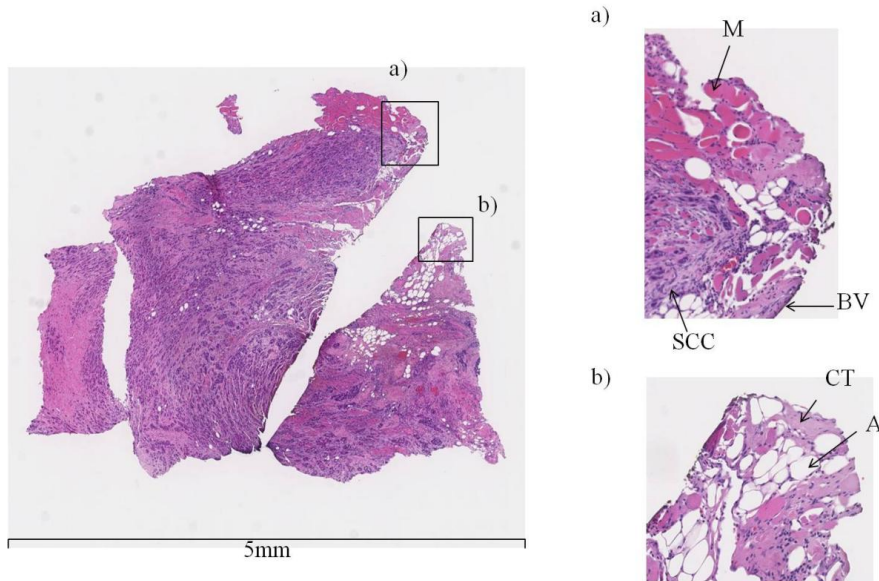


**Figure 6.** H&E stained thin tissue section from the SCC-measurement that has a water concentration below the cut-off value 69%. The area where the measured point is located is represented by a) and b) and histologically this area contains muscle cells (M), a blood vessel (BV), some connective tissue (CT), adipose tissue (A) and tumor cells (SCC).

The eight measurements represented by label a.2 in figure 4a were of tissue locations with a mixture of connective tissue, muscle, blood vessels and nerves, showing water concentrations ranging between 71.4-78.4%. We do not have a clear explanation why the water concentration in these eight measurements is above the 69% cut off value.

The higher water concentration we found in SCC compared to healthy tissue was also found earlier in other tumors, such as melanoma, ductal carcinoma of the breast and basal cell carcinoma. However, these were qualitative observations (20-22).

Garcia-Flores et al. (2011) have reported a higher water concentration in chemically induced breast tumors in rats, than in normal breast tissue. In this case the normal tissue measurements appear to have been obtained from subcutaneous adipose tissue, which contains very little water, different from the tumor which is rich in water (20). Philipsen et al. (2013) demonstrated by in-vivo FT Raman spectroscopy

a relatively stronger Raman signal contribution of water in skin lesions (including melanoma, basal cell carcinoma and benign pigmented lesions) than in normal skin. It should be noted that the spectral region assigned in this paper to water OH-stretching vibrations (3175 to 3265  $\text{cm}^{-1}$ ) strongly overlaps with NH-stretching vibrations from proteins and therefore is not the most suitable spectral region to assess water concentration in tissue (21). Surmacki et al. (2013) also reported a higher intensity of the water Raman signal water in human breast tumor than in normal (adipose) breast tissue, which is low in water content by nature (22).

A first limitation of this study is related with the fact that the method to calculate the water concentration was devised for protein-water mixtures, and does not take the signals from lipids into account which also contribute to the 2910-2966  $\text{cm}^{-1}$  band. The measurements with a high signal from lipids showed consistently low water contribution and were always associated with healthy tissue. For these reasons, we conclude that despite the fact that the determination of the water concentration is based on a protein model the signal contributions from lipids are unlikely to influence our discrimination results regarding discrimination of tumor and healthy tissue.

Limitations of this study include the fact that we have a limited number of samples (fourteen). Future investigation will also target other subsides within the oral cavity to see if we can extrapolate our results. Also, one can imagine that measurements of the transition zone between tumor and healthy surrounding tissue could be valuable in understanding and explaining the underlying mechanism. This is why we will keep on performing measurements and will try to focus on this peritumoral zone as well.

Another limitation could be the fact that it is still difficult to correlate the measured points with pathology. Even though we used pins to mark the measurement spots, the pathologists found it hard to find the exact measurement spot in some cases. Currently we are thinking of a different approach to mark the measurement spots after measuring, to overcome this problem. This technique could be integrated in a multi-fiber probe which can measure a bigger surface at once (30,31).

Finally, this setup is not yet suitable for intra-operative use. Yet, these results can contribute to creating a method which can be used in an intra-operative system as well. Our ultimate goal would be the scanning of all resection margins, which is still far from the point measurements we describe in this study. Still, we believe that our results, promising as they are, could help to create a method to scan all resection margins.

## Conclusions

In this study, high-wavenumber Raman measurements of fresh SCC tongue resection tissue specimens have demonstrated that SCC has significantly higher water content than surrounding healthy tissue. HWNRS can therefore be used to differentiate tumor and surrounding healthy tissue based on water concentration. The specific spectral information obtained in this study can be used for the development of an in-vivo Raman spectroscopic method for border demarcation of SCC of head and neck. Raman spectroscopy is fast (measurements in the order of 1 second or less with real-time signal analysis) and can be applied through the use of hand-held fiber-optic probes at virtually any location of the head and neck area. This enables the development of both ex-vivo and in-vivo intra-operative applications for the purpose of assisting and guiding oncological surgical procedures towards adequate resection margins.

## References

1. Smits R. W. H., Koljenovic S., Hardillo J. A., *Submitted to Head and Neck*, August 2014.
2. Slotweg P. J., Hordijk G. J., Schade Y., *Oral Oncology*. 2002; 38, 500-503.
3. Loree T. R., Strong E. W., *The American Journal of Surgery*. 1990; 160, 410-414.
4. Kerawala C. J., Ong T. K., *Head & Neck*. 2001; 23, 230-232.
5. DinNardo L. J.; Lin J.; Karageorge L. S.; Powers, C. N., *The Laryngoscope*. 2000; 110, 1773-1776.
6. Ribeiro N. F. F., Godden D. R. P., Wilson G. E., *Int. J. Oral Maxillofac. Surg.* 2003; 32, 152-158.
7. Damadian R., *Science*. 1971; 171, 1151-1153.
8. Trojanowska A., 2011; 16, 207-212.
9. Boyd N. F., Martin L. J., Bronskill M., *Cancer Inst.*, 2010; 102, 1224-1237.
10. Horger M., Fenchel M., Nagele T., *AJR*. 2009; 193, 1384-1387.
11. Pavlisa G., Rados M., Pavlisa G., *Clinical Imaging*. 2009; 33, 96-101.
12. Kono K., Inoue Y., Nakayama K., *Am. J. Neuroradiol.* 2001; 22, 1081-1088.
13. Kiricuta I., Simplaceanu J. V., *Cancer Res.* 1975; 35, 1164-1167.
14. Eggleston J. C., Saryan L. A., Hollis D. P., *Cancer Res.* 1975; 35, 1326-1332.
15. Hazlewood C. F., Chang D. C., Medina D., *Proc. Natl. Acad. Sci.* 1972; 69, 1478-1480.
16. Yu C., Fan S., Sun Y., *Quant. Imaging Med. Surg.* 2012; 2, 33-45.
17. Hall W. A., Truwit C. L., *J Magn Reson Imaging*. 2008; 27(2), 368-75.
18. Wang Y., Minamide H., Tang M., *Optics Express*. 2010; 18.
19. Oh S. J., Kim S., Ji Y. B., *Biomedical Optics Express*. 2014; 5(8), 2837-2842.
20. Garcia-Flores A. F., Raniero L., Canevari R. A., *Teor. Chem. Acc.* 2011.
21. Philipsen P. A., Knudsen L., Gniadecka M., *Photobiol. Sci.* 2013; 12, 770-776.
22. Surmacki J., Musial J., Kordek R., *Molecular Cancer*. 2013; 12-48.
23. Abramczy H., Brozek-Pluska B., Krzesniak M., *Spectrochimica Acta Part A: Molecular and Biomolecular Spectroscopy*. 2014; 129, 609-623.
24. Caspers P. J., Lucassen G. W., Carter E. A., *Journal of Investigative Dermatology*. 2001; 3, 434-442.
25. Wolthuis R., Van Aken M., Fountas K., *Anal. Chem.* 2001; 73, 3915-3920.
26. Youden W. J., *Cancer*. 1950; 3, 32-35.

27. Martens H, Stark E, *Journal of Pharmaceutical & Biomedical Analysis*. 1991; 9(8), 625-635.
28. Koljenović S., Bakker Schut T. C., Wolthuis R., *Journal of Biomedical Optics*. 2005; 10(3), 1-11.
29. Metz C. E., *Seminars in Nuclear Medicine*. 1978; 8(4), 283-298.
30. Bergholt M. S., Zheng W., Huang Z, *Journal of Biomedical Optics*. 2013; 18(3), 1-3.
31. Puppels G. J., Bakker Schut T. C., Caspers P. J., In *Handbook of Raman Spectroscopy*; Lewis, I.R., Edwards, H.G.M. Eds.; Marcel Dekker: New York, 2001; pp 549-574.





## ***CHAPTER 4***

### ***Characterization and subtraction of luminescence background signals in high-wavenumber Raman spectra of human tissue***

E. M. Barroso, T. C. Bakker Schut, P. J. Caspers, I. P. Santos, E. B. Wolvius, S. Koljenović,  
and G. J. Puppels

**Journal of Raman Spectroscopy 2018;1-11**



## Abstract

Raman spectroscopy in the high-wavenumber spectral region (HWR) is particularly suited for fiber-optic in-vivo medical applications. The most-used fiber-optic materials have negligible Raman signal in the HWR. This enables the use of simple and cheap single-fiber-optic probes that can be fitted in endoscopes and needles. The HWR generally shows less tissue luminescence than the fingerprint region. However, the luminescence can still be stronger than the Raman signal.

Hardware- and software-based strategies have been developed to correct for these luminescence signals. Typically, hardware-based strategies are more complex and expensive than software-based solutions. Effective software-strategies have almost exclusively been developed for the fingerprint region. First-order polynomial baseline fitting (PBF) is the most common background/luminescence estimation employed for the HWR.

The goal of this study was to characterize the luminescence background signals of HW spectra of human oral tissue, and compare the performance of two algorithms for correction of these background signals: PBF and multiple regression fitting (MRF). In the MRF method, we introduce here, prior knowledge of the range of Raman signals that can be obtained from the tissues of interest is explicitly used.

MRF is more robust than PBF because it does not require an a priori choice of the polynomial order for fitting the background signal. This is important because, as we show, no single polynomial order can optimally characterize all backgrounds that are encountered in HW tissue spectra. We conclude that MRF should be the preferred method for background subtraction in the HWR.

## Introduction

Raman spectroscopy has been broadly explored for medical applications in oncology aiming at early diagnosis, biopsy guidance and surgery guidance (1-3). The technique can provide qualitative and quantitative molecular information about tissues and enables classification of tissues with high sensitivity and specificity. Raman spectroscopy is directly applicable for in-vivo and ex-vivo analysis of tissue, without the need for labels and/or reagents (4). Elimination of interference from laser-induced tissue luminescence is still a challenge for many medical applications of Raman spectroscopy. This intrinsic luminescence signal can be several orders of

magnitude more intense than the Raman signal, which limits the analysis (5). To overcome this, both hardware- and software-based strategies have been developed to reduce the interference from luminescence (3, 5-29).

An example of a hardware-based strategy is the use of specific excitation wavelengths far from the visible range. For example, the intensity of a fluorophore is dependent on the excitation wavelength. With exception of porphyrins and melanin (17), the excitation and emission of most tissue fluorophores exhibit maxima at ultra-violet (UV) and visible (VIS) wavelengths (18). Thus, longer wavelengths are preferred over UV/VIS (5,6). The selection of appropriate NIR source is an optimization between competing factors. For example, while tissue luminescence decreases with increasing wavelength, also the Raman scattering cross section and the quantum efficiency of CCD detectors decrease. For CCD detectors the quantum efficiency drops below 15% at 1000 nm, and cannot be used at all above 1100nm. Detectors such as indium gallium arsenide (InGaAs), germanium, and indium phosphide can be used for wavelengths above 950 nm. Although these detectors have lower quantum efficiency, and exhibit much more detector noise in comparison to silicon detectors (5), new types of InGaAs detectors are emerging which have very good noise characteristics, approaching those of CCD detectors (6).

Another hardware-based strategy for luminescence rejection is multi-excitation wavelength Raman spectroscopy, also called as shifted excitation Raman difference spectroscopy (SERDS) (29). Raman spectra shift with the excitation wavelength, and luminescence is invariant for small excitation-wavelength shifts. The use of multiple excitation frequencies can thus be employed to separate the Raman signal from the luminescence background. The efficiency of the rejection increases with the number of excitation frequencies, which adds significant complexity to this hardware solution (20). This technique has been mainly used on samples that have spectral bands with similar spectral widths (powders, crystalline proteins, etc). Recently, Cordero et al. (29) demonstrated that this technique may also be applicable for biological tissue, demonstrating SERDS to correct background from chicken meat. They concluded that SERDS could be a good choice for background correction when backgrounds are too complex to be estimated, and when signal-to-noise of the spectra is not a limiting factor (29).

Software-based strategies aim at algorithms to accurately subtract luminescence background signals from tissue spectra. Such algorithms have been widely developed and tested for the fingerprint region of the Raman spectrum ( $400\text{ cm}^{-1}$  to  $2000\text{ cm}^{-1}$ ), including methods based on wavelet transformation (21,22), iterative weighted least squares (23), geometric approach (24), polynomial baseline fitting (7-

9,25), iterative morphological and mollifier-based baseline correction (26), auto-adaptive background (27), and genetic algorithm based cubic spline smoothing (28).

For the high-wavenumber region ( $2500\text{ cm}^{-1}$  to  $4000\text{ cm}^{-1}$ ), these methods have shown limited value, mainly because of limited knowledge about the shape of the luminescence backgrounds of high-wavenumber Raman spectra of human tissues. The high-wavenumber region consists of a small number of relatively broad and overlapping bands, which makes the estimation of the background signals much more difficult than for the fingerprint region. Polynomial subtractions of 1<sup>st</sup> and 5<sup>th</sup> orders are the few and most common solutions mentioned for background correction in the high-wavenumber region (3,10-15). First order polynomial subtraction has been used on high-wavenumber Raman spectra acquired from oral cavity (gingiva, buccal, dorsal tongue, palate), adenomatous polyps, esophageal squamous cell carcinoma, nasopharyngeal tissues and breast tissue (3,10,12-15). The spectra in these studies were acquired with fiber-optic Raman probes and a confocal Raman microscope. The excitation laser wavelengths used were 785 nm and 1064 nm. A 5<sup>th</sup> order polynomial subtraction method has been reported for HW Raman spectra of urine samples, using a confocal Raman system with a 785 nm laser (11).

Raman spectroscopy in the high-wavenumber region demonstrates significant advantages for ex-vivo and in-vivo medical applications when compared to the commonly used fingerprint region. The intensity of the signal is higher, and therefore measurements can be performed in shorter integrations times. Additionally, much used fiber-optic materials like fused silica do not have Raman signal at the high-wavenumber region of the Raman spectrum (30). This enables the use of simple and cheap single fiber optic probes that can be easily inserted in endoscopes and needles to perform in-vivo measurements in hollow organs or surface assessment of solid organs such as oral cavity (31,32), lung (33,34), upper gastrointestinal tract (35-37) and colorectal (14,38).

A study by Koljenović *et al.* showed that, for discriminating cancer from healthy tissue, essentially the same diagnostic information is obtained in either of the two spectral regions (fingerprint or high-wavenumber) (30). Although the high-wavenumber spectra show considerably less interference from tissue luminescence compared to spectra in the fingerprint region, the background luminescence signal in the high-wavenumber can still be some orders of magnitude higher than the Raman signal itself.

This study reports a more elaborate method for luminescence background subtraction from tissue spectra in the HWR. The method is based on a detailed characterization of the shapes of the luminescence background signals in ex-vivo

high-wavenumber Raman spectra of freshly excised oral cavity tissue. The aim of this study was to characterize the luminescence background, and to compare the performance of two algorithms for correction of these backgrounds: the most used algorithm (polynomial baseline fitting) and a multiple regression fitting based method.

## **Materials and Methods**

### **Instrumentation and spectral pre-processing**

For all Raman experiments a confocal Raman microscope was used. The setup comprised a multichannel Raman Module (HPRM 2500, RiverD International B.V., The Netherlands), a 671nm laser (CL671-150-SO, CrystaLaser) and a charge-coupled device (CCD) camera fitted with a back-illuminated deep depletion CDD-chip (Andor 316, Andor Technology Ltd., UK). All the different parts of the instrument are described in detail in earlier work (39,40). All spectra acquired with this setup were calibrated to a relative wavenumber axis, and corrected for the wavelength dependent detection efficiency of the setup. The calibration was performed following the instructions of the spectrometer supplier (RiverD International B.V., The Netherlands). Spectral preprocessing was performed by removal of cosmic ray events and Raman signal generated in the instrument (caused by the passage of laser light through optical components), which was recorded by measuring a Raman spectrum without a sample being present.

### **Luminescence background signal**

Bleaching experiments were performed to evaluate the shapes of the luminescence background signals that are present in ex-vivo high-wavenumber human tissue spectra. The bleaching was induced by continuous exposure of the samples to the focused Raman excitation laser light. This produced spectra with an almost constant Raman contribution and decaying luminescence contributions. In this subsection, the bleaching experiments and the method used to extract the luminescence background signals from these experiments are described.

#### *Tissue samples*

Ex-vivo experiments were performed on fresh resection specimens from patients undergoing surgery for oral cavity squamous cell carcinoma. Informed consent was

obtained from the patients prior to the surgical procedure. The study protocol has been approved by the Medical Ethics Committee of the Erasmus MC, University Medical Center Rotterdam, The Netherlands (MEC-2013-345). The surgeon brought the specimen right after resection to the pathology department. The pathologist performed assessment of resection margins by cutting the specimen, perpendicularly to the resection surface, in about 5mm thick cross sections. After this intra-operative assessment, one of the cross sections was chosen by the pathologist for measurements and the remaining cross sections were immersed in formalin. Blood was rinsed with physiological salt solution (0.9% NaCl) and gently patted dry with gauze. The section was inserted in a cartridge with the tissue in contact with a fused silica window on one side of the cartridge. The window allowed scanning of a 3cm x 3cm tissue area. Experiment time was limited to 60 minutes, after which the section was immersed in formalin and together with the rest of the resection specimen, and followed the standard pathology workflow.

### *Bleaching Experiments to isolate luminescence background signals*

For bleaching experiments Raman spectra were collected from different tissue locations on the freshly excised oral cavity tissue sections. Approximately 80mW of laser light was focused to a spot of 4 $\mu$ m in diameter. Up to 120 spectra with 1 s exposure time were obtained at each measurement location.

In the experiments breakdown of the luminescence molecules was induced by continuous exposure to the focused Raman excitation laser light. Time decay of the luminescence component of the signal and time invariance of the Raman component was determined by calculating difference spectra between consecutive spectra in a bleaching experiment. If difference spectra showed a broad background signal without observable Raman features, the difference between the first spectrum (spectrum with the highest background) and last spectrum (spectrum with the lowest background) was used to estimate the luminescence background signal. If Raman features were present in the difference spectra between the first spectrum and consecutive spectra the experiment was discarded.

### *Optimization of polynomial approximation to the background*

The background signals estimated from each bleaching measurement were normalized, and polynomials of increasing orders from 1st to 10th order were fitted to the normalized backgrounds by the classical least-squares method (41). The norm of the residuals was plotted as a function of polynomial order. The optimal polynomial order was defined as the order after which there was no more significant decrease in residual (<5%).

## **BSA reference spectra**

Bovine serum albumin (BSA) was purchased from Sigma-Aldrich (A9647, 66kDa). Eleven solutions of BSA and water were prepared with mass percentages from 5% to 40%. Per solution 60 spectra were acquired with an exposure time of 1s and then averaged, resulting in a set of reference spectra characterized by a low background signal and varying fractions of protein and water ( $\text{CH}_3$  stretching vibrations, 2910-2965  $\text{cm}^{-1}$ , and OH stretching, 3350-3550 $\text{cm}^{-1}$ ). First order polynomial subtraction was used to subtract the little existing background signal.

## **Tissue reference spectra**

A total of 10147 tissue spectra, collected in Raman mapping experiments described earlier (40), were used to create a set of tissue reference spectra with low luminescence backgrounds and a high variance with respect to Raman content. Ratios between peak content and background content were calculated based on the 2910  $\text{cm}^{-1}$  - 2965  $\text{cm}^{-1}$   $\text{CH}_3$  stretching band. A first order polynomial baseline was fitted between the spectral points at 2910  $\text{cm}^{-1}$  and 2965  $\text{cm}^{-1}$ . Peak content was calculated as the integrated area above this baseline. Background was calculated as the integrated area below the baseline. The spectra with the 25% highest  $\text{CH}_3$  content to background ratio were selected for the reference set. These spectra were scaled on the mean of the data set by an extended multiplicative scatter correction (EMSC) algorithm (41,42). Hierarchical cluster analysis (HCA) was used to find the largest clusters in the group of the spectra with the 25% highest  $\text{CH}_3$  content to background ratio. Principal component analysis (PCA) was first used for data reduction (43). The clustering method was Ward's agglomerative algorithm with 1- $R^2$  as the distance metric, where  $R^2$  is the squared Pearson's correlation coefficient. The result of the HCA is a membership matrix  $N \times N$  ( $N$  is the number of spectra) that represents the clustering at each level of agglomeration (44). The largest clusters, comprising 90% of the spectra (from the group of spectra with the 25% highest  $\text{CH}_3$  content to background ratio), were selected as a representation of the most common tissue structures present in the oral cavity with the lowest luminescence background. Cluster averages were calculated, and the residual background subtracted by 1st order polynomial baseline fitting.

## **Algorithms for luminescence background subtraction**

Two algorithms were compared for characterization and subsequent subtraction of luminescence background signals: a polynomial baseline fitting (PBF) algorithm and an algorithm based on multiple regression fitting (MRF).

### *Polynomial baseline fitting algorithm*

The PBF algorithm used is an iterative function that fits a polynomial, of a user-specified order, through a selected set of spectral points. In the first iteration, all points of the spectrum are used, and in each iteration the number spectral points are reduced by only including spectral points with lower intensity than the fitted polynomial at those points. In this way, the polynomial is iteratively adapted to fit the lowest points of the spectrum. The iteration is stopped when the number of points used for the baseline fit is below a threshold set by the user. Finally, the offset of fitted baseline polynomial is adapted to ensure that the value of the fitted baseline was never above the value the spectrum over the whole spectral range.

### *Multiple regression fitting algorithm*

In the MRF method the spectra were fitted with a set of library spectra (independent variables), that have low background, and a polynomial, of a user-specified order, using a non-negative least squares method (constraining fit coefficients to greater or equal to zero).

## **Algorithm performance evaluation**

The performance of the PBF and MRF algorithms was evaluated using two artificial data test sets that were constructed from the extracted luminescence background spectra, BSA reference spectra, and tissue reference spectra described above. Different luminescence background spectra were digitally added to the reference sets, which resulted in test spectra for which the luminescence background component was exactly known. The result of the luminescence background correction methods was compared to the corresponding reference spectrum (without artificially added luminescence background). Performance of the two background correction algorithms was evaluated for different values of the polynomial order to define optimal values for both methods. Evaluation criteria were the similarity between the background corrected spectrum and the original spectrum using Pearson's correlation coefficient, and secondly, the influence of the background correction on the calculated water percentage. The water concentration was calculated from the ratio of the Raman bands at 3390 and 2935  $\text{cm}^{-1}$ , as described by Caspers *et al* (45).

## Results

### Luminescence background signal data set

#### *Tissue samples & Bleaching experiments*

Bleaching experiments were performed to isolate the luminescence background signals that are present in ex-vivo tissue spectra. Freshly excised oral cavity specimens from 6 patients were analyzed on a total of 35 different tissue locations. An example of a bleaching experiment is presented in the figure 1.a.

#### *Optimization of polynomial approximation to the background*

Table S1 (Supporting Information) shows the residuals of the polynomial fits to the 35 different luminescence background spectra and the optimal polynomial order. The results for orders 1 to 7 are shown in the table. Three out of the 35 luminescence backgrounds were optimally approximated by a 1st order polynomial (8%), 22 background signals were optimally approximated by a 2nd order polynomial (63%), 8 by a 3rd order polynomial (23%), and 2 by 4th order polynomial (6%). An example of the polynomial approximation to the background can be seen in the figure 1.b-d.

### BSA test data set

Figure 2 shows the reference set of a total of 11 spectra of BSA solutions with different mass-percentages (4.92%, 5.91%, 9.86%, 14.80%, 19.74%, 24.70%, 29.66%, 31.65%, 34.64%, 37.62% and 39.61%). Eight spectra were used for testing of the PBF and MRF algorithms. The remaining 3 spectra were used as independent data in the MRF algorithm. Each of the 8 BSA reference spectra was combined with all 35 different background luminescence spectra, resulting in a total test set of 280 spectra shown in figure 2.b.

### Tissue test data set

A total of nineteen tissue reference spectra with low luminescence background were obtained, which are shown in figure 3.a. Thirteen spectra were used for testing of the PBF and MRF algorithms.

**Table S1 - Residuals of the luminescent background approximations using increasing polynomial orders (1st to 7th order). OPO: optimal polynomial order, order at which the residual does not further decrease (<5%).**

Background	Residuals per polynomial approximation (%)							OPO
	1 <sup>st</sup>	2 <sup>nd</sup>	3 <sup>rd</sup>	4 <sup>th</sup>	5 <sup>th</sup>	6 <sup>th</sup>	7 <sup>th</sup>	
1	2.0	0.5	0.5	0.5	0.5	0.5	0.5	2
2	1.6	1.3	1.3	1.3	1.3	1.3	1.3	2
3	1.5	0.6	0.6	0.6	0.6	0.6	0.6	2
4	0.3	0.2	0.2	0.2	0.2	0.2	0.2	2
5	0.9	0.8	0.7	0.7	0.7	0.7	0.7	3
6	0.9	0.3	0.3	0.3	0.3	0.3	0.3	2
7	1.1	1.1	1.1	1.1	1.1	1.1	1.1	1
8	1.9	1.7	1.7	1.7	1.7	1.6	1.6	2
9	2.8	1.9	1.9	1.9	1.9	1.9	1.9	2
10	2.7	1.5	1.3	1.3	1.3	1.3	1.3	3
11	2.6	1.2	0.8	0.8	0.8	0.8	0.8	3
12	3.4	2.3	1.7	1.6	1.6	1.6	1.6	4
13	3.5	2.7	2.5	2.5	2.5	2.5	2.5	3
14	4.3	3.5	3.1	3.0	3.0	3.0	3.0	4
15	1.7	1.0	1.0	1.0	1.0	1.0	1.0	2
16	6.5	6.3	6.3	6.3	6.3	6.3	6.3	2
17	2.3	1.2	1.2	1.2	1.2	1.2	1.2	2
18	1.7	1.2	1.2	1.2	1.2	1.2	1.2	2
19	1.3	0.8	0.8	0.8	0.8	0.8	0.8	2
20	1.8	1.0	1.0	1.0	1.0	1.0	1.0	2
21	2.3	1.6	1.6	1.6	1.6	1.6	1.6	2
22	2	1.3	1.3	1.3	1.3	1.3	1.3	2
23	3.1	2.2	2.2	2.2	2.2	2.2	2.2	2
24	2.9	1.2	1.0	1.0	1.0	1.0	1.0	3
25	6.0	5.8	5.8	5.8	5.8	5.8	5.8	2
26	1.2	0.3	0.3	0.3	0.3	0.3	0.3	2
27	1.6	0.8	0.8	0.8	0.8	0.8	0.8	2
28	0.8	0.7	0.7	0.7	0.7	0.7	0.7	2
29	2.7	2.7	2.7	2.6	2.6	2.5	2.5	1
30	1.5	0.2	0.2	0.2	0.2	0.2	0.2	2
31	2.6	1.4	1.3	1.3	1.3	1.3	1.3	3
32	2.1	1.0	1.0	1.0	0.9	0.9	0.9	2
33	1.2	0.7	0.6	0.6	0.6	0.6	0.6	3
34	1.7	1.3	1.1	1.1	1.1	1.1	1.1	3
35	3.0	3.0	2.8	2.8	2.8	2.8	2.8	1

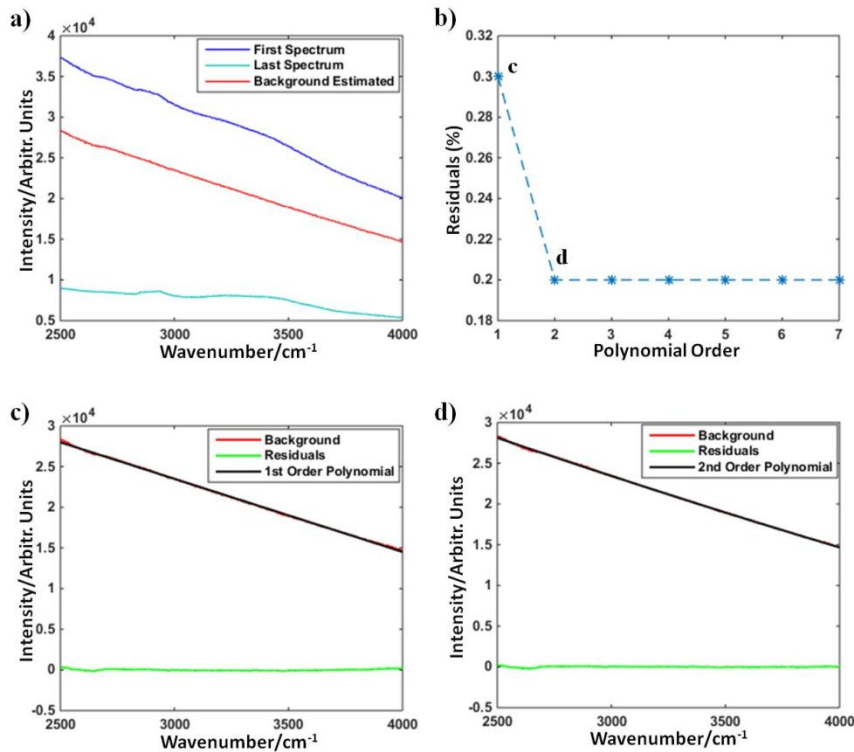


**Figure 1.** Example of background estimation from a bleaching experiment. a) Bleaching time-series: first spectrum (dark blue), last spectrum (light blue) and the difference between the two as the estimated background (red). b) Residuals for different polynomial order fits to the estimated background. c) Estimated background (red), fitted 1<sup>st</sup> order polynomial (black), and residual (green). d) Estimated background (red), optimal (2<sup>nd</sup> order) polynomial (black), and residual (green). The optimal polynomial order is defined as the minimal order after which there was no more significant decrease in residual (<5%).

The remaining 6 spectra were used as independent data in the MRF algorithm and. Each of the 13 tissue reference spectra was combined with all 35 different background luminescence spectra, resulting in a total test set of 455 spectra shown in figure 3.b.

The mean and the standard deviation of the Pearson's correlation coefficients are shown per test data set and per algorithm used for testing. The table also shows the mean and the standard deviations of the differences in calculated water concentrations.

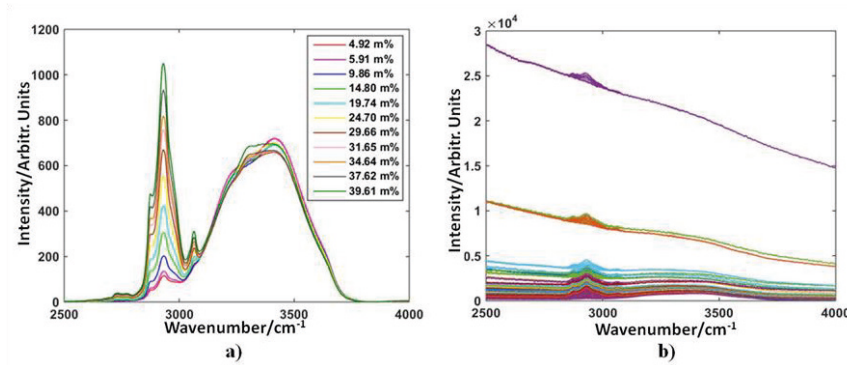


Figure 2. BSA reference spectra data set and BSA spectra test set. a) Averaged Raman high-wavenumber spectra from different albumin solutions. The mass percentage (m%) of the solutions varied between 5% and 40%. For better visualization of Raman signal the low intensity background was subtracted as a 1st order polynomial. b) BSA spectra test set: 280 Raman spectra with BSA signal and luminescence content.

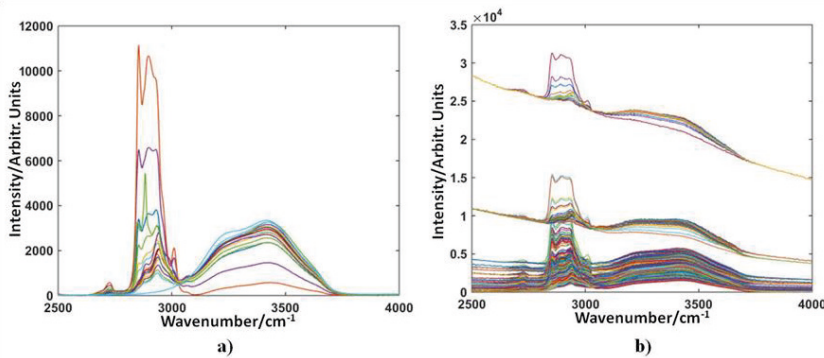


Figure 3. Ex-vivo high-wavenumber tissue reference spectra data set and high-wavenumber tissue spectra test set. a) Nineteen ex-vivo high-wavenumber tissue reference spectra with low luminescence background were obtained after cluster analysis of the low luminescence spectra in the ex-vivo tissue spectra data set. For better visualization of Raman signal the low intensity background was subtracted as a 1st order polynomial. b) Ex-vivo high-wavenumber tissue spectra test set: 455 Raman spectra with known Raman and luminescence content.

## Algorithm performance evaluation

### *BSA test data set*

For all 280 spectra of the BSA test data set, the background was estimated with the two algorithms using a 1st, 2nd, 3rd, 4th and 5th polynomial order and subtracted.

The similarity of the background-corrected data with the original data is listed in table 1.

Examples for the PBF algorithm with 1st, 3rd and 4th polynomial order are shown in figure 4.a-4.c. The distributions of the corresponding Pearson's correlation coefficients are shown in figure 4.d. Examples for the MRF algorithm with 1st, 2nd and 4th polynomial order are shown in figure 4.e-4.g. The distributions of the corresponding Pearson's correlation coefficients are shown in figure 4.h.

**Table 1 - Evaluation of the performance of the PBF and PRF algorithms on BSA spectra and on ex-vivo high-wavenumber tissue spectra. Average +/- standard deviation of the Pearson's correlation coefficient between background corrected spectra and their reference spectra for the two different correction algorithms (PBF and MRF) and different values of the algorithm background polynomial. Average and standard deviation of the absolute error in water concentration (%) between background corrected spectra and their reference spectra for the two different correction algorithms and different values of the algorithm background polynomial.**

Background Polynomial	BSA Spectra			
	Pearson's Correlation Coefficient		Absolute error in [H <sub>2</sub> O] (%)	
	PBF	MRF	PBF	MRF
1 <sup>st</sup> order	0.973±0.076	0.974±0.075	2.74±10.60	2.74±10.60
2 <sup>nd</sup> order	0.995±0.009	0.996±0.006	0.64±0.57	0.61±0.52
3 <sup>rd</sup> order	0.993±0.021	0.996±0.006	0.74±1.22	0.56±0.48
4 <sup>th</sup> order	0.747±0.136	0.996±0.007	29.24±34.10	0.58±0.54
5 <sup>th</sup> order	0.516±0.197	0.996±0.006	46.54±16.39	0.58±0.52
Background Polynomial	Tissue Spectra			
	Pearson's Correlation Coefficient		Absolute error in [H <sub>2</sub> O] (%)	
	PBF	MRF	PBF	MRF
1 <sup>st</sup> order	0.996±0.008	0.996±0.007	0.81±1.30	0.81±1.30
2 <sup>nd</sup> order	0.996±0.010	0.997±0.007	0.62±1.00	0.52±0.72
3 <sup>rd</sup> order	0.996±0.010	0.997±0.006	0.60±0.82	0.48±0.54
4 <sup>th</sup> order	0.728±0.140	0.997±0.007	12.99±22.30	0.48±0.53
5 <sup>th</sup> order	0.578±0.200	0.997±0.007	37.00±13.97	0.49±0.52

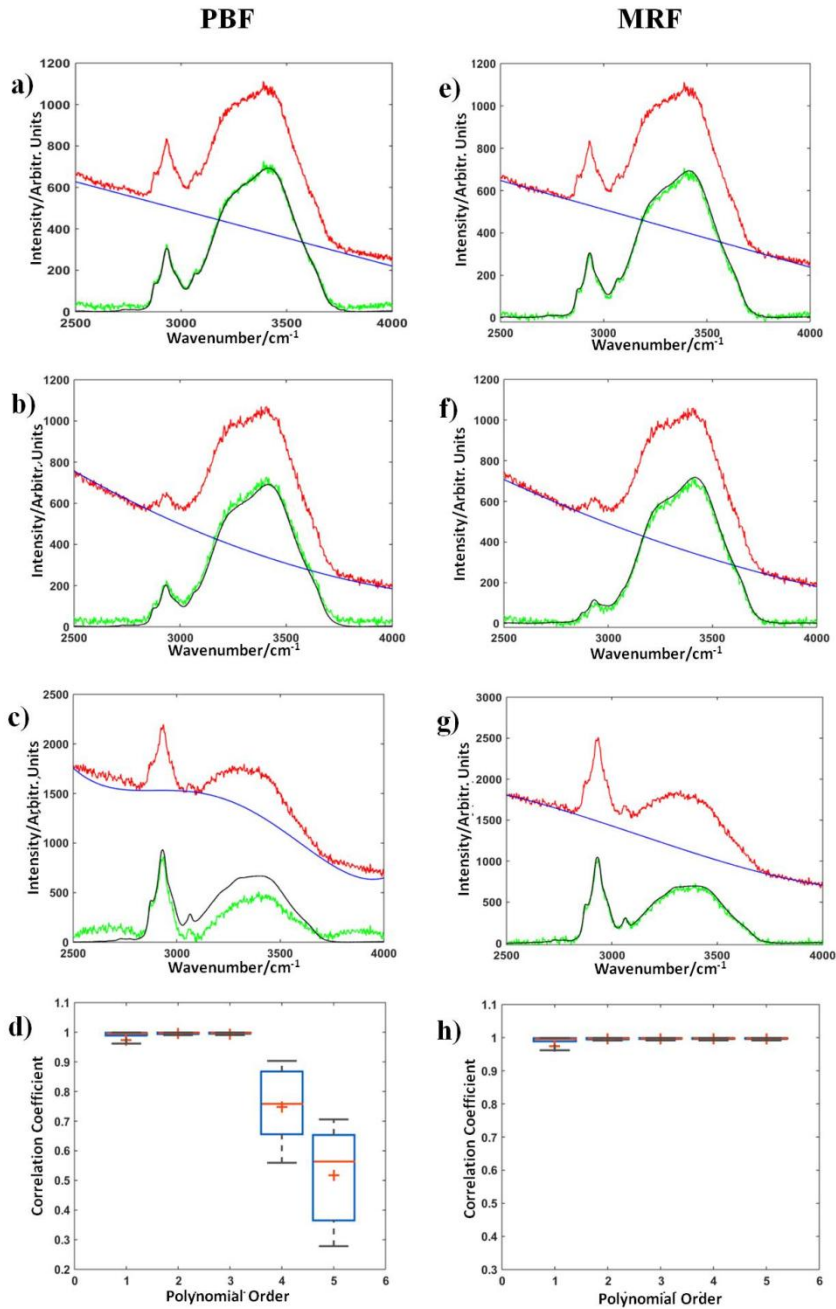


**Figure 4.** Luminescence background correction on BSA test data using the PBF and MRF algorithms. PBF results are shown in the left column, MRF results in the right column. a) Example of PBF 1<sup>st</sup> order polynomial background subtraction. b) PBF 2<sup>nd</sup>

order polynomial. c) PBF 4<sup>th</sup> order polynomial. d) Box-plot of the Pearson's correlation coefficients for PBF with different polynomial orders. e) Example of MRF 1<sup>st</sup> order polynomial background subtraction. f) MRF 2<sup>nd</sup> order polynomial. g) MRF 4<sup>th</sup> order polynomial. Spectra displayed: test spectrum (red), estimated background (blue), corrected spectrum (green), corresponding reference spectrum (black).

### *Tissue reference test data set*

For all 455 spectra of the tissue test data set, the background was estimated with the two algorithms using a 1st, 2nd, 3rd, 4th and 5th polynomial order. The similarity of the background-corrected data with the original data and the errors in calculated water concentration after background correction are listed in table 1. The figure 5 shows tissue reference spectra that were used that were used as independent variables in the MRF algorithm. Two examples of the results obtained using PBF algorithm and MRF algorithm are shown in figure 6.a-6.d.

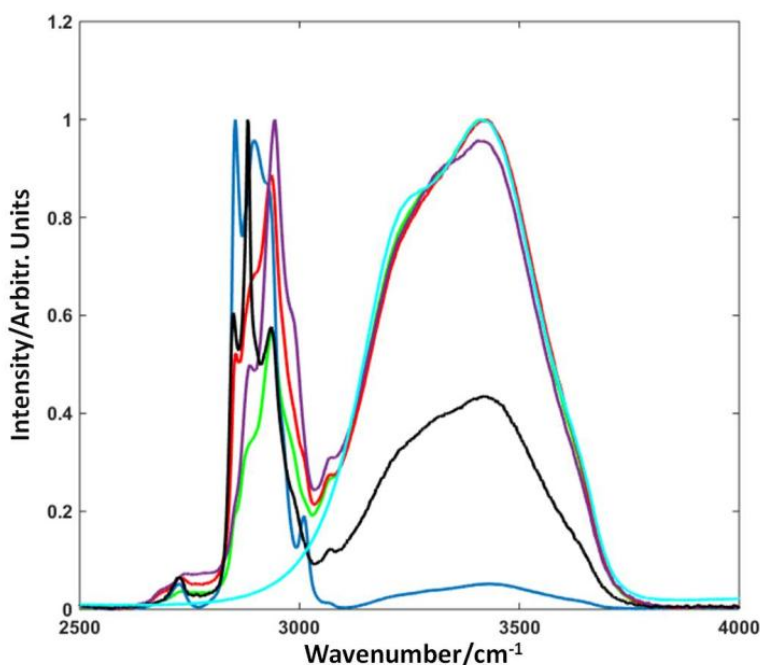


**Figure 5.** The 6 ex-vivo high-wavenumber tissue reference spectra that were used as independent variables in the MRF algorithm. For better visualization of the differences in the Raman signal the spectra were normalized.

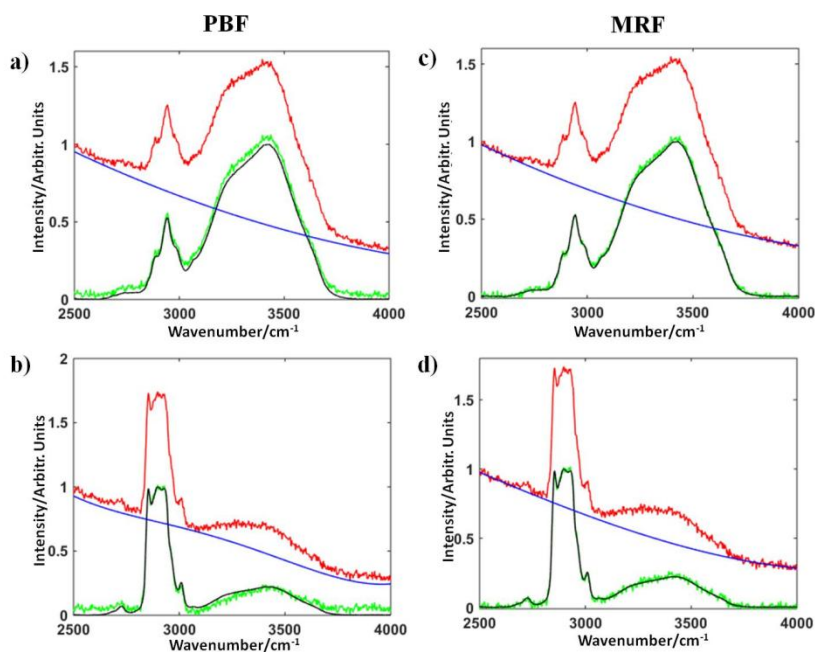


**Figure 6.** Luminescence background correction on tissue test data using the PBF and MRF algorithms. PBF results are shown in the left column, MRF results in the right column. a) Example of PBF 2nd order polynomial background subtraction. b) PBF 4th order polynomial. c) MRF 4th order polynomial. d) MRF 4th order polynomial. Test spectrum (red), estimated background (blue), corrected spectrum (green), corresponding reference spectrum (black).

## Discussion & Conclusions

When measuring Raman spectra from biological tissue, high luminescence backgrounds can (almost) completely obscure the Raman signal. Both hardware- and software-based strategies have been developed to correct for these luminescence background signals.

Hardware-based strategies can be efficient, but their implementation is associated with higher instrument complexity and associated higher costs. Software-based strategies are easier to implement and have lower costs. Most software-based strategies have been developed for the fingerprint region. In contrast to the fingerprint region, not many background subtraction algorithms have been developed for the high-wavenumber region of the Raman spectrum (7,9,21-28,47).

For high-wavenumber region spectra, polynomial baseline fitting (PBF) is the only solution mentioned for background correction, using either a 1<sup>st</sup> order (3,10,12-15), or a 5<sup>th</sup> order polynomial (11). However, this method produced unsatisfactory results for our ex-vivo high-wavenumber spectra of human oral tissues. First, we experienced that not all luminescence backgrounds could be characterized by a first order polynomial, and the estimation of the background by higher order polynomials did not produce stable results. We observed that the polynomial fits have problems in distinguishing between luminescence background and the rather broad band Raman spectral features in the high-wavenumber region.

Therefore, in this article, we present a new and effective method for correction of luminescence backgrounds in high-wavenumber region Raman spectra. The method is based on multiple regression fitting (MRF) and on high-wavenumber luminescence-free Raman signal. The goal of this study was to characterize the luminescence background signals of ex-vivo human oral tissue high-wavenumber region spectra, and to compare the performance of the MRF method with the more common polynomial background fitting (PBF).

The luminescence background signals were measured in laser-induced bleaching experiments on freshly excised human oral tissue. The bleaching process was not complete for all the bleaching experiments performed, due to time constraints (fresh specimen(s) that needed to be sent to pathology department). Although the estimated backgrounds did not bleach completely, we do not believe that this affects the outcome of this study in any way.

Polynomials of different order were required for optimal approximation of the luminescence backgrounds, ranging from 1<sup>st</sup> order (8% of the cases), 2<sup>nd</sup> order (63% of the cases), 3<sup>rd</sup> order (23%), to 4<sup>th</sup> order (6%). These results indicate that it is not possible to choose a single optimal polynomial order that will give the best background estimation for all cases. Hence operator-supervision is required, and inter-operator subjectivity may play a role. Moreover, the selection of a polynomial order that is not optimal can result in significant artifacts in the Raman spectrum from residual luminescence contributions or from removal of Raman signal by polynomial over-fitting.

The luminescence background signals obtained from the bleaching experiments were used to generate test data sets of spectra with known luminescence and Raman contributions (figures 2-3). For the Raman contributions two different datasets were used: a set of spectra from pure BSA solutions with different concentrations, and fresh ex-vivo tissue spectra from oral cavity tissue with very low luminescence background. Because the luminescence backgrounds in the test data sets were

digitally added, the test data enabled accurate evaluation of the performance of the background subtraction algorithms (figures 4-6). Evaluation criteria were spectral correlation and error in the calculated water content after background correction, as compared to the corresponding reference spectra. The results in table 1 show that for both datasets MRF performs equally well or better than PBF for all the polynomial background orders evaluated. The results test show that the MRF is more robust and more effective than PBF in accurately estimating the luminescence background in HWR tissue and BSA spectra. Also, here, it is clear that the MRF algorithm gives significantly better results when higher order polynomials are used in the fitting process. For the tissue reference test data set the MRF algorithms gives better results, and again especially for the higher order polynomials.

For the classical PBF method, the overall best results were obtained by fitting a 2<sup>nd</sup> order polynomial. This is mainly determined by the observation that the luminescence backgrounds obtained from the bleaching experiments predominantly had a 2<sup>nd</sup> order polynomial shape. Higher polynomial orders lead to large errors due to over-fitting artifacts. This is a common risk in polynomial background fitting of HWR Raman spectra of tissues because these spectra are characterized by broad partially overlapping bands, and because no reliable baseline points are available to anchor the central part of the spectrum around 2800-3800 cm<sup>-1</sup>. As a result, the broad high-wavenumber Raman bands are partly fitted as background by higher order polynomials (see figure 4.c).

For MRF, 2<sup>nd</sup> order polynomials or higher gave the best results. This confirms that the MRF-method is robust and can be reliably used with higher order polynomials, because the Raman signal is fitted by the independent spectra included in the method. Thus, higher order polynomials do not result in fitting of the Raman signal as background. The MRF algorithm is not dependent of the shape of the Raman signal, provided that the independent data set of luminescence free Raman spectra is representative of the Raman signal variance measured. This effectively eliminates subjectivity in choosing an optimal polynomial order, as required by the PBF method, and the associated problem that a single optimal polynomial order does not exist for a variety of backgrounds, as shown in the results section.

The results of this study were obtained on high-wavenumber region Raman spectra. However, we believe that the method may not be limited to this spectral region but may prove equally useful for luminescence background correction in the fingerprint region. Further studies will be conducted to prove the usefulness of MRF for luminescence background subtraction in the fingerprint region.

In conclusion, this study has demonstrated that MRF is a more accurate and robust solution than PBF for correction of luminescence backgrounds and can be used for unsupervised and automated background subtraction as needed in real time tissue diagnostic applications.

## References

1. Kallaway C., Almond L. M., Barr H., *Photodiagnosis Photodyn Ther.* 2013; 3 , 10.
2. Broadbent B., Tseng J., Kast R., *J. Neurooncol.* 2016; 1 , 130.
3. Wang J., Lin K., Zheng W., *Sci Rep.* 2015; August , 5.
4. Çulha M., *Bioanalysis.* 2015; 21 , 7.
5. Pence I., Mahadevan-Jansen A., *Chem Soc Rev.* 2016; 7 , 45.
6. Santos I. P., Caspers P. J., Bakker Schut T. C., *J Raman Spectrosc.* 2015; 7 , 46.
7. Gallo C., Capozzi V., Lasalvia M., *Vib Spectrosc.* 2016; 83.
8. Beier B. D., Berger A. J., *Analyst.* 2009; 6 , 134.
9. Lieber C. A., Mahadevan-Jansen A., *Appl Spectrosc.* 2003; 11 , 57.
10. Huang W., Wu S., Chen M., *J Raman Spectrosc.* 2015; 6 , 46.
11. Brindha E., Rajasekaran R., Aruna P., *Spectrochim Acta - Part A Mol Biomol Spectrosc.* 2017; 171.
12. García-Flores A. F., Raniero L., Canevari R. A., *Theor Chem Acc.* 2011; 4-6 , 130.
13. Liu W., Sun Z., Chen J., *J. of Spectroscopy.* 2016; Volume 2016.
14. Bergholt M. S., Lin K., Wang J., *J Biophotonics.* 2016; 4 , 9.
15. Bergholt M. S., Zheng W., Huang Z., *J Biomed Opt.* 2013; 3 , 18.
16. Santos I. P., Caspers P. J., Bakker Schut T. C., *Anal Chem.* 2016; 15 , 88.
17. Huang Z., Zeng H., Hamzavi I., *J Biomed Opt.* 2006; 3 , 11.
18. Lakowicz J. R., *Principles of Spectroscopy*, MA: Springer US, Boston, 2006.
19. Carvalho L. F. C. S., Bonnier F., O'Callaghan K., *Proc. SPIE 9531, Biophotonics South America.* 2015; 9531.
20. McCain S. T., Willett R. M., Brady D. J., *Opt Express.* 2008; 15 , 16.
21. Galloway C. M., Le Ru E. C., Etchegoin P. G., *Appl Spectrosc.* 2009; 12 , 63.
22. Zhang Z. M., Chen S., Liang Y. Z., *J Raman Spectrosc.* 2010; 6 , 41.
23. Ruan H., Dai L. K., *Asian J Chem.* 2011; 12 , 23.
24. Kourkoumelis N., Polymeros A., Tzaphlidou M., *Spectrosc An Int J.* 2012; 5-6 , 27.
25. Wang T., Dai L., *Appl Spectrosc.* 2016; 0 , 0.
26. Koch M., Suhr C., Roth B., *J Raman Spectrosc.* 2016; July 2016.
27. Xie Y., Yang L., Sun X., *Spectrochim Acta - Part A Mol Biomol Spectrosc.* 2016; 161.

28. He S., Fang S., Liu X., *Chemom Intell Lab Syst.* 2016;152.
29. Cordero E., Korinth F., Stiebing C., *Sensors.* 2017; 1724.
30. Koljenović S., Bakker Schut T. C., Wolthuis R., *Journal of Biomedical Optics.* 2005; 3 , 10.
31. Krishna H., Majumder S. K., Chaturvedi P., *J Biophotonics.* 2014; 9, 7.
32. Guze K., Pawluk H. C., Short M., *Head Neck.* 2015; 4 , 37.
33. Short M. A., Lam S., McWilliams A., *Opt Lett.* 2008; 7 , 33.
34. McGregor H. C., Short M. A., McWilliams A., *J Biophotonics.* 2017; 1 , 10.
35. Teh S. K., Zheng W., Ho K. Y., *Br J Cancer.* 2008; 2 , 98.
36. Bergholt M. S., Zheng W., Lin K., *Analyst.* 2010; 12 , 135.
37. Duraipandian S., Bergholt M. S., Zheng W., *J Biomed Opt.* 2012; 10 , 17.
38. Short M. A., Tai I. T., Owen D., *Opt Express.* 2013; 4 , 21.
39. Barroso E. M., Smits R. W. H., Bakker Schut T. C., *Anal Chem.* 2015; 4 , 87.
40. Barroso E. M., Smits R. W. H., van Lanschot C. G. F., *Cancer Res.* 2016; 20 , 76.
41. Vickers T. J., Wambles R. E. J., Mann C. K., *Appl Spectrosc.* 2001; 4 , 55.
42. Martens H., Stark E., *J Pharm Biomed Anal.* 1991; 8 , 9.
43. Jolliffe I. T., *Principal Component Analysis*, Second Edition, Springer-Verlag, New York, 2002.
44. Jain A. K., Murty M. N., Flynn P. J., *ACM Comput Surv.* 1999; 3 , 31.
45. Caspers P. J., Lucassen G. W., Carter E. A., *J Invest Dermatol.* 2001; 3 , 116.
46. Wang B. -G., Konig K., Halbhuber K. -J., *J of Microsc.* 2010; 238.
47. Bonnier F., Ali S. M., Knief P., *Vibrational Spectroscopy.* 2012; 61.





## ***CHAPTER 5***

### ***Water concentration analysis by Raman spectroscopy to determine the location of the tumor border in oral cancer surgery***

E. M. Barroso<sup>†</sup>, R. W. H. Smits<sup>†</sup>, C. G. F. van Lanschot, P. J. Caspers, I. ten Hove, H. Mast, A. Sewnaik, J. A. Hardillo, C. A. Meeuwis, R. Verdijk, V. Noordhoek Hegt, R. J. Baatenburg de Jong, E. B. Wolvius, T. C. Bakker Schut, S. Koljenović, G. J. Pupples

<sup>†</sup> These authors contributed equally to this work.

**Cancer Research 2016;76(20)**



## Abstract

Adequate resection of oral cavity squamous cell carcinoma (OCSCC) means complete tumor removal with a clear margin of more than 5 mm. For OCSCC 85% of the surgical resections appear inadequate. Raman spectroscopy is an objective and fast tool that can provide real-time information about the molecular composition of tissue and has the potential to provide an objective and fast intra-operative assessment of the entire resection surface. A previous study demonstrated that OCSCC can be discriminated from healthy surrounding tissue based on the higher water concentration in tumor.

In this study we investigated how the water concentration changes across the tumor border towards the healthy surrounding tissue on freshly excised specimens from the oral cavity. Experiments were performed on tissue sections from 20 patients undergoing surgery for OCSCC. A transition from a high to a lower water concentration, from tumor ( $76\% \pm 8\%$  of water) towards healthy surrounding tissue ( $54\% \pm 24\%$  of water), takes place over a distance of  $\approx 4$  to 6 mm across the tumor border. This was accompanied by an increase of the heterogeneity of the water concentration in the surrounding healthy tissue. The water concentration distributions between the regions were significantly different ( $p$ -values  $< 0.0001$ ). This new finding highlights the potential of Raman spectroscopy for objective intra-operative assessment of the resection margins.

## Introduction

Oral cavity cancer is a major public health issue, with 300,000 new cases per year worldwide (1). Most oral cancers arise from the epithelium of the mucosal surface and are referred to as oral cavity squamous cell carcinoma (OCSCC). OCSCC mortality is high, with a 5-year survival of around 50% and 145,000 deaths per year worldwide (1,2). Despite advances in treatment modalities (surgery, radiotherapy and chemotherapy), these numbers have not shown significant improvement over the last decades (3,4). Important determinants of the clinical outcome of OCSCC patients are tumor subsite, TNM classification, age, comorbidity, and tumor histological characteristics (5-7). Surgery is the mainstay of treatment for OCSCC. Adequate tumor resection with acceptable remaining function and physical appearance is the main goal. At our institute, we follow the guidelines of the Royal College of Pathologists (United Kingdom). The distance between tumor and the nearest resection surface (DBTNRS) determines the adequacy of the surgical

procedure. This distance is histologically measured in mm. A resection margin can be classified as clear (>5 mm of DBTNRS), close (1 to 5 mm of DBTNRS) and positive (<1 mm of DBTNRS) (8). Clear margins are regarded as adequate, close and positive margins as inadequate. Adequate resection margins are crucial for disease control and survival (8-14). Patients with inadequate resection margins often receive adjuvant therapy (chemotherapy and/or radiation), or re-resection. However, these can have a negative effect on patient morbidity.

Achieving adequate resection margins is challenging. The lack of reliable intra-operative guidance and the proximity of tumors to vital structures are the common causes of inadequate tumor resection. Despite comprehensive preoperative imaging of the tumor (by CT scan, MRI etc.), the surgeon decides where to cut, based on visual inspection and palpation of the tumor during the operation. Earlier, we have reported the surgical results obtained in two Dutch centers (Erasmus Medical Center Rotterdam and Leiden University Medical Center). For OCSCC surgery adequate resection margins were obtained in only 15% of the cases (9). A similar result was recently reported by the Harborview Medical Center and the University of Washington Medical Center in Seattle (USA) (11). Clearly, visual inspection and palpation of the tumor and surrounding tissue by the surgeon are insufficient to warrant adequate tumor resection.

Intra-operative assessment of resection margins by means of a frozen section procedure can be used (15). This procedure, in which the pathologist performs microscopic evaluation of a piece of suspicious tissue, is currently the gold standard of intra-operative diagnostics (15-17). The main limitation of the frozen section procedure is that only a fraction of the resection margins can be investigated. The method is prone to sampling error, which often leads to false negative results (9,18). As a result, the frozen section procedure is not very effective in improving surgical success rate. Ideally, the entire resection surface should be evaluated intra-operatively, which requires an objective and fast technology.

Intra-operative assessment of resection margins on the resection specimen (i.e. specimen driven approach) has been reported to be superior to assessment of the wound bed (i.e. defect driven approach) by different groups. Specimen driven intra-operative assessment of resection margins leads to a higher surgical success rate and increase of patient survival than defect-driven or no intra-operative assessment at all (11,17-19).

Various techniques like ultrasonography, imprint cytology, and various optical techniques are being explored for intra-operative use in surgical oncology (20-28). Some of these techniques are being applied for OCSCC, which were recently

reviewed by Ravi et al (2014). Optical techniques like high-resolution micro-endoscopy (HRME), optical coherence tomography (OCT), fluorescence spectroscopy, elastic light scattering spectroscopy, and Raman spectroscopy are promising because of their ease of use, relatively low cost and high speed in screening large tissue areas (20-28).

Raman spectroscopy is an optical technique that is being investigated for intra-operative evaluation of the surgical margins. Raman spectroscopy can be applied to assess the mucosa, as well as, the deep soft tissue layers (29-34). It is an objective technique based on inelastic scattering of monochromatic light that provides detailed quantitative and qualitative information about the molecular composition of tissue. The technique is non-destructive and there is no need for reagents or labeling, which promotes easier translation to the clinics (35,36).

The goal of our research is to develop a Raman spectroscopic technique for objective intra-operative assessment of the entire resection surface, with the ultimate goal to improve the success rate of OCSCC surgery. In a first pilot study we have demonstrated that Raman spectra of resection specimen discriminated tumor from healthy surrounding tissue with a sensitivity of 99% and a specificity of 92% (37). The primary discriminating factor of the Raman spectra proved to be the water concentration in the tissue. Raman spectroscopy is very suitable for rapid quantitative determination of the water concentration in tissue, as has been demonstrated by our group (38-40). The objectives of the current study were to investigate how the change in water concentration correlates with the border between tumor and surrounding healthy tissue and, consequently, to verify if this information can be used to assess resection margins.

## Material and Methods

### Medical Ethical Approval

This study was approved by the Medical Ethics Committee (MEC-2013-345) of the Erasmus MC Cancer Institute, University Medical Center Rotterdam. Prior to the operation, informed consent was obtained from the patients. Measurements were conducted ex-vivo on resection specimen of patients undergoing surgery for OCSCC. The allowed time for the experiments was 60 minutes, after which the resection specimen was put in formalin for routine histopathological evaluation.

## Tissue samples and handling

Immediately after resection, the surgeon brought the specimen to the cutting room of the pathology department, which is in close proximity to the operating room. A dedicated pathologist and surgeon inspected the specimen together. This process included labeling of the anatomic sites and documentation of the specimen with diagrams and digital images (Figure 1.1).

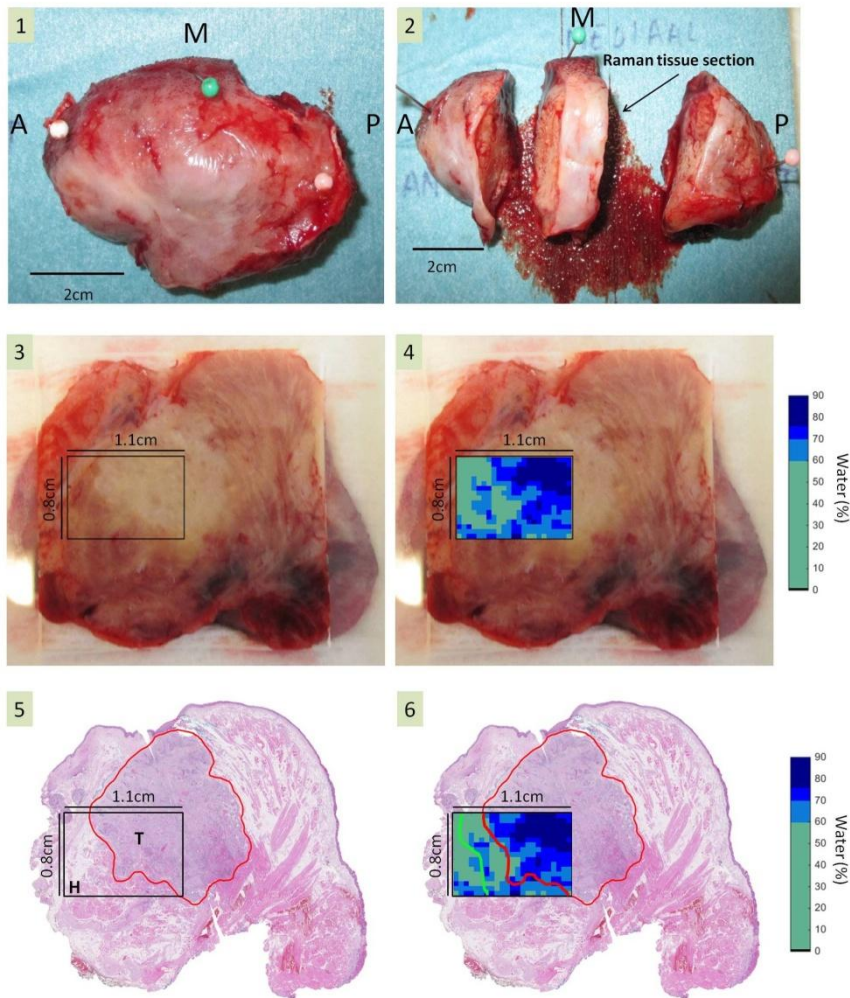


**Figure 1. Overview of the experimental protocol. 1. Immediately after surgical resection, the specimen (excision of tongue SCC) was transferred to the pathology room and orientation was digitally recorded (anterior (A), posterior (P) and medial (M)). 2. The**

specimen was cut perpendicular to the resection surface in three sections for intra-operative assessment of the resection margins. Thereafter, a tissue section was chosen for the Raman experiment. 3. The Raman tissue section was inserted into a cartridge. The area to be measured was defined by the pathologist, containing tumor and >5 mm of surrounding healthy tissue, at least in one direction. 4. Raman mapping experiments were performed on a grid. The water concentration for each measured point was calculated. A two-dimensional image was obtained by using a nonlinear color scale to represent the water concentrations. 5. After Raman measurement, the specimen was routinely processed. H&E stained slide was made from the whole Raman tissue section within which pathologists identified the tissue area that was measured. The histopathological annotation of the tumor (T), healthy tissue (H) and of the tumor border (red line) was performed. 6. Based on the annotated tumor border in the H&E image (red line), the position of the adequate surgical margin (>5 mm of distance to the tumor border) was determined within the water map (green line).

After orienting and defining the resection margins, the pathologist and the surgeon surveyed all resection planes by visual inspection and palpation. After this, the pathologist cut the specimen in 3 - 5 cross sections (with a thickness of about 5 mm – 10 mm), perpendicular to the resection margin plane (Figure 1.2). For specimens comprising bone (i.e. mandibular resection specimens in patients with OSCC invading the bone) the soft tissue was cut till the bone. The pathologist measured the distance between tumor and resection surface. Often, this macroscopic assessment only was sufficient to decide on the further course of the operation without the need for frozen sections. In case of an unclear tumor border the pathologist may decide to further refine the information by microscopic examination of frozen sections.

Provided with this intra-operative information regarding inadequate margins the surgeon continues to harvest more tissue from the wound bed (e.g. immediate re-resection) to achieve an adequate surgical result.

After this intra-operative diagnostic procedure, one of the specimen cross sections was chosen for Raman experiments (further called “Raman tissue section”). The cross section was regarded suitable when containing tumor and >5 mm of healthy looking surrounding tissue (Figure 1.2). The remaining specimen cross sections were immersed in formalin.

Blood was rinsed from the Raman tissue section using physiological salt solution (0.9% NaCl) and gently patted dry with gauze. The area of interest (i.e. tumor and >5 mm of surrounding healthy tissue) was macroscopically chosen by the pathologist. The Raman tissue section was inserted in a closed cartridge to avoid drying of the tissue. The upper side of the cartridge consists of a fused silica window. This cartridge allows the scanning of a 3x3 cm tissue area. The Raman tissue section was placed in the cartridge with the surface to be measured in contact

with the fused silica window. Digital images of all handling steps were made, including images for the macroscopic representation of the tissue area measured (Figure 1.3).

After the experiment, the Raman tissue section was removed from the cartridge and immersed in formalin, together with the rest of the specimen to follow the routine procedure for final pathological processing.

### **Raman instrumentation and mapping experiments**

Raman ex-vivo mapping experiments were performed using a confocal Raman microscope (CRM), built in-house. The equipment was placed in a laboratory close to the operating room. The setup, as explained in our previous work (37), comprised a multichannel Raman Module (HPRM 2500, RiverD International B.V., The Netherlands), a 671nm laser (CrystaLaser, CL671-150-SO) and a charge-coupled device (CCD) camera fitted with a back-illuminated deep depletion CDD-chip (Andor iDus 401, DU401A BR-DD, Andor Technology Ltd., UK). A microscope (Leica DM RXA2, Leica Microsystems Wetzlar GmbH, Germany) and a computer-controlled sample stage (Leica DM STC) were coupled with the Raman Module. Eighty mW of laser light was focused in the tissue by means of a microscope objective (0.4 numerical aperture) with a free working distance of 1.1 mm (N PLAN 11566026, Leica Microsystems B.V., The Netherlands). The depth resolution was 40  $\mu\text{m}$ , experimentally determined. Spectral information was collected in the wavenumber range 2500 to 4000  $\text{cm}^{-1}$  with a resolution  $<5 \text{ cm}^{-1}$ .

For each measurement the cartridge with the tissue section was fixed on the microscope stage. The selected area was measured point-by-point using a grid. The grid cell size was between 300  $\mu\text{m}$  per 300  $\mu\text{m}$  to 1000  $\mu\text{m}$  per 1000  $\mu\text{m}$ , depending on the size of the tissue section and on the allowed time of 60 minutes to perform the experiment. In some cases, more than one map per specimen was measured depending on the size of the tissue section and on the allowed time. The acquisition time per spectrum was 1 second. Laser light was focused in the tissue at about 50  $\mu\text{m}$  below the fused silica window surface.

### **Calibration and processing of spectra**

All spectra were calibrated on the relative wavenumber axis and corrected for the wavelength dependent detection efficiency of the setup, according to instructions of the spectrometer supplier (RiverD International B.V., The Netherlands). Pre-processing of the spectral data was performed by removal of cosmic ray events and

subtraction of the signal background generated in the optical path of the setup itself (39). MATLAB R2014b was used for data processing and data visualization.

The tissue Raman spectra showed varying levels of background signal originating from tissue autofluorescence. For the calculation of tissue water concentrations, the autofluorescent background signal was estimated by a 3rd order polynomial and subtracted from the measured spectra.

Spectra with a relative intensity lower than 5% of the average intensity of all spectra measured from the sample were discarded. Intensity of the spectra was determined for the range 2700 to 3100  $\text{cm}^{-1}$  in which almost all spectral signatures from lipids and proteins are localized. Low signal intensities were encountered in cases where the tissue was locally not fully in contact with the measurement window.

The ratio of the Raman bands at 3390 $\text{cm}^{-1}$  and 2935 $\text{cm}^{-1}$  was used to determine the concentration of water per spectrum according to the method developed by Caspers et al. (2001) and described in detail in our previous study (38, 40).

### **Raman water maps**

Raman water maps were created by plotting the water concentration as a 2D map using pseudo colors to represent the water concentration range. A convolution of the water map with a 3x3 averaging filter was applied, as shown in figure 1.4, to obtain values that are more representative of the local water concentration (reducing noise in the image), and for better visualization of the difference in water concentration between tumor and the surgical margins (41).

### **Histopathology**

Histopathological evaluation of the measured areas was performed by two dedicated pathologists on routine hematoxylin and eosin (H&E) stained thin tissue sections. Subsequently, the H&E stained section was digitized, and the pathologists delineated healthy tissue, tumor and tumor border (Figure 1.5).

### **Data analysis**

Based on the projection of the tumor border in the H&E image (red line) onto the Raman water map, each pixel was labeled as either tumor border, tumor or healthy (Figure 1.6). The precision with which the individual pixels could be annotated in this way is limited by the much lower resolution of the Raman map compared to the microscopic image. The error was estimated to be half of the Raman map pixel-size. Thereafter, the minimal Euclidean distance between each Raman map pixel and the

tumor border was calculated. Based on these distances, the position of the adequate surgical margin (all pixels with distance  $>5$  mm to the tumor border) was obtained (Figure 1.6).

For each map, the average and standard deviation of the water concentration were separately calculated for tumor, for the inadequate margin (i.e. distance from tumor border  $\leq 5$  mm), and for the adequate margin.

The Mann-Whitney U-test was used to determine if the distribution of the water concentrations in tumor, in inadequate margins and in adequate margins are significantly different from each other.

Next, we calculated the average water concentration of the tissue as a function of the distance to the tumor border. This was done by calculating the mean water concentration of pixels falling within a 0.5 mm distance interval and moving this interval from -15 mm (inside the tumor) to + 10 mm (in the healthy tissue). Likewise, the standard deviation in the water concentration was calculated as function of distance to the tumor border.

## Results

Twenty-five ex-vivo Raman mapping experiments were performed on fresh resection specimens from 20 patients treated by surgery for OCSCC. Table 1, shows patient and tumor characteristics.

Each map had an average of 406 spectra (range comprehended between 97 to 1250 spectra), and an average area of  $240 \text{ mm}^2$  (from  $18.9$  to  $624 \text{ mm}^2$ ). The average tumor area per map was  $84 \text{ mm}^2$  (range was between  $13 \text{ mm}^2$  to  $390 \text{ mm}^2$ ), the average inadequate margin area per map was  $85 \text{ mm}^2$  (minimum value was  $27.9 \text{ mm}^2$  and maximum value was  $237 \text{ mm}^2$ ), and the average adequate margin area per map was  $71 \text{ mm}^2$  (minimum and maximum values were respectively  $4 \text{ mm}^2$  and  $379.2 \text{ mm}^2$ ).

In total, 3526 Raman spectra from tumor were obtained. From the surrounding healthy tissue, 3620 spectra were obtained at a distance of less than 5mm from the tumor border (i.e. within the area of inadequate margin) and 3001 spectra were obtained at a distance greater than 5mm from the tumor border (i.e. from the area of adequate margins).

As an example, the results for three experiments performed on fresh resection specimens from three patients are shown in figure 2. The macroscopic images of the measured areas are shown in column A. Column B shows the water concentration maps.

**Table 1. Patient and tumor characteristics. Number of maps measured per patient (Maps). Primary tumor location and pathological TNM classification (pTNM) of malignant tumors (42). Tumor size varied from less than 1cm (T1) to more than 4cm. In some patients, tumor had extended into the mandible (T4a). N-stage varied from no regional metastasis in lymph nodes to multiple lymph nodes with metastasis of 6cm or less in greatest dimension (N0-N2b). Distant metastasis was not encountered (M0).**

Patient	Age	Gender	Maps	Primary Tumor location	pTNM
1	71	F	1	Lateral side of tongue	T2N2bM0
2	72	M	1	Floor of mouth	T2N2bM0
3	52	F	1	Floor of mouth	T3N2bM0
4	52	F	1	Lateral side of tongue	T1N0M0
5	54	M	1	Lateral side of tongue	T1N0M0
6	42	M	1	Lateral side of tongue	T1N0M0
7	59	F	1	Lateral side of tongue	T2N0M0
8	91	M	2	Lateral side of tongue	T1N1M0
9	52	F	1	Lateral side of tongue	T1N0M0
10	42	F	1	Lateral side of tongue	T4aN2bM0
11	67	M	2	Inferior alveolar process	T4aN0M0
12	60	F	1	Lateral side of tongue	T1N0M0
13	69	M	2	Lateral side of tongue	T1N0M0
14	61	M	1	Lateral side of tongue	T1N0M0
15	68	M	1	Lateral side of tongue	T1N0M0
16	79	M	2	Lateral side of tongue	T1N0M0
17	68	M	2	Retromolar trigone	T4aN2bM0
18	72	F	1	Tongue and floor of the mouth	T3N1M0
19	58	M	1	Lateral side of tongue	T2N0M0
20	61	F	1	Lateral side of tongue	T2N0M0

These maps were interpolated to a pixel size of 300  $\mu\text{m}$ , which was the smallest step size used for mapping. In column C, the averaged water maps after interpolation to the same pixel size are presented. Column D shows the annotated H&E stained sections. Column E shows the average water concentration (blue line) and standard deviation (black line).

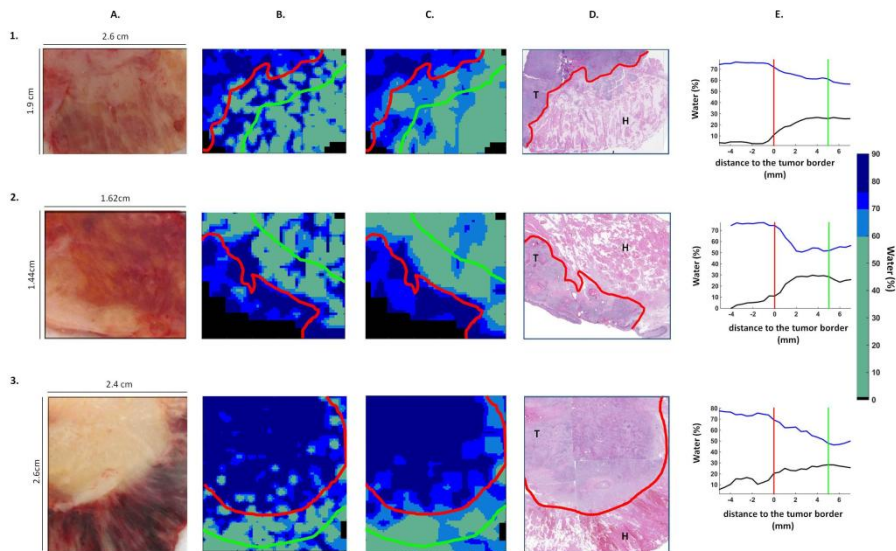


**Figure 2.** 1 – 3: Examples of the data obtained by means of mapping experiments on 3 Raman tissue sections from 3 patients. Panels column A: Photograph of the measured fresh tissue surface. Panels column B: Raman water map with indication of tumor border (red; based on final histopathology shown in panels of column D) and adequate surgical margin (green). Panels column C: Averaged Raman water map with indication of tumor border (red; based on final histopathology shown in panels of column D) and adequate surgical margin (green). Panels column D: H&E stained section obtained from the measured tissue surface, with tumor border (red), tumor (T), healthy surrounding tissue (H) indicated by pathologist. Panels column E: Graphs showing water concentration as function of the distance to the tumor border. Blue line: Average water concentration calculated per 0.5 mm distance interval. Black line: Standard deviation of the water concentration, per 0.5 mm distance interval. The red line at 0 mm represents the tumor border and the green line represents a distance of 5 mm from tumor border.

For each map the mean and standard deviation of the water concentration for tumor, inadequate and adequate margins were calculated (table 2). The average water concentration in tumor is  $76 \pm 8\%$ , in the inadequate margin it is  $59 \pm 24\%$ , and in the adequate margin it is  $54 \pm 24\%$ .

Mann-Whitney U-tests show that these difference in water concentration between tumor, inadequate margin, and adequate margin are all significantly different with p-values  $< 0.0001$ .

**Table 2 – Average water concentration and respective standard deviation for each map. The water concentration was calculated specifically for the tumor, inadequate margin and adequate margin. Maps were ordered according to the TNM classification of tumors (42).**

pTNM	Map	Patient	Concentration of water (%)					
			Tumor		Inadequate Margins		Adequate Margins	
			mean	std	Mean	std	Mean	std
T1N0M0	1	4	71	5	66	12	55	14
T1N0M0	2	5	71	5	65	20	62	19
T1N0M0	3	6	76	8	62	24	61	25
T1N0M0	4	12	76	6	54	28	58	24
T1N0M0	5	13	75	14	53	30	61	24
T1N0M0	6	13	76	11	49	30	57	31
T1N0M0	7	14	81	5	62	25	69	16
T1N0M0	8	15	77	4	66	21	61	26
T1N0M0	9	16	81	5	59	26	44	30
T1N0M0	10	16	77	12	57	26	43	32
T1N0M0	11	9	79	6	69	21	61	24
T1N1M0	12	8	73	10	55	26	46	33
T1N1M0	13	8	75	10	46	31	37	30
T2N0M0	14	7	78	5	60	24	55	24
T2N0M0	15	19	69	18	63	21	62	25
T2N0M0	16	20	81	3	70	23	62	24
T2N2bM0	17	1	80	9	65	25	55	30
T2N2bM0	18	2	76	6	54	20	60	22
T3N1M0	19	18	77	9	56	27	49	26
T3N2bM0	20	3	74	9	53	26	58	28
T4aN0M0	21	11	77	5	58	27	61	27
T4aN0M0	22	11	75	4	62	25	50	28
T4aN2bM0	23	10	76	8	64	18	42	21
T4aN2bM0	24	17	74	14	58	25	44	28
T4aN2bM0	25	17	75	13	52	27	43	27

In figure 3 the water concentration (blue line) is shown, calculated as the mean and standard deviation over all experiments, as a function of distance to the tumor border, using 0.5mm distance intervals. From the figure it is clear that, the water concentration in tumor is much higher than in the surrounding healthy tissue. The figure also shows that the drop-in water concentration coincides with the tumor border. The water concentration starts to decrease inside the tumor mass, close to the tumor border and continues to drop steeply until about 4 mm into the surrounding healthy tissue. From there the decline in water concentration continues with a

smaller gradient. Interestingly, the standard deviation in water concentration values also differs between tumor and surrounding healthy tissue; from less than 10% inside the tumor to more than 15% just outside the tumor.

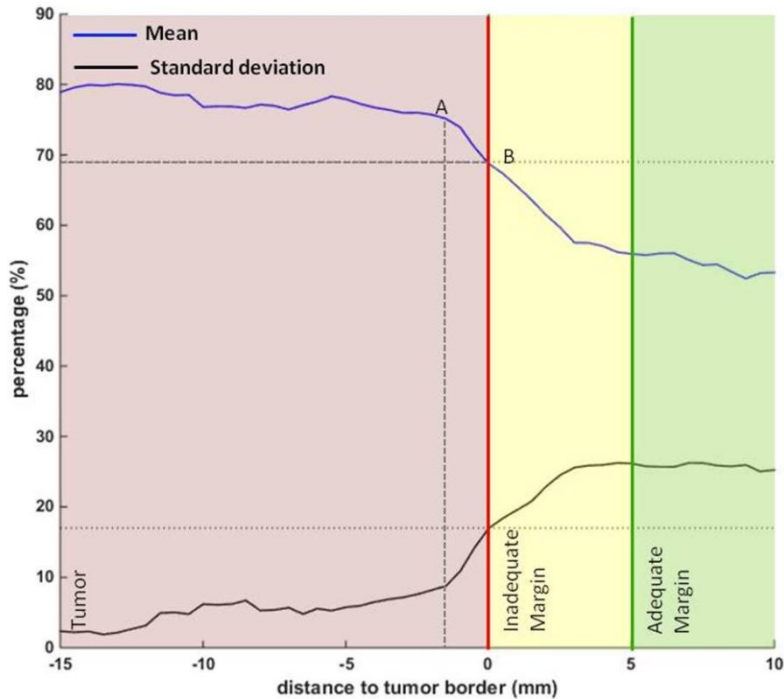


**Figure 3. Water concentration profile from inside the tumor towards adequate margin. All individual water concentration percentages of the 25 maps were averaged per interval to calculate the mean (blue) and standard deviation (black) of the water concentration as a function of the distance to the tumor border. The red line at 0 mm indicates the tumor border. The green line at 5 mm indicates the beginning of the adequate surgical margin.**

## Discussion

The aim of our research is the development of a clinical tool for intra-operative guidance of surgical-oncological procedures motivated by the main goal of surgery: adequate tumor resection and preservation of function and physical appearance. Of the many factors that affect the clinical outcome of patients with OSCC, only the resection margins, can be influenced by the surgeon and pathologist. The objective

intra-operative assessment of resection margins is the key to increase the number of adequate resections in surgical oncology, therefore, an objective tool for assessment and guidance is needed.

Multiple techniques are being explored for intra-operative use in surgical oncology (20-28). Until now, fluorescence spectroscopy (20), diffuse reflectance spectroscopy (21), elastic light spectroscopy (22), HRME (23) and OCT (24) have explored in-vivo delineation of the tumor at the mucosal surface, prior to surgery. However, eighty-seven percent of inadequate margins are found in the deeper (submucosal) soft tissue layers (43). Therefore, the design of these studies is not perfect to be applied at the submucosal layers of soft tissue, which is where the majority of inadequate margins are found.

OCT is a promising technique that has been used to investigate OCSCC resection margins. A recent study published by Hamdoon et al (2015) concluded that OCT is a valuable tool in the assessment of surgical margins. This study reported that the diagnostic accuracy was about 85%. However, they mentioned that the use of OCT-technology is limited, because the created image can be affected by the lack of normal tissue perfusion. Therefore, the resolution and contrast of the OCT images are influenced by the "ex-vivo nature" of the approach (44,45). Moreover, not only OCT but also HRME has as disadvantage that it requires complicated subjective image-interpretation (23,24,44,45).

Raman spectroscopy has proved to be a reliable technique that can be applied to assess mucosa as well as the deep soft tissue layers (31,36-38). This objective and non-destructive technique was used in our first study, where it showed to be accurate in discriminating OCSCC from the surrounding healthy tissue. In this previous study, we showed, by means of high-wavenumber Raman spectroscopy, that water concentration within the tumor (OCSCC) is significantly higher than in the surrounding healthy tissue enabling discrimination between tumor and healthy tissue with 98% accuracy (37). The notion that certain tumors contain more water than surrounding healthy tissue was not new; already in 1971 water content was described as one of the discriminators between tumor and healthy tissue. Diagnostic instruments like MRI use the differences in water between the relaxation times of normal and malignant tissues to generate contrast between the two (46).

In the current study, we investigated how the water concentration changes from inside the tumor towards the adequate surgical margin. The results show a clear correlation between the tumor border and the change in water concentration. The transition from a high-water concentration inside the tumor to a lower water concentration in the surrounding tissue takes place as a negative gradient over a

distance of about 4-6 mm across the border of the tumor. By analyzing this negative water concentration gradient (Figure 3) we observed that the decrease in water concentration from tumor towards the adequate margin is accompanied by an increase in the standard deviation of the water concentration, i.e. the heterogeneity increases. Inside the tumor, the water concentration was higher than 69%, with a relatively low standard deviation of less than 15%. This low standard deviation indicates that OCSCC is homogeneous concerning water concentration, regardless of pTNM classification (Table 2). Inside the tumor, at about 1.5 mm distance to the tumor border, the water concentration of the tumor starts to decrease, and the standard deviation starts to increase (Figure 3.A). The average precision with which the Raman image could be annotated with the image of the H&E-stained section was  $\pm 0.38$  mm (from  $\pm 0.15$  mm to  $\pm 0.5$  mm) and was determined by the resolution of the Raman measurements as explained in the materials and methods section. The increase in the standard deviation can indicate that close to the tumor border, the water concentration heterogeneity increases, possibly explained by the presence of stroma, blood vessels and lymphatic vessels (47). Another interesting finding is that at approximately 4 mm beyond the tumor border the standard deviation of the water concentration levels off at about 26%. This high variance of the water concentration in the surrounding healthy tissue is due to the heterogeneity in these areas comprising fat tissue, muscle (M) and vessels (Figure 4).

In this study we show the water concentration distribution across the tumor border. The shape of the water profile from inside the tumor towards the adequate margin for OCSCC is a new finding, as well as, the increase in water concentration heterogeneity at the tumor border.

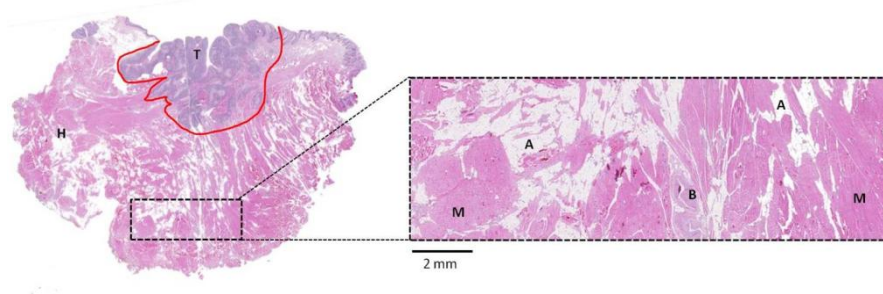


**Figure 4.** H&E stained section obtained from a measured tissue surface, with tumor border (red line), tumor (T) and healthy surrounding tissue (H) indicated by pathologist. A representative region of the adequate margin was enlarged and the tissue structures annotated. Tissue structures present are muscle (M), adipose tissue (A) and blood vessels (B).

We are currently devising fiber optic probe configurations and fiber optic probe measurement strategies to capture this information in a way that can be implemented for rapid intra-operative assessment of resection specimens.

We believe that Raman spectroscopy is a promising candidate for comprehensive intra-operative inspection of the surgical margins for OCSCC resection specimens, which will fit in the surgical workflow and can help to significantly improve the percentage of adequate resections.

We expect that water concentration analysis will be proof equally useful in localizing the tumor border in other locations of the body and plan to expand this line of investigation accordingly.

## References

1. Ferlay J., Soerjomataram I., Dikshit R., *GLOBOCAN 2012. International Journal of Cancer*. 2014;136: E359–E386.
2. Karim-Kos H. E., de Vries E., Soerjomataram I., *Eur. J. Cancer*. 2008;44:1345–89.
3. Guntinas-Lichius O., Wendt T., Buentzel J., *J Cancer Res Clin. Oncol*. 2010;136:55-63.
4. Sant M., Allemani C., Santaquilani M., *Eur J Cancer*. 2009;45:931–91.
5. Woolgar J. A., *Oral Oncol*. 2006;42:229–239.
6. Datema F. R., Ferrier M. B., van der Schroeff M. P., *Head & Neck*. 2009;32:728-736.
7. Baatenburg de Jong R. J., Hermans J., Molenaar J., *Head & Neck*. 2001;23:718-724.
8. Helliwell T., Woolgar J., *The Royal College of Pathologist*. 2013.
9. Smits R. W. H., Koljenović S., Hardillo J. A., *Head & Neck*. 2015; doi: 10.1002/hed.24075.
10. Dillon J. K., Brown C. B., McDonald T. M., *J Oral Maxillofac Surg*. 2015;73:1182-8.
11. Varvares M. A., Poti S., Kenyon B., *Laryngoscope*. 2015; doi: 10.1002/lary.25397.
12. Slootweg P. J., Hordijk G. J., Schade Y., *Oral Oncol*. 2002;38:500–503.
13. Al-Rajhi N., Khafaga Y., El-Husseiny J., *Oral Oncol*. 2000;36:508–514.
14. Binahmed A., Nason W. N., Abdoh A. A., *Oral Oncol*. 2007;43:780–784.
15. Pathak K. A., *Oral Surg Oral Med Oral Pathol Oral Radiol Endod*. 2009;107:235-239.
16. Gandour-Edwards R. F., Donald P. J., Wiese D. A., *Head & Neck*. 1993;15:33-8.
17. Hinni M. L., Ferlito A., Brandwein-Gensler M. S., *Head & Neck*. 2013; 35:1362–1370.
18. Yahalom R., Dobriyan A., Vered M., *J Surg Oncol*. 2008;98:572–578.
19. Chang A. M., Kim S. W., Duvvuri U., *Oral Oncol*. 2013;49:1077–1082.
20. Francisco A. L., *Oral Oncology*. 2014;50:593-599.
21. Stephen M. M., Jayanthi J. L., Unni N. G., *BMC Cancer*. 2013;13:278.
22. Sharwani A., *Oral Oncology*. 2006;42:343-349.
23. Vila P. M. *Ann Surg. Oncol*. 2013;19(11):3534-3539.
24. Lee A. M. D., *Biomedical Optics Express*. 2015;6(7):2664-2674.
25. Deshmukh A., *J Biomed Opt*. 2011;16:127004.
26. Ravi S. P., *J. of Clinical and Diagnostic Research*. 2014;8(9):ZE01-ZE05.

27. Keereweer S., Kerrebijn J. D. F., Mol I. M., *Head & Neck*. 2012;34:1002-1008.
28. Keereweer S., Mieog J. S. D., Mol I. M., *Archives of Otolaryngology - Head and Neck Surgery* 2011;137:609-615.
29. Malini R, *Biopolymers*. 2006;81:179-193.
30. Oliveira A. P., *Photomed Laser Surg*. 2006;24:348-353.
31. Su L., *Laser Phys*. 2012;22:311-316.
32. Nijssen A., Koljenović S., Schut T. C. B., *J Biophoton*. 2009;2:29-36.
33. Cals F. L. J. , Schut T. C. B., Hardillo J. A., *Laboratory Investigation*. 2015.
34. Bergholt M. S., Lin K., Zheng W., *J Biomed Opt*. 2012;17:077002.
35. Liu H., *Cancer Res*. 2012;72:2491-2500.
36. Barman I., *Cancer Res*. 2013;73:3206-3215.
37. Barroso E. M., Smits R. W. H., Bakker Schut T. C., *Anal. Chem*. 2015;87:2419-2426.
38. Wolthuis R., Van Aken M., Fountas K., *Anal. Chem*. 2001;73:3915-3920.
39. Wolthuis R., Bakker Schut T. C., Caspers P. J., *Fluorescent and Luminescent Probes for Biological Activity*. 1999;433-455.
40. Caspers P., *Journal of Investigative Dermatology*. 2001;116(3):434-442.
41. Haralick, Sternberg, and Zhuang, *IEEE Transactions on Pattern Analysis and Machine Intelligence*. 1987;PAMI-9:532-550.
42. Sobin L. H., Gospodarowicz M. K., Wittekind Ch., eds., International Union Against Cancer (UICC) TNM Classification of Malignant Tumors. 7th ed. Oxford, UK: Wiley-Blackwell; 2009.
43. Woolgar J. A., Triantafyllou A., *Oral Oncol*. 2005;41:1034-43.
44. Hamdoon Z., Jerjes W., McKenzie G., *Photodiagnosis and Photodynamic Therapy*. 2016;13:211-217.
45. Jung W., Boppart S. A., *Anal Cell Pathol*. 2012;35(3):129-143.
46. Damadian R., *Science*. 1971;171:1151-1153.
47. Wenig B. M., *Modern Pathology*. 2002;15(3):229-254.



## ***CHAPTER 6***

### ***Raman spectroscopy for assessment of bone resection margins in mandibulectomy for oral cavity squamous cell carcinoma***

E. M. Barroso<sup>†</sup>, I. ten Hove<sup>†</sup>, T. C. Bakker Schut, H. Mast, C. G. F. van Lanschot, R. W. H. Smits, P. J. Caspers, R. Verdijk, V. Noordhoek Hegt, R. J. Baatenburg de Jong, E. B. Wolvius, G. J. Puppels, S. Koljenović

<sup>†</sup> These authors contributed equally to this work.

**European Journal of Cancer 2018; 92:77-87**



## Abstract

The aim of this study was to investigate the potential of Raman spectroscopy for detection of oral cavity squamous cell carcinoma (OCSCC) in bone resection surfaces during mandibulectomy.

Raman mapping experiments were performed on fresh mandible resection specimens from patients treated with mandibulectomy for OCSCC. A tumor detection algorithm was created based on water concentration and the high-wavenumber range (2800  $\text{cm}^{-1}$  to 3050  $\text{cm}^{-1}$ ) of the Raman spectra.

Twenty-six *ex-vivo* Raman mapping experiments were performed on 26 fresh mandible resection specimens obtained from 22 patients.

The algorithm was applied on an independent test set and showed an accuracy of 95%, a sensitivity of 95%, and a specificity of 87%.

These results form the basis for further development of a Raman spectroscopy tool as an objective method for intra-operative assessment of bone resection margins.

## Introduction

Oral cavity squamous cell carcinoma (OCSCC) is the most frequent type of cancer in the head and neck region. The 5-year survival is around 50% (1,2). Every year, 145.000 deaths are registered worldwide (3,4).

The primary treatment for OCSCC is surgery aiming at complete removal of tumor with an adequate resection margin (5,6). During the operation, the surgeon decides where to cut based on preoperative imaging (CT, MRI), visual inspection and palpation of the tumor and surrounding tissues.

For OCSCC surgery, results obtained from two Dutch centers (Erasmus MC, University Medical Center Rotterdam and Leiden University Medical Center) showed inadequate soft tissue resection margins in about 85% of the cases (7). Similar results were reported by the Harborview Medical Center and the University of Washington Medical Center in Seattle (USA) (8). With respect to bone resection margins, studies have reported tumor-positive bone resections in 2-20% of the cases (9-12). Additionally, a retrospective study performed by our group showed that tumor-positive bone resection margins were found in 21% of the patients (13).

Adequate resection margins are paramount for disease control and survival: a number of studies have shown that 5-year disease-free survival decreases significantly when the margins are inadequate (7,9,14-19). Ideally, all resection margins (soft- and bone tissue) should be controlled by intra-operative assessment. This would enable additional resection during the same surgical setting to ensure adequate tumor resection and a tumor-free wound bed for tissue transplants.

For soft tissue resection margins the so-called frozen section procedure is available for intra-operative assessment (20-24). The surgeon samples a piece of suspicious tissue from the wound-bed and submits it for microscopic evaluation by the pathologist.

In contrast to soft tissue, for bone resection margins the assessment by frozen sections is virtually impossible (25-29), while histopathological information on the presence of tumor or free of tumor in the bone margins is available only after a few weeks (7).

The resection of advanced OCSCC with mandible involvement requires immediate reconstruction with microvascular free flaps. By that time the wound is healed, which makes a second surgery undesirable (25-29). Therefore, current histopathology does not contribute to more radical resections. During surgery, other than visual inspection, there is no routine intra-operative technique to evaluate the bone resection margins.

Recently, Nieberler et al. (2014, 2016) showed that intra-operative cytological assessment of bone resection margins can be used. This intra-operative approach was established and validated to assess bone specimens, including the inferior alveolar nerve. The technique revealed a sensitivity of 94.4%, a specificity of 97.4%, a positive predictive value of 85% and a negative predictive value of 99.1%. Although these results are very promising, this approach is not widely used. The authors mention a number of limitations of the technique. Desiccation of the bone margin caused altered cell morphologies, which led not only to false-positive results but also to false-negative results. Additionally, the authors mention that insufficient cellular material or excessive trabecular bone material and the interference by blood cells resulted in low quality cytological preparations (28,29).

The use of Raman spectroscopy for intra-operative assessment of tumor resection margins is currently being investigated (30-32). This optical technique is based on inelastic scattering of light by the molecules in the tissue and provides detailed quantitative and qualitative information about its molecular composition (30-34). The technique can be used directly on tissue because it is non-destructive and there is no need for reagents or labeling (30-41).

In earlier work we showed that Raman spectroscopy can be used to discriminate OCSCC from surrounding healthy soft tissue with a sensitivity of 99% and a specificity of 92%, based on clear differences in tissue water concentration. The water concentration was found to be significantly higher in the tumor than in the surrounding healthy soft tissue (35). Furthermore, we demonstrated that the tumor border could be determined based on water concentration. The water concentration decreases from 76% ( $\pm 8\%$ ) inside the tumor to 54% ( $\pm 24\%$ ) at a distance of 5 mm from the tumor border, corresponding to the targeted tumor free margin in OCSCC resections (36).

The goal of the current study was to investigate whether Raman spectroscopy can also be used to detect OCSCC in bone resection surfaces enabling surgeons and pathologists to use it as an objective intra-operative technique for assessment of the bone resection margins.

## Materials and Methods

### Medical Ethical Approval

This study was approved by the Medical Ethics Committee of the Erasmus MC, University Medical Center Rotterdam (MEC-2013-345). Before the surgical procedure, informed consent was obtained from all patients. Between October 2014 and July 2016 experiments were performed on fresh resection specimens of patients undergoing mandibulectomy for OCSCC. The time for the Raman experiments was limited to 60 minutes for optimal preservation of the tissue.

### Handling of resection specimen

After the resection, the pathologist and the surgeon examined the specimen together.

This examination comprised of recording the anatomical orientation of the specimen with drawings and photographs (Figure 1.a). Subsequently, the pathologist together with the surgeon examined all resection planes by visual inspection and palpation.

After this assessment, without compromising the histopathological process, cross sections were taken from one or both mandible resection edges and from the center of the specimen (containing tumor) (Figure 1.a-e). The bone sections had a thickness of 5 mm. The complete bone resection surface was macroscopically inspected by the pathologist and surgeon. Regions within the resection surfaces were selected for

Raman measurements that either appeared to contain tumor, or, as controls, appeared to be free of tumor.

Prior to Raman experiments the bone sections were rinsed with physiological salt solution (0.9% NaCl) and then gently patted dry with gauze. The bone section was placed in a cartridge with the surface to be measured in contact with a fused silica window (Figure 1.b-c). After the Raman experiments measurements, the specimen followed the routine procedure for final histopathological processing. An overview of the handling protocol of a mandible specimen is illustrated in Figure 1.

### **Raman instrumentation and mapping**

A confocal Raman microscope was used to perform Raman mapping experiments. The equipment is described in detail in earlier work (36). It comprises a 671nm laser (CrystaLaser, CL671-150-SO), a multichannel Raman Module (HPRM 2500, RiverD International B.V) and a charge-coupled device (CCD) camera fitted with a back-illuminated deep depletion CDD-chip (Andor iDus 401, DU401A BR-DD, Andor Technology Ltd.). The Raman Module was coupled to a microscope (Leica DM RXA2, Leica Microsystems Wetzlar GmbH) and a computer-controlled sample stage (Leica DM STC). By means of a microscope objective with 0.4 numerical aperture and 1.1mm working distance (N PLAN 11566026, Leica Microsystems B.V.) 80mW of laser light was focused in the bone tissue. Spectral information was collected in the high-wavenumber range of 2500 to 4000  $\text{cm}^{-1}$  with a resolution  $<5\text{cm}^{-1}$ .

The depth resolution was 40 $\mu\text{m}$ . The laser light was focused in bone at about 70 $\mu\text{m}$  below the fused silica window of the cartridge. The cartridge was then fixed on the microscope stage and a selected surface area was mapped in a grid. The step size of the grid varied between 250 $\mu\text{m}$  by 250 $\mu\text{m}$  to 1000 $\mu\text{m}$  by 1000 $\mu\text{m}$  depending on the size of the bone section. The signal acquisition time per spectrum was 1 second. Each mapping experiment was performed in less than 30 minutes.

### **Calibration and pre-processing of spectra**

For data calibration and data pre-processing software was developed with MATLAB (R2014b).

Spectra were calibrated on the relative wavenumber axis and corrected for the wavelength dependent detection efficiency of the setup (37).

The background signal due to tissue auto fluorescence was estimated using a method based on the multiple regression (42). The background was estimated as a 3rd order polynomial and subtracted from the pre-processed spectra.

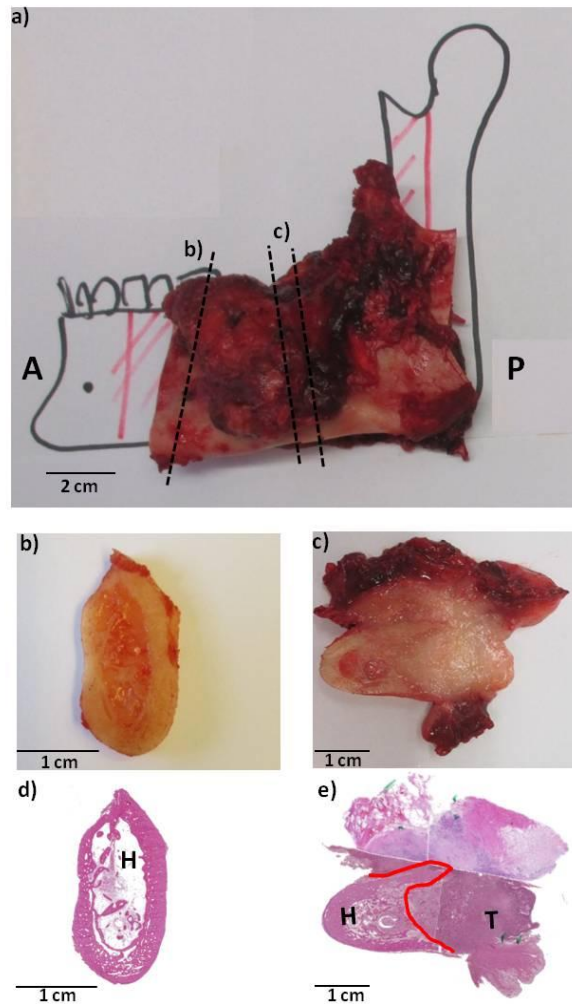


**Figure 1.** Overview of the handling protocol of a segmental mandibulectomy specimen. a) Specimen with recorded anatomical orientation (A for anterior and P for posterior). b) Section inserted in the cartridge. This section is from the edge of the specimen (without macroscopically visible tumor). c) Section inserted in the cartridge. This section is from the center of the specimen with the tumor invading the bone. d) Close up of the tissue section shown in b. e) Close up of the tissue section shown in c. f) H&E stained section obtained from the bone section b. g) H&E stained section obtained from the bone

**section c. Healthy tissue (H) and tumor (T) are indicated. The red line demarcates the border between the tumor and healthy bone.**

For all spectra, the average intensity over the range of 2700 to 3100  $\text{cm}^{-1}$  was used as a measure of signal intensity. The lowest quality spectra (with an average intensity lower than 5% of the overall average intensity) were excluded from the data analysis.

## **Histopathological annotation**

Histopathological annotation of tumor and healthy tissue in bone resection specimen, based on H&E stained sections, was performed by a dedicated pathologist (Figure 1. f-g).

## **Spectral Analysis**

Data processing and data analysis was also performed in MATLAB; R2014b. Data analysis consisted of two steps: 1) analysis of the water concentration and 2) analysis of the C-H stretching region by performing principal component analysis (PCA) and linear discriminant analysis (LDA).

### *1) Analysis of the water concentration*

The water concentration in bone resection specimen was calculated for each measurement point according to the method developed by Caspers et al. (2001) and described in detail elsewhere (33-35).

Raman water maps of the bone sections were created, using a color code to represent the water concentration range. The images of the H&E stained sections were projected onto the corresponding Raman water maps. This allowed histopathological annotation of each pixel as tumor, tumor border, or healthy bone.

Additionally, for each Raman pixel the minimal Euclidean distance to the closest pixel belonging to the tumor border was calculated. The precision of the annotation of the individual pixels was limited by the resolution of the respective Raman water map (pixel size varying from 250  $\mu\text{m}$  by 250  $\mu\text{m}$  to 1000  $\mu\text{m}$  by 1000  $\mu\text{m}$ ).

After calculation of the water concentrations and histopathological annotation of the Raman water maps, the water concentrations were separated in two groups: water concentrations from samples only containing healthy bone (referred to as H-group), and water concentrations from bone containing tumor (referred as T-group). For the

T-group we only considered the spectra from the tumor region that were  $>3$  mm away from the tumor border to ensure that only pure tumor spectra were analyzed.

The Mann-Whitney u-test was used to determine if there was a significant difference between the water concentrations measured in tumor and the water concentrations measured in healthy bone.

The discriminatory power of the water concentration analysis was determined using a Receiver Operating Characteristic (ROC) curve. The ROC curve was obtained by calculating the number of correct and incorrect classifications as function of the water concentration cut-off value used to discriminate between the T-group and the H-group. The water concentration percentage that discriminated the two groups with a sensitivity of 99% was used as a cut-off value in order to minimize the risk of misclassifying tumor as healthy tissue. Spectra with water concentrations lower than the cut-off were indicated as negative (bone without tumor). Spectra with water concentrations higher than this cut-off were indicated as positive (i.e. potentially tumor) and were further processed in step 2.

## 2) Analysis of the C-H stretching region: PCA-LDA modeling

The spectral region between  $2800$  and  $3050\text{ cm}^{-1}$  was used for analysis of the C-H stretching Raman signal. The information obtained in this region is independent from, and complementary to, the water concentration information.

First, all spectra were scaled using an extended multiplicative scatter correction (EMSC) procedure to eliminate the spectral interference of varying water contributions. This method has been used in earlier studies and in this study was used to ensure that the C-H stretching region analysis is independent from the water signal (40,43). After, PCA was performed to reduce the dimensionality of data prior to LDA modeling. The scores on the most significant principal components (determined by the highest confidence levels in a student t-test of group differences) were selected as input parameters to the LDA. LDA finds the direction in this PCA space that maximizes the ratio between inter-group and intra-group variance (44,45). The LDA discriminant score was used for classification. The discriminating parameter used as input for the LDA was a Boolean: tumor or non-tumor.

## **Classification algorithm for detection of OCSCC in the bone**

An algorithm for detection of OCSCC in the bone was developed by combining the two previous analyses: 1) analysis of the water concentration and 2) PCA-LDA analysis of the C-H stretching region.

After algorithm development, an independent data set was used for validation of the algorithm. Sixty-eight percent of the maps served for algorithm development, 32% of the maps were used as independent data set.

### *Algorithm development*

The water concentration was calculated per spectrum (step 1). Only the spectra that yielded a water concentration higher than the cut-off were subjected to the PCA-LDA model, labeled as suspicious of being tumor (step 2). Spectra with a water concentration lower than the cut-off were classified with a zero score (labeled as bone without tumor).

The LDA discriminant score, obtained in step 2, was used for classification of the spectra with water concentrations higher than the cut-off, calculated in step 1).

The discriminative power of this sequential model was determined by calculating the area under the curve (AUC) of the ROC curve that was generated by evaluating the leave one patient out prediction results for different discrimination threshold levels.

The Youden Index was determined to find the cut-off level that best discriminates between the two groups (highest combined sensitivity and specificity) (46). This Youden index was used as the cut-off for the tumor detection algorithm.

### *Algorithm Validation*

The tumor detection algorithm was tested on an independent data set, consisting of data obtained from tissue samples of patients that were not included in the data set used to create the classification model. The sensitivity and specificity of the algorithm were calculated.

Due to the relatively large pixel-size in the Raman maps, the pixels on the tumor border could not be annotated as tumor or healthy. They were annotated as tumor border and were excluded from the test of the classification model.

## Results

Twenty-six ex-vivo Raman mapping experiments were performed on fresh mandible resection specimens from 22 patients treated with mandibulectomy for OCSCC. Patient and tumor characteristics are listed in the table 1.

**Table 1 - Patient and tumor characteristics.**

Patient	Age	Gender	Tumor	cTNM
1	70	M	tongue	T4N0M0
2	67	F	floor of	T1N0M0
3	86	F	mandible	T4N0M0
4	66	M	floor of	T4aN0M
5	68	M	floor of	T4N0M0
6	87	F	mandible	T4aN0M
7	69	M	mandible	T4aN0M
8	52	M	mandible	T4aN2c
9	67	F	floor of	T2N0M0
10	73	M	mandible	T4aN2b
11	73	M	mandible	T4aN0M
12	78	M	mandible	T4aN0M
13	66	M	mandible	T4N0M0
14	84	F	mandible	T4N2cM
15	54	M	mandible	T4aN2c
16	69	M	mandible	T4aN2c
17	81	M	floor of	T4aN0M
18	60	M	lower lip	rT0N3M
19	59	F	floor of	rT4aN0
20	56	F	buccal	T4N0M0
21	61	F	mandible	T4aN0M
22	64	M	floor of	T4aN0M

\* Mandibulectomy (marginal) performed for reconstruction reasons.

# Mandibulectomy (segmental) performed because of large lymph node metastasis with extra nodal spread and extensive bone invasion.

Of these 26 maps, 17 maps (from 15 patients) were used for development of the tumor detection algorithm and final classification model (training set). The remaining 9 maps (from 7 different patients) were used for validation of the model (test set).

The maps of the training set consisted on average of 423 spectra (ranging from 122 to 727 spectra) and measured an average area of 128.7mm<sup>2</sup> (ranging from 43.7 to 253 mm<sup>2</sup>). Seven Raman maps were obtained of bone sections containing tumor and

surrounding healthy bone (T-group, 7 patients), 10 Raman maps were obtained of patient's samples containing only healthy bone (H-group, 8 patients). Figure 2 shows examples of the Raman sections that were measured. The bone section shown in figure 2.a consisted of healthy tissue and the bone section shown in figure 2.b was invaded by tumor. The Raman spectrum in figure 2.c was obtained from the healthy bone tissue and the Raman spectrum in figure 2.d was obtained of tumor. Figures 2.e and 2.f show the tissue sections after H&E staining.

## Spectral Analysis

### *1) Analysis of the water concentration*

For the T-group, water concentrations were calculated from 1008 tumor spectra that were recorded at >3 mm distance from the tumor border. The distribution of water concentrations is shown in figure 3.a (orange). The mean of the water concentrations of the T-group was 77% with a standard deviation of 6%.

For the H-group, a total of 4983 spectra were measured and were used to calculate water concentrations in the healthy bone tissue. The distribution of the water concentration in the H-group is also shown in figure 3.a (green). The H-group had a mean water concentration of 44% with a standard deviation of 17%.

The Mann-Whitney U-test showed a significant difference between the water concentrations from the H-group and the T-group (p-value <0.0001).

A ROC-curve was generated based on the water concentrations measured in both groups, in which the true positive rate (sensitivity) was plotted against the false positive rate (1-specificity) for different values of the water concentration threshold (Figure 3.b). The area under the curve, which is a measure for the discriminatory power of the test, was 0.96. Using a cut-off value of 60% for the water concentration, a sensitivity of 99% is obtained for the detection of tumor suspicious tissue, with a specificity of 83%.

### *2) Analysis of the C-H stretching region*

For analysis of the spectral region containing C-H vibrations only the spectra from the T-group and from the H-group that showed a water concentration >60% (cut-off) were included (712 spectra from the H-group, and 1002 spectra from the T-group). The mean spectra of the two groups and their difference are shown in figure 3.c. The difference spectrum shows that the lipid to protein ratio in tumor tissue is higher than in healthy bone. The wavenumber region 2830 to 3020  $\text{cm}^{-1}$  was used for PCA-

LDA modeling because it contained the largest differences between the mean spectra from the two groups.

The first 4 principal components were used as input in the LDA modeling.

### Classification model for detection of OCSCC in the bone

#### Model development

The two-step tumor detection algorithm described above was used to develop the final classification model.

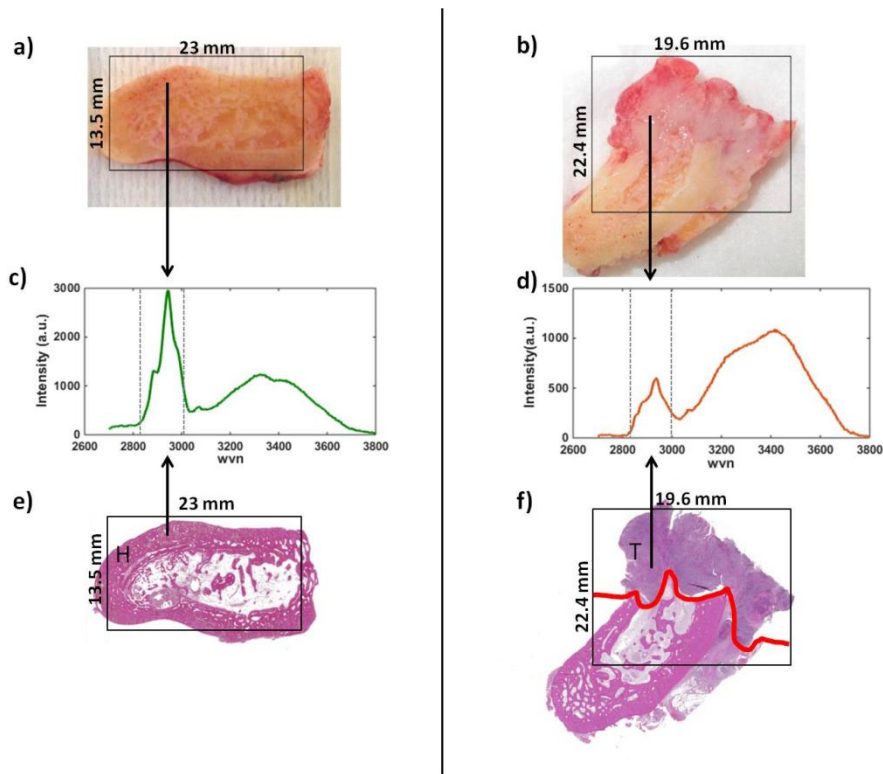


**Figure 2.** Examples of fresh mandibulectomy sections of healthy cortical bone and bone invaded by tumor, with their characteristic Raman spectra and H&E images. a) Bone section from the edge of a mandible specimen, without tumor. b) Bone slice from the center of the specimen, where tumor is invading the bone. c) Spectrum acquired from the cortical region of the mandible (acquisition time: 1 second). d) Spectrum from tumor

tissue that was >3mm distant from the tumor border (acquisition time: 1 second). The two-dashed vertical gray lines are marking the CH-stretching region. e) H&E stained section obtained from the bone section a. f) H&E stained section obtained from the section b. **Histopathological annotation: H for healthy bone and T for tumor. The tumor border is delineated with a red line.**

All spectra (5991) from the training set were used for development of this model.

The ROC-curve shown in figure 3.d is the result of a leave-one-patient-out evaluation (cross validation per spectrum) of the classification model (combination of the water concentration analysis and the PCA-LDA model). It shows a discriminatory power of 98%.

The LDA discrimination threshold that gave the highest combined sensitivity and specificity (Youden index) yielded a sensitivity of 94%, and a specificity of 93%. The threshold was used in the final classification model.

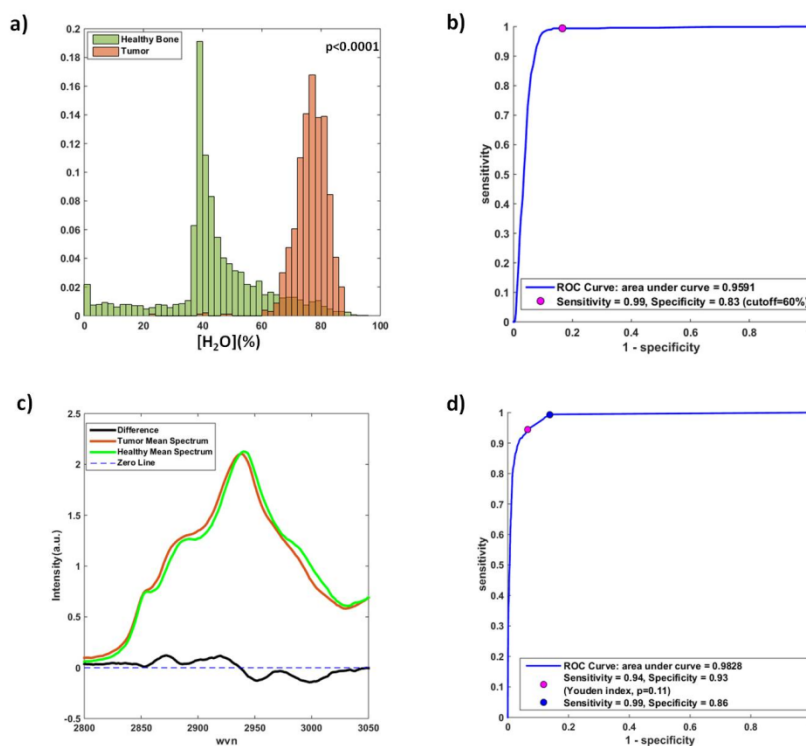


**Figure 3. Results of the spectral analysis and leave one patient out cross validation. a) Histogram of the normalized distributions of the water concentration for the tumor group (T-group, orange), and for the healthy bone group (H-group, green). b) ROC**

curve generated (AUC of 0.96) to show the discriminating power of the water concentration model (sensitivity of 99% and specificity of 83% for water concentrations >60%). c) Mean spectrum of the T-group with a water concentration of >60% (orange), and the mean spectrum of H-group with a water concentration of ≤60% (green). The difference spectrum (tumor minus healthy) is shown in black. d) ROC curve generated (AUC of 0.98) to demonstrate the discriminatory power of the tumor detection algorithm (sensitivity of 94% and specificity of 93%).

### *Model validation*

The independent test set consisted of 2033 spectra from 9 maps (from 7 patients). The average number of spectra per map was 226 (range from 110 to 509 spectra), from an average area of 74.4 mm<sup>2</sup> (range from 27.5 to 147 mm<sup>2</sup>).

The validation of the tumor detection algorithm (on the independent test set) using the discrimination threshold based on the Youden index, showed a sensitivity of 95%, a specificity of 87%, and an accuracy of 95%. The results of the validation of the tumor detection model are presented in table 2 and illustrated in figure 4 with the prediction maps of the tumor detection algorithm (column b).

**Table 2 – Comparison of false positive rates\* obtained in bone cross sections containing tumor and bone cross sections without tumor.**

Map number	False Positive rate (%)	Histopathology
1	15	Bone section with tumor
2	15	Bone section with tumor
3	68	Bone section with tumor
4	0.2	<b>Bone section without tumor</b>
5	1.3	<b>Bone section without tumor</b>
6	4	<b>Bone section without tumor</b>
7	7.2	<b>Bone section without tumor</b>
8	1.3	<b>Bone section without tumor</b>
9	0	<b>Bone section without tumor</b>

\* False positive rate is the proportion of pixels from healthy tissue that are misclassified as tumor.

## **Discussion**

In contrast to OCSCC soft tissue specimens in which the resection margins can be assessed by frozen sections during the operation, there is no standard technique than can be used intra-operatively for evaluation of bone resection margins for OCSCC.

A study published by Nieberler et al. (2016) demonstrated the benefits of cytological intra-operative assessment of the bone resection margins in head and neck carcinoma. They concluded that the intra-operative assessment can lead to a reduction of the residual carcinoma tissue in the bone resections margins from 17% to 7.8% (29). Although these results are very promising, a major disadvantage of the technique is that the analysis is mainly based on cells obtained from the bone marrow. This cytological sample preparation is difficult, the assessment is subjective, labor intensive, and requires the availability of highly trained professionals.

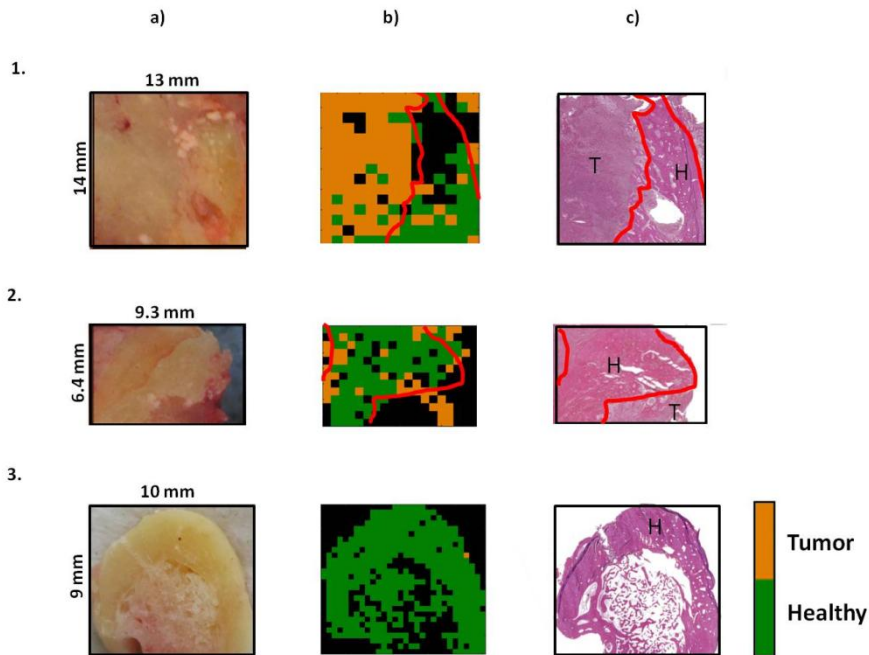


**Figure 4.** Examples of the results obtained when testing the tissue classification model on 3 bone slices from 3 patients (1-3). a) Photographs of fresh bone cross sections from the center of resection specimen with tumor invasion (based on radiologic examination) from which Raman spectra were obtained. b) Raman classification maps (orange: tumor, green: healthy bone) tumor border indicated in red. Black pixels correspond to absence of tissue or to spectra with low Raman signal quality. c) H&E-stained sections obtained from the measured bone surface, with tumor border (red), tumor (T) and healthy surrounding bone (H) indicated by pathologist.

In contrast to cytological assessment described by Nieberler et al. (2014, 2016), Raman spectroscopy based method is objective, does not require sample preparation and enables quick evaluation of whole bone resection surface.

Since 2014, our group has been focused on applying high-wavenumber Raman spectroscopy for surgery guidance by intra-operative assessment of resection margins on OCSCC specimens (35).

By using this technique, we found that we could differentiate OCSCC from surrounding healthy tissue based on water concentration with an accuracy of 98% (35). Recently, we have demonstrated that high-wavenumber Raman spectroscopy can be used in soft tissue specimens to locate the tumor border (36). The final aim of our research is the development of a clinical tool for ex-vivo and in-vivo real-time assessment of the soft and bone resection margins motivated by the main goal of surgery: adequate tumor resection while sparing as much healthy tissue as possible.

The current ex-vivo study shows that the average water concentration found in tumor located in the bone was  $77\% \pm 6\%$ . This value is similar to the results found in tumor located in the soft tissue in a previous study (36). The average water concentration of healthy bone is 44%, which is lower than in healthy soft tissue (54%) (36). A large standard deviation in water concentration was found for healthy bone (17%), just as we found previously for healthy soft tissue (24%) (36).

A two-step classification model was developed based on the water concentration information and the spectral information in the CH-stretching region. The model showed an accuracy of 95%, a specificity of 87% and a sensitivity of 95% when tested on an independent data-set.

A further analysis of the false positive results (table 2) showed that most misclassifications occurred in bone sections containing tumor where histopathologically normal tissue in the proximity of tumor was classified as tumor (average false positive rate of 33%). This may be explained by epithelial-mesenchymal transition (EMT), which is recognized as an initiating mechanism of the invasive and metastatic behavior of epithelial cancers (47). Therefore, EMT may be biochemically more similar to tumor than to healthy bone, which explains false positives in the bone sections containing tumor and healthy-looking tissue (table 2). This is also supported by the fact that, in bone sections without tumor (and without EMT) the average false positive rate was much lower (2.3% in average). Marro et al. (2014) showed that Raman spectroscopy can be used for molecular monitoring of epithelial mesenchymal transition in breast cancer cells (48).

For implementation of this technique for clinical decision making regarding the need for additional bone resection, a first approach could be to use the false positive rate encountered in bone sections without tumor as a threshold below which a tissue section is classified as tumor free. This as well as more elaborate approaches will be the subject of further studies.

These results convincingly show that Raman spectra of bone resection specimen provide the information to distinguish between healthy tissue and remaining tumor tissue.

Implementation in the clinical workflow also requires the elimination of a practical issue that sometimes occurred. A lack of contact between the surface of the bone section and the fused silica window of the measurement cartridge leads to a low-quality Raman signal. Therefore, it is important to cut the bone in a manner that it results in a flat and smooth surface. Alternatively, a method can be implemented by which the contours of the surface are automatically followed by the measurement system (such as, inVia<sup>TM</sup>Qontor<sup>TM</sup>, Renishaw B.V., United Kingdom).

In this study, regions within bone resection surfaces were selected that either appeared to the surgeon and pathologist to contain tumor, or, as controls, appeared to be free of tumor. Of course, the aim for the future is to scan the complete resection surface by Raman spectroscopy.

Our results show, that Raman spectroscopy could be applied ex-vivo for evaluation of bone resection margins (including bone marrow and cortical bone) during OCSCC surgery. We believe that this could improve the number of adequate resection margins, and consequently reduce the extent of adjuvant treatment. Equally important, having a method for intra-operative assessment of bone resection margins, might give surgeons the confidence to adjust initial cut line and resect the bone closer to the suspected tumor border. In this way, healthy bone might be spared, which will positively influence the reconstruction and reduce the possible post-operative complications.

## References

1. Datema F. R., Ferrier M. B., Vergouwe Y., *Head & Neck*. 2013;35(9):1232-7.
2. van der Ploeg T., Datema F., Baatenburg de Jong R., *PLoS One*. 2014;9(6):e100234.
3. Ferlay J., Soerjomataram I., Dikshit R., *International Journal of Cancer*. 2014;136:E359–E386.
4. Karim-Kos H. E., de Vries E., Soerjomataram I., *Eur. J. Cancer*. 2008;44:1345–89.
5. Ord R. A., Aisner S., *J Oral Maxillofac Surg*. 1997;55:663-9; discussion 669-71.
6. Chen P. Y., Chen H. H., Hsiao J. R., *Oral Oncol*. 2007;43:780-4.
7. Helliwell T., Woolgar J., *The Royal College of Pathologists*. 2013.
8. Varvares M. A., Poti S., Kenyon B., *Laryngoscope*. 2015; doi: 10.1002/lary.25397.
9. Binahmed A., Nason R.W., Abdoh A.A., *Oral Oncol*. 2007;43:780–4.
10. Schusterman M. A., Harris S. W., Raymond A. K., *Head & Neck*. 1993;15:204-207.
11. Brown J. S., Kalavrezos N., D'Souza J., *British Journal of Oral and Maxillofacial Surgery*. 2002;40:275-284.
12. Bilodeau E. A. and Chiose S., *Head and Neck Pathology*. 2011;5:2016-220.
13. Smits R. W. H., ten Hove I., Koljenović S., *Journal of Oral & Maxillofacial Surgery*. Submitted 2018 and under revision.
14. Loree T. R., Strong E.W., *Am J Surg*. 1990;160:410–4.
15. Smits R. W. H., Koljenović S., Hardillo J. A., *Head & Neck*. 2015; doi: 10.1002/hed.24075.
16. Dillon J. K., Brown C. B., McDonald T. M., *J Oral Maxillofac Surg*. 2015;73:1182-8.
17. Hinni M. L., Ferlito A., Brandwein-Gensler M. S., *Head & Neck*. 2013;35:1362–70.
18. Slootweg P. J., Hordijk G. J., Schade Y., *Oral Oncol*. 2002;38:500–503.
19. Al-Rajhi N., Khafaga Y., El-Husseiny J., *Oral Oncol*. 2000;36:508–514.
20. Gokavapura S., Rao L. M. C., Mahajan M., *British Journal of Oral and Maxillofacial Surgery* 2015;(53):875-879.
21. Byers R. M., Bland K. I., Borlase B., *Am J Surg*. 1978;136:525-8.
22. Williams D. W., *Curr Oncol Rep*. 2016;18:54.
23. Smits R. W. H., Noordhoek Hegt V., Verdijk R., *To be submitted soon*.
24. McIntosh E. R., Harada S., Drwiega J., *Annals of Diagnostic Pathology*. 2015;19:326-329.
25. Maciejewski A., Szymczyk C., *J Reconstr Microsurg*. 2007;23:1-10.

26. Holzle F., Kesting M. R., Holzle G., *Int J Oral Maxillofac Surg.* 2007;36:802-6.
27. Markowitz B. L., Calcaterra T. C., *Clin Plast Surg.* 1994;21:9-14.
28. Nieberler M., Häusler P., Drecoll E., *Cancer Cytopathology.* 2014;122:646-56.
29. Nieberler M., Häußler P., Kesting M. R., *Ann Surg Oncol.* 2016.
30. Nijssen A., Koljenović S., Schut TCB., *J Biophoton.* 2009;2:29-36.
31. Liu H., *Cancer Res.* 2012;72:2491-2500.
32. Barman I., Dingari N. C., Saha A., *Cancer Res.* 2013;73:3206-3215.
33. Wolthuis R., Van Aken M., Fountas K., *Anal. Chem.* 2001;73:3915-3920.
34. Caspers P. J., *Journal of Investigative Dermatology.* 2001;116(3):434-442.
35. Barroso E. M., Smits R. W. H., Bakker Schut T. C., *Anal. Chem.* 2015;87:2419-2426.
36. Barroso E. M., Smits R. W. H., van Lanschot C. G. F., *Cancer Res.* 2016;76(20):5945-5953.
37. Malini R., Venkatakrishna K., Kurien J., *Biopolymers.* 2006;81:179-193.
38. Oliveira A. P., Bitar R. A., Silveira L., et al. *Photomed Laser Surg.* 2006;24:348-353.
39. Su L., Sun Y. F., Chen Y., *Laser Phys.* 2012;22:311-316.
40. Cals F. L. J., Schut T. C. B., Hardillo J. A., *Laboratory Investigation.* 2015;95(10):1186-96.
41. Bergholt M. S., Lin K., Zheng W., *J Biomed Opt.* 2012;17:077002.
42. Barroso E. M., Bakker Schut T. C., Caspers P. J., *Submitted to Journal of Raman Spectroscopy.*
43. Martens H., Stark E., *Journal of Pharmaceutical & Biomedical Analysis.* 1991; 9(8): 625-635.
44. Fenn M. B., Xanthopoulos P., Pyrgiotakis G., *Advances in Optical Technologies.* 2011.
45. Gautam R., Vanga S., Ariese F., *EPJ Techniques and Instrumentation.* 2015;2-8.
46. Fluss R., Faraggi D., Reiser B., *Biom J* 2005;(4):458-72.
47. Kalluri R., Weinberg R. A., *J Clin Invest.* 2009;119:1420-1428.
48. Marro M., Nieva C., Sanz-Pamplona R., *Biochimica et Biophysica Acta.* 2014;1843:1785-1795.





## ***CHAPTER 7***

***Translation to the clinics:  
development of a fiber-optic Raman  
needle probe for intra-operative  
assessment of surgical margins in  
oral cancer based on water  
concentration***



## Introduction

Every year >300,000 new cases of oral cavity squamous cell carcinoma (OCSCC) are diagnosed worldwide. The mortality rate of this type of cancer is high (145,000 deaths per year worldwide). The 5-year survival rate is poor, around 50%. Surgery is often the treatment of choice for this type of cancer (1,2). Adequate tumor resection with acceptable remaining function and physical appearance is the main goal of the surgery (3). Achieving an adequate resection margin is difficult (clear margins, > 5mm of surrounding healthy tissue). The current surgical success rate for OCSCC resection is only 15% (4,5). This low success rate clearly indicates that the current methods used for intra-operative assessment during OCSCC surgery (visual inspection and palpation) are subjective and insufficient to guarantee an adequate resection.

Although, intra-operative assessment of resection margins for OCSCC surgery can be supported by the frozen section procedure, this procedure is limited (6-10). The major limitation is that only a fraction of the resection margin or wound bed can be investigated. Additionally, this method is associated with sampling errors, which are associated to false negative results (6-10).

Ideally, the entire resection surface should be evaluated to consistently obtain a high surgical success rate and thereby improve clinical outcome of OCSCC patients.

Therefore, an objective, and rapid method is needed for intra-operative assessment of complete resection margins.

Raman spectroscopy is an objective optical technique that can be applied to obtain qualitative and quantitative information about the biochemical composition of tissues from the oral cavity.

In a previous study we have established that Raman spectroscopy can be used to discriminate OCSCC from surrounding healthy soft tissue with a sensitivity of 99% and a specificity of 92%. The discrimination was based on differences in tissue water concentration (found to be significantly higher in the tumor than in the surrounding healthy soft tissue) (11).

In a second study, we showed that the tumor border can be localized based on the water concentration distribution. The water concentration decreases from 76% ( $\pm$  8%) inside the tumor to 54% ( $\pm$  24%) in the adequate margin (12). These findings demonstrate the potential of Raman spectroscopy for objective intra-operative assessment of the resection margins based on the water concentration.

The water concentration was determined based on measurements in the high-wavenumber (HWVN) part of the Raman spectrum, which is mainly dominated by the CH-, OH-, and NH-stretching vibrations. Several studies demonstrated that for clinical applications the HWVN part of the Raman spectrum is as informative as the mostly used fingerprint (FP) region (13,14).

The previous studies were performed using a confocal Raman microspectrometer. Signal collection times of 1 second were used, which resulted in spectra with a high signal to noise ratio, allowing a quick determination of the tissue water concentration. By optimizing the measurement volume and laser power, we believe that the signal collection time per measurement can be reduced to 0.1 second or less. This will enable inspection of large resection areas in the limited time available during surgery.

To enable scanning of complete resection surface and deep tissue layers of a specimen, while this remains intact, the use of a Raman fiber-optic needle probe can be a solution.

Raman fiber-optic probes have been used to detect brain cancer, esophageal cancer and gastric cancer (15-17). The Raman signal acquired with these probes, which were multi-fiber, were mostly from the top ~1mm layer of the tissue. Other studies showed that Raman fiber-optic probes can be fitted in hypodermic needles (18,19) for assessing deeper soft tissue layers. The main requisite for this approach is to have a thin needle for optimal tissue penetration (specimen shape and size need to remain intact). Since the needle needs to be thin, a solution is to have instead of a multi-fiber probe a single optical fiber, which may be used for both, excitation and collection (20).

In this paper, we present a Raman spectroscopy system that uses a single-fiber-optic needle probe for discriminating oral cavity squamous cell carcinoma from healthy tissue based on water concentration. We demonstrate that the probe can be used to inspect the resection surface and the deep tissue layers. This is an important step towards the development of an intra-operative tool for assessing the entire tumor resection surface, which may allow an adequate tumor removal and thereby improvement of patient outcome.

## Materials and Methods

### Tissue Samples

The Medical Ethics Committee of the Erasmus MC has approved this study (MEC-2013-345, 2015-amendments). Informed consent was obtained from the patients prior to the surgical procedure. For each patient, intra-operative assessment of the resection surface of the freshly excised oral cavity squamous cell carcinoma specimen was conducted by the pathologist and surgeon. Intra-operative assessment of the resection surface was performed by visual inspection and palpation. The pathologist and the surgeon indicated the regions where they expected the smallest distance between the tumor border and the resection cut surface. Raman ex-vivo experiments were performed on the regions indicated by the pathologist and surgeon. After the experiments, the resection specimen was immersed in formalin and sent for routine histopathological evaluation.

### Fiber-optic Raman needle probe instrument

A new prototype Raman instrument, equipped with an automated fiber-optic needle probe for assessing soft tissue resection margins, was developed by RiverD International B.V. (The Netherlands), as part of a research project funded by the Dutch Cancer Foundation (project number: 106467) (figure 1).

#### *The Raman Module*

The equipment was placed in a laboratory of the Pathology department, which is close to the operating room. The setup is comprised of a custom-designed HWVN-Raman Module (RiverD International B.V., The Netherlands), enabling signal collection in the spectral range of 2500-4000  $\text{cm}^{-1}$ , a 671 nm laser (Gem671, 50 mW – 250 mW, LaserQuantum, UK) and a charge-coupled device (CCD) camera fitted with a back-illuminated deep depletion CCD-chip (Andor iVac, 316 LDC-DD, Andor Technology Ltd., UK).

The Raman module is connected to the needle probe with a cable containing a fiber patch-cord and electrical wiring.

Two different patch cords can be used by the equipment: one consisted of a step index 100  $\mu\text{m}$ -core fiber (NIR100/110AL-300-FC/PC-FC/PC-MS44, Art Photonics GmbH, Germany), and another consisted of a gradient index 50  $\mu\text{m}$  core fiber (LWL Cable GI50/125AL-300-FC/PC-FC/PC-MS44, Art Photonics GmbH, Germany).

The patch-cords are 3 m in length with FC/PC connectors at both ends, and have a protective silicone-coated stainless steel reinforced tubing (outer diameter of 4.4 mm).

The spectral resolution of the fiber-optic Raman equipment is  $>7\text{cm}^{-1}$  when the 50  $\mu\text{m}$ -core fiber is used and  $>15\text{ cm}^{-1}$  when used the 100  $\mu\text{m}$ -core fiber.



**Figure 1. First prototype: fiber optic needle probe Raman instrument.**



**Figure 2. Prototype fiber optic Raman needle probe.**

### *The needle probe*

The needle probe consists of a fiber optic needle (30G x 12 mm Omnican® insulin needle) attached to an actuator (via FC/PC) that drives the needle through a metal spoon to a maximum depth of 10mm into the tissue (SmarAct type SLC1730L linear positioned, Smaract GmbH, Germany).

The actuator is located inside the hand held plastic housing/holder of the probe (figure 2). The patch cord that conducts/transmits the light is fixed to the actuator.

Two different fiber-optic needles can be used, one with a 100  $\mu\text{m}$ -core optical fiber, and another with a 50  $\mu\text{m}$ -core optical fiber (figure 3).

The 100 $\mu\text{m}$ -core fiber-optic needle (30G GNIR100/110AL, AP11396, art photonics GmbH, Germany) is a 30 gauge needle beveled at 38 degrees that can be connected to the 100 $\mu\text{m}$  patch cord. The needle contains the optical fiber (step index silica/silica, core of 100 $\mu\text{m}$  and cladding 110 $\mu\text{m}$ , coated with aluminum), also beveled at 38 degrees on the tip, and terminated with a FC/PC connector.



**Figure 3. Example of a disposable 50 $\mu\text{m}$ -core fiber-optic needle (art photonics GmbH, Germany).**

The 50 $\mu\text{m}$ -core fiber-optic needle (30G GI50/125AL, AP11353, art photonics GmbH, Germany) is identical, but then with a graded index 50 $\mu\text{m}$  optical fiber, that can be connected to the 50 $\mu\text{m}$  patch cord.

A spoon (with a hole, see figure 2) is located at the end of the hand-held probe. The spoon can be placed on the resection surface of the specimen and the needle will be penetrating the resection surface through the hole of the spoon. After measuring the needle is automatically retracted.

## **Determination of the depth sensitivity of the probe**

Since the ultimate goal of this research is to assess surgical resection margins of OCSCC with a fiber optic needle probe that inspects tissue (up to 10 mm in depth) with a precision of <1 mm, it is crucial to guarantee that the depth sensitivity of the instrument matches with the requirements specified.

To estimate the depth sensitivity of the probe in tissue, a plastic container filled with water was prepared (non-scattering solution).

The needle probe was vertically immersed in the water of the container. Every 10  $\mu\text{m}$  a Raman spectrum was recorded, and the measurement position annotated. Measurements were performed until the probe touched plastic, which was the bottom of the recipient.

After the experiment, the Raman spectra were normalized to the total intensity.

The intensity of the water band was integrated in the range: 3350-3550  $\text{cm}^{-1}$ . In this way, the intensity of the water band was recorded as a function of depth. The first derivative of the intensity of OH band as a function of depth was calculated. The width at which the value is half of the minimum value was defined as the depth sensitivity.

The depth sensitivity, was experimentally determined for both sizes of fiber-optic needle probes. For both probes the full half width maximum of the step response (measured in a non-scattering medium) was determined and it was approximately 100  $\mu\text{m}$ .

## **Handling of tissue samples & needle probe measurements**

After intra-operative assessment, measurements were performed with the 50  $\mu\text{m}$ -core Raman fiber-optic needle probe system in the suspected region of the specimen, along a straight line indicated by pathologist and surgeon as illustrated in figure 4.a-d.

### *Water profile measurements for assessment of the resection margin*

Water profiles measurements were performed with the needle probe to assess the resection margins.

The spoon of the needle probe was positioned on the resection surface, at the region of interest. For each location of interest, the Raman needle probe was programmed

to measure from the resection surface (at 0 mm) to a depth of 6mm in steps of 1mm. The Raman needle probe was programmed to collect 100 spectra per each millimeter, to ensure a high signal quality. Each spectrum was collected with an acquisition time of 0.1 s. The laser power at the tip of the fiber-optic Raman needle probe was  $\approx 40$  mW.

Each water profile measurement was separated 5-10 mm apart (figure 4.b-d). To mark each location that was measured a colored acupuncture needle was used (figure 4.b-d).

After measuring all the locations of interest, an incision was made, perpendicularly to the resection surface and along a straight line that is in proximity to the acupuncture needles that demarcate the measured locations (figure 4.c). This allowed a macroscopic inspection of the distance between the tumor border and the measured locations at the resection surface (figure 4.d).

### *Measurements on the tissue cross section for inspection of the water concentration in tumor and in healthy tissue*

The incision made along the straight line allowed direct access to macroscopically visible tumor and healthy surrounding tissue.

Measurements were performed with the fiber-optic needle probe only at the surface of the cross section in order to test if the measurements with the Raman needle probe yielded the same results that were obtained in our previous studies (11,12). Ten to 50 frames of 0.1 second were collected per location measured. The locations were annotated on a photograph of the cross section. Measurements were separated 5 mm apart.

For the measurements on the cross section the laser power at the tip of the fiber-optic Raman needle probe was  $\approx 99$  mW.

After the experiment, care was taken to preserve the orientation of the specimen and the tissue was sent to the pathology department for the final processing.

## **Spectral calibration and Pre-processing**

For calibration and pre-processing of the spectra software was developed with MATLAB (R2014b). Calibrations of the relative wavenumber axis and of the intensity axis were carried out as described previously (21). The shape and intensity of the tissue background signal were determined using a method based on a multiple regression fitting algorithm, developed by Barroso *et al.* (2017) (22). After

subtraction of the tissue background signal the water concentration was calculated per each spectrum measured according to the method developed by Caspers et al. (2001) and described in detail elsewhere (23, 24).

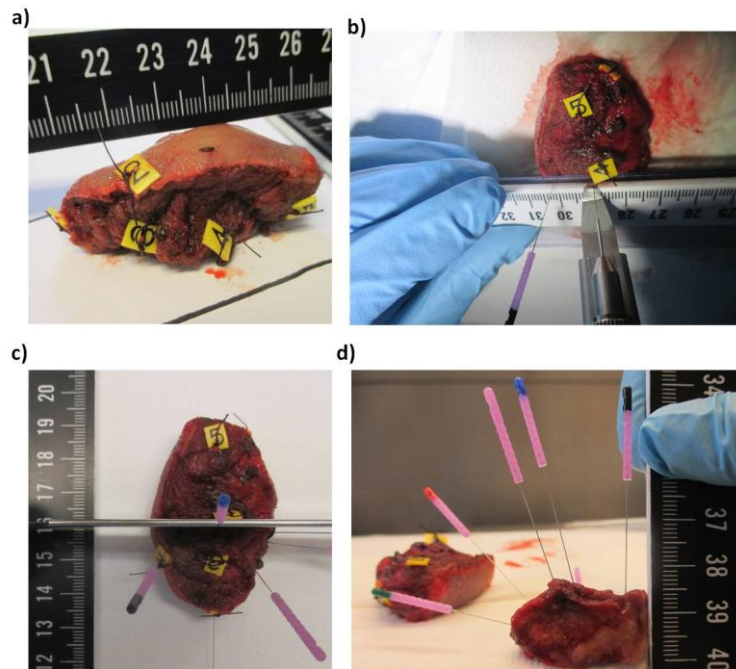


**Figure 4. Overview of the handling and measurement protocols with fiber-optic needle probe of a fresh tongue specimen. a) Intra-operative assessment of the specimen by pathologist and surgeon: visual inspection, palpation of the resection surface, and indication of the possible suspected region. The location of the possible suspected region determines where Raman measurements are performed (along a straight line). b) Water profile measurements with the fiber-optic Raman needle probe are performed and marked with colored acupuncture needles. c) Cut along the measured line. d) Macroscopic inspection of the distance between the tumor border and the measured locations at the resection cut surface (marked with needles).**

## **Water concentration Analysis**

### *Water profile measurements for assessment of the resection margin*

For each depth scan measurement of 0 to 6 mm in depth, the mean and standard deviation of the water concentrations measured per millimeter were calculated. In this way, the mean water concentration in the tissue was determined as a function of depth.

### *Measurements on the tissue cross section for inspection of the water concentration in tumor and in healthy tissue*

For each location measured superficially in the cross section, the mean and standard deviation of the water concentrations were calculated. For each location, also the distance to the resection surface was registered, so that the water concentrations were defined as a function of depth.

#### **Histopathology correlation**

Haematoxylin and eosin (H&E) stained thin sections were made from the cross-section surfaces used for macroscopic inspection of the distance between the tumor border and the resection surface (figure 4.b-d) and for inspection of the water concentration in tumor and healthy tissue, at the locations measured superficially by the Raman needle probe.

Histopathological evaluation of the H&E stained section was performed. The tissue spectra, and corresponding water concentrations were annotated as tumor or healthy tissue based on the histopathological evaluation. Also based on the H&E stained thin section, the pathologist measured the smallest distance between the tumor border and the resection cut surface.

7

## **Results**

### **Tissue Samples**

Two patients were included in the study both with OCSCC of the tongue. Therefore, the first results of the fiber-optic Raman needle probe for assessment of the resection margins and inspection of the water concentration of tumor and healthy tissue were based on OCSCC tongue specimens.

Patients and tumor characteristics are described in the table 1.

### **Needle probe measurements & water concentration analysis**

#### *Water profile measurements for assessment of the resection margin*

Five water profile measurements were performed with the needle probe at 5 different positions on an OCSCC tongue resection surface (patient 1, see table 1).

For each water profile, the mean and the standard deviation of the water concentrations were calculated per millimeter. These values are shown in the table 2.

**Table 1. Clinical and hitopathological characteristics of the patients and tissue samples.**

Patient	Age	Gender	Location	cTNM	pTNM	OCSCC Grading
1	60	F	tongue	cT2N0M0	pT2N1	Moderate differentiated
2	83	M	tongue	cT4N0M0	pT2N0	Moderate to poor differentiated

**Table 2. Water profile measurements performed on a tongue resection specimen with the fiber-optic Raman needle probe.**

Depth from the resection cut surface	Needle Color					
	Green	Red	Pink	Black	Blue	
Mean [H <sub>2</sub> O]±std(%)	0mm	66.8±5.2	9.4±0.5	70.9±5.5	48.5±1.8	75.8±0.8
	1mm	54.3±5.5	22±2.6	68.2±1.7	74.7±1.4	77.3±0.5
	2mm	28.5±7.05	18.2±0.9	63.9±1.2	46.3±2.6	77.2±0.6
	3mm	23.6±1.9	15.6±0.7	63.5±1	28.5±1.6	78.3±3.4
	4mm	24.3±2.5	14.8±0.7	64.4±1.2	30±2.4	72.1±3.3
	5mm	23.3±2.8	16.3±1.3	62±1.8	64.4±2	63.7±1
	6mm	21.3±2.8	19.3±1.2	60.4±1.4	64.5±1.2	60.8±1.1

*Measurements on the tissue cross section for inspection of the water concentration in tumor and in healthy tissue*

On the cross section of another tongue specimen (patient 2, see table 1), 4 measurements were performed, see figure 5.

The mean and standard deviation of the water concentrations measured were calculated for the 4 different locations between the two pink pins (figure 5).

At the location 1, which is at approximately 0 mm from the resection surface, the mean water concentration was 61% and the standard deviation was 8.6%.

At the location 2, which is at 5 mm from the resection surface, the mean water concentration was 27% and the standard deviation was 0.5%.

At the location 3, which is at 10 mm from the resection surface, the mean water concentration was 72% and the standard deviation was 0.7%.

The location 4 (at 15 mm from the resection surface) had a mean water concentration of 75.4% and a standard deviation of 0.6%.

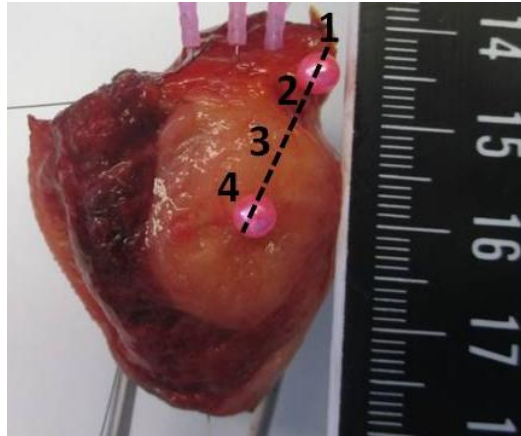


**Figure 5.** Cross section view of the tongue specimen inspected superficially with the fiber-optic Raman needle probe. The start point and end point of the measurements are marked with pink spherical pins. Position 1 marks the start point. Position 4 marks the end point. Measurements were performed along the dashed line (5mm apart from each other) on the cross section of the specimen (1-4). The measurements can be assigned as function of depth (0-15mm).

### Histopathology correlation

H&E stained sections made from the cross sections were used for inspection of the distance between the tumor border and the resection surface (figure 6), and for inspection of the water concentration in tumor and healthy, when performing superficial measurements on the cross section (figure 7).

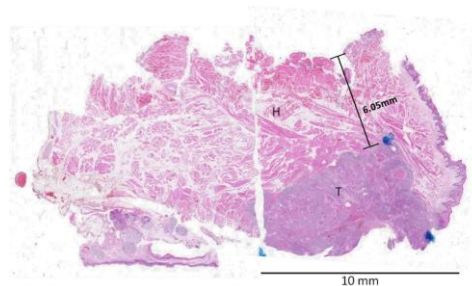


**Figure 6.** H&E stained section made of the cross section from the tongue specimen of patient 1 where water profile/depth scan measurements were performed. The resection surface was marked with ink during the gross pathology of the specimen. The resection

margin (smallest distance between the resection surface marked with ink and the border of the tumor) was measured and it is shown (6.05 mm). The resection margin is adequate. Healthy tissue (H) and tumor (T) are also marked.

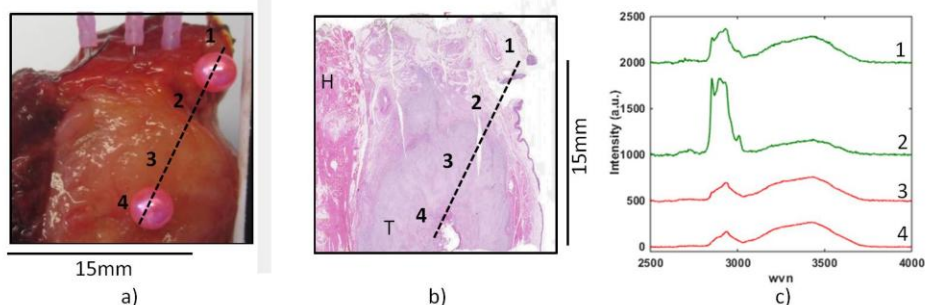


**Figure 7.** Illustration of superficial measurements performed with the fiber-optic Raman needle probe on a cross section of the specimen of patient 2. a) Cross section view of the tongue specimen inspected. The start point and end point of the measurements are marked with pink spherical pins and with numbers (from 1 to 4). The measurements can be assigned as function of depth (0-15mm). b) H&E stained section of the cross section measured. Based on the H&E stained section measurements 1 and 2 are healthy (H) and measurements 3 and 4 are from tumor (T). c) Mean spectra measured per location. At each location 10 to 50 frames were measured (0.1s acquisition time). Spectra obtained from healthy tissue are shown in green (1 and 2). Spectra obtained from tumor are shown in red (3 and 4).

## Discussion

For this study, a thin fiber optic needle probe prototype, consisting of a single optical fiber inserted into a 30G hypodermic needle was developed.

The first experiments performed by this prototype are shown. This fiber optic probe enables collection of HWVN Raman spectra.

The measurements performed superficially on the tongue cross section (figure 7) with the fiber-optic Raman needle probe show that tumor has high water concentration and healthy tissue has generally low water concentration. This confirms what was found in previous studies (11,12). These measurements form the basis for using a fiber-optic Raman needle probe for assessment of soft tissue resection margins of OCSCC specimens.

The water profile can be used to determine the distance between the resection surface and the tumor border. If the probe measures high water concentration at a distance of less than 5 mm from the resection surface, it means that the margin is inadequate and, therefore, an extra-resection should be performed. If the probe measures low water concentration along a distance of more than 5 mm from the resection surface, it means that at that specific location the margin is adequate.

The performed water profiles are summarized in the table 2. Two water profiles, marked with the red and green needles, had low values of water concentration along 6 mm in depth. Therefore, knowing that tumor has always high water concentration and healthy tissue has in average low water concentration, for these two locations the tissue measured is healthy, which means that the distance between the resection surface and the tumor border is  $>5$  mm (adequate). Based on the histopathological assessment, see figure 6, it can be confirmed that the measured tissue is healthy (the smallest distance found between the tumor border and the resection cut surface was 6.05 mm). This indicates that the resection margin is adequate ( $>5$  mm).

For three water profile measurements (also shown in the table 2), high water concentrations were found, sometimes in between low water concentrations. Knowing that the tissue is healthy (based on histopathological evaluation), the reason why high water concentrations can be found also in healthy tissue may be explained by earlier studies (12). Results obtained in these earlier studies show that the healthy tongue tissue is characterized in average by a low water concentration with a high standard deviation  $54\% \pm 24\%$ . This means that in healthy tissue also some high water concentrations can be encountered (12).

The fiber-optic Raman needle probe system has a depth sensitivity that it is different from the depth sensitivity of the setup used in the previous studies, which supported the development of the current equipment. Therefore, more studies will be performed in order to determine the optimal water cut-off that determines the tumor border from a profile. Additionally, more investigation will be made to know what other sampling/measuring strategies can be developed to reliably and accurately determine the distance between the tumor border and the resection surface of OCSCC specimens.

Some technical issues/limitations were observed when experimenting the fiber-optic Raman needle probe. For some experiments, the needle did not penetrate smoothly in the tissue (especially, when measuring dense/fibrotic tissue), and, in many cases, the needle was compressing the tissue before penetrating the resection surface. The needle can become contaminated after a water profile measurement, therefore, in between water profiles the needle was cleaned with an ultrasonic bath. The solutions

for these problems are currently being investigated and the technical and functional characteristics of the probe will be further optimized with respect to speed and reliability. In the future, some non-expert personnel may be able of using the probe without observing any technical issue.

The quality of the signal measured (acquisition time of 0.1s and laser power of  $\approx$ 40-100 mW) with the needle probe seems, in most cases, adequate for an accurate calculation of the water concentration (shot-noise does not limit the calculation of the water concentration).

Based on these preliminary results, the proof of concept is made and we believe that a fiber-optic Raman needle probe instrument is an excellent candidate for assessment of OCSCC resection margins and its implementation may significantly improve the number of adequate resections.

## References

1. Ferlay J., Soerjomataram I., Dikshit R., *Int J Cancer*. 2014;136:E359–86.
2. Karim-Kos H. E., de Vries E., Soerjomataram I., *Eur J Cancer*. 2008;44:1345–89.
3. Guntinas-Lichius O., Wendt T., Buentzel J., *J Cancer Res Clin Oncol*. 2010;136:55–63.
4. Sant M., Allemani C., Santaquilani M., Knijn A., *Eur J Cancer*. 2009;45:931–91.
5. Woolgar J. A., *Oral Oncol*. 2006;42:229–39.
6. Pathak K. A., Nason R. W., Penner C., *Oral Surg Oral Med Oral Pathol Oral Radiol Endod*. 2009;107: 235–9.
7. Gandour-Edwards R. F., Donald P. J., Wiese D. A., *Head Neck*. 1993;15:33–8.
8. Hinni M. L., Ferlito A., Brandwein-Gensler M. S., *Head Neck*. 2013;35:1362–70.
9. Yahalom R., Dobriyan A., Vered M., *J Surg Oncol*. 2008;98:572–8.
10. Smits R. W. H., Koljenovic S., Hardillo J. A., *Head Neck*. 2016;38Suppl 1:E2197–203.
11. Barroso E. M., Smits R. W. H., Bakker Schut T. C., *Anal Chem*. 2015;87: 2419–26.
12. Barroso E. M., Smits R. W. H., van Lanschot C. G. F., *Cancer Res*. 2016;76(20):5945-5953.
13. McGregor H. C., Short M. A., McWilliams A., *J Biophotonics*. 2017;10(1):98-110.
14. Teh S. K., Zheng W., Ho K.Y., *Br J Cancer*. 2008;98(2):457–65.
15. Jermyn M., Mok K., Mercier J., *Sci. Transl.* 2015;Med. 7(274): 274ra19-274ra19.
16. Wang J., Lin K., Zheng W., *Sci Rep.* 2015;5(August):12957.
17. Lin K., Wang J., Zheng W., *Cancer Prev. Res.* 2016;9(6):476-483.
18. Petterson I. E. I., Day J. C. C., Fullwood L. M., *Anal. Bioanal. Chem.* 2015;407(27):8311-8320.
19. Santos L. F., Wolthuis R., Koljenović S., *Anal. Chem.* 2005;77(20):6747-6752.
20. Day J. C. C., and Stone N., *Appl. Spectrosc.* 2013;67(3):349-354.
21. Malini R., Venkatakrishna K., Kurien J., *Biopolymers*. 2006;81:179–193.
22. Barroso E. M., Bakker Schut T. C., Caspers P. J., *Submitted to Journal of Raman Spectroscopy*.
23. Wolthuis R., Van Aken M., Fountas K., *Anal. Chem.* 2001;73:3915-3920.
24. Caspers P. J., Lucassen G. W., Certer E. A., *Journal of Investigative Dermatology*. 2001;116(3):434-442.





## ***CHAPTER 8***



### ***General discussion & Outlook***



## General discussion

In head and neck surgical oncology, the lack of intra-operative methods to discriminate tumor from non-tumor with sufficient or clinically relevant sensitivity and specificity is an issue. This thesis provides a solution for that clinical necessity.

The most common type of cancer in head and neck region is oral cavity squamous cell carcinoma (OCSCC). Therefore, in this thesis, the potential of Raman spectroscopy for intra-operative assessment of soft resection margins and bone resection surfaces of freshly resected OCSCC specimens was investigated. Raman spectroscopy is a valuable solution because this technique is objective, can be performed in-vivo and or ex-vivo, the tissue samples do not need preparation, and can be processed in real-time (1).

The Raman systems used in this thesis operate with the high-wavenumber region of the Raman spectrum (wavenumbers ranging from about  $2400\text{ cm}^{-1}$  up to  $4000\text{ cm}^{-1}$ ). The interest for using high-wavenumber Raman spectroscopy was based on two facts: a) Koljenović *et al.* showed that, for discriminating cancer from healthy tissue, essentially the same diagnostic information is obtained in either of the two spectral regions (fingerprint or high-wavenumber) (1), and b) Raman spectroscopy in the high-wavenumber region has significant advantages for ex-vivo and in-vivo use when compared to the commonly used fingerprint region. The signal intensity in the high-wavenumber region is higher than in the fingerprint region, and measurements can be performed in shorter integrations times. Additionally, fiber-optic materials like fused silica do not have Raman signal at the high-wavenumber region (1), which enables the use of simple and cheap single fiber-optic probes that can be easily inserted in endoscopes and/or needles to perform in-vivo measurements in hollow organs or surface assessment of solid organs such as, oral cavity (2,3), lung (4,5), upper gastrointestinal tract (6-8) and colorectal (9,10).

For the measurements described in this thesis, both, microscope and optical fibers were used for illumination and collection of light, a 671 nm excitation wavelength was used as excitation light source, and Raman signal was collected in the range  $\approx 800\text{-}920\text{ nm}$ . Combining these characteristics in a Raman instrument, minimal absorption of the light by water and hemoglobin ( $\text{HbO}_2$  and Hb), which contribute to degradation and camouflage of the Raman signal, was guaranteed.

Some important findings have supported the development of intra-operative guidance (IOG) Raman tools for assessment of the resection margins.

This thesis shows that Raman spectroscopy can discriminate OCSCC from the surrounding healthy soft tissue based on the water concentration as determined from the high-wavenumber spectra (11), with 99% sensitivity and 92% specificity (170-point measurements/ 14 patients) (10).

The method used to calculate the water concentration can be seen as a limitation because it was devised for protein–water mixtures and does not take into account the signals from lipids, which also contribute to the CH-stretching Raman band (2910–2966  $\text{cm}^{-1}$ ). However, the measurements with a high signal from lipids have shown consistently low water contribution, and were always associated with healthy tissue. Therefore, even though the determination of the water concentration is based on a protein model, the signal contributions from lipids are unlikely to influence our discrimination results regarding discrimination of tumor and healthy tissue (10).

Also, for this thesis, a method, called multiple regression fitting (MRF), for subtraction of luminescence background of high-wavenumber Raman spectra from freshly resected human oral tissue was developed, and its performance was compared with the most used method, polynomial baseline fitting (PBF) (12). MRF does not require an *a priori* choice of the polynomial order for fitting the background signal, and this is important because, as it is also shown in this thesis, no single polynomial order can optimally characterize all backgrounds that are encountered in high-wavenumber tissue spectra. Therefore, MRF is more robust than and preferable to PBF. This was an important development because it facilitates the analysis of Raman signal and reduces the influence of the luminescence background in the calculation of the water concentration in tissue (12).

Knowing that OCSCC could be discriminated from healthy tissue based on the water concentration and that the calculation of the water concentration would not be influenced by the luminescence properties of tissue, in this thesis, the changes in water concentration across the OCSCC border toward the healthy surrounding tissue (located at  $>5$  mm from the tumor border) were investigated (25 mapping experiments/ 20 patients). During this study, it was discovered that a transition from a high to a lower water concentration, from OCSCC ( $76\% \pm 8\%$ ) toward healthy surrounding tissue ( $54\% \pm 24\%$ ), takes place over 4 to 6 mm across the OCSCC border. This information can be used to detect the location of the OCSCC border (13).

Furthermore, also in this thesis, it is demonstrated that Raman spectroscopy can detect OCSCC in bone resection surfaces with high sensitivity (96%) and specificity (83%) during mandibular resections (26 mapping experiments/ 22 patients) (14). These results demonstrate that Raman spectra of bone resection specimen provide

valuable information to distinguish between healthy tissue and OCSCC. Therefore, Raman spectroscopy could be applied *ex-vivo* for evaluation of bone resection margins (including bone marrow and cortical bone) during OCSCC surgery. However, implementation in the clinical workflow also requires the elimination of a practical issue that sometimes occurred: the lack of contact between the surface of the bone section and the fused silica window of the measurement cartridge. This problem leads to a low-quality Raman signal. Also, to guarantee a good quality of the Raman signal, it is important to cut the bone in a manner that it results in a flat and smooth surface. Alternatively, a method can be employed by which the contours of the surface are automatically followed by the measurement system (such as, *inViaTMQontorTM*, Renishaw B.V., United Kingdom).

Finally, a Raman needle probe prototype, consisting of a single optical fiber inserted into a 30G hypodermic needle is presented and the first experiments performed by this prototype are shown. The fiber-optic probe enables collection of high-wavenumber Raman spectra and the first measurements performed on OCSCC confirm what was found in earlier work (tumor has high water concentration and healthy tissue has in average low water concentration). The water profile measure through the fiber-optic needle probe will be used to determine the distance between the resection surface and the tumor border. In this way, when the probe measures high water concentration at a distance of less than 5 mm from the resection surface, it means that the margin is inadequate. If the probe measures low water concentration along a distance of more than 5mm from the resection surface, it means that at that specific location the margin is adequate. Additionally, some technical issues were observed when experimenting the fiber-optic Raman needle probe: the needle did not penetrate smoothly in the tissue (especially, when measuring dense/fibrotic tissue). In many cases, the needle was compressing the tissue before penetrating the resection surface. The solutions for these problems are currently being investigated and the technical and functional characteristics of the probe will be further optimized with respect to speed and reliability.

Based on these preliminary results the proof of concept is made and we believe that a fiber-optic Raman needle probe instrument will be an excellent candidate for assessment of OCSCC soft tissue resection margins.

The use of the IOG tools developed in this thesis may contribute positively to the future of the head and neck surgical oncology field, see figure 1.

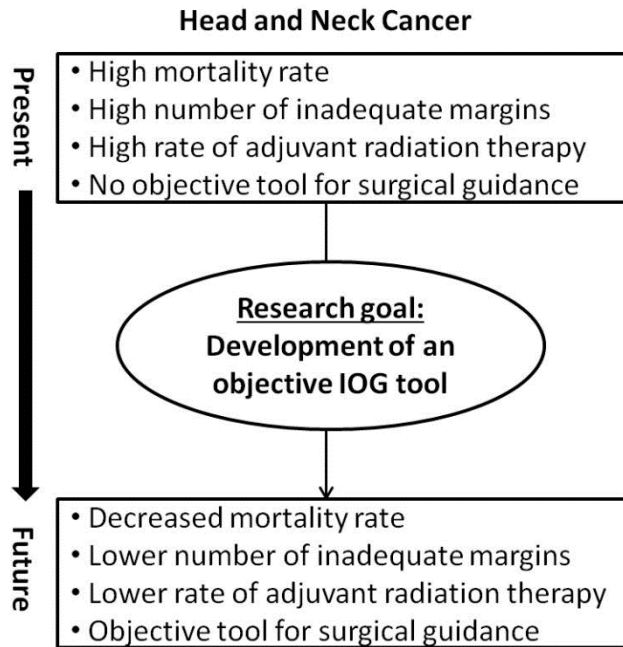


**Figure 1. Diagram that demonstrates the impact of this thesis in the future of head and neck surgical oncology.**

## **Outlook**

### **Raman pathology system for assessment of bone resection surfaces**

Studies have reported that tumor-positive bone resections are found in 2-21% of the cases when a mandibulectomy for OCSCC is performed (15-19). Additionally, there is no standard technique available for assessment of bone resection surfaces (20-25). Therefore, the Raman system for assessment of bone resection surfaces could be implemented for clinical decision making regarding the need for additional bone resection when a mandibulectomy for OCSCC is performed.

From the technical point of view, the first approach could be to apply the tumor detection algorithm created on every bone resection surface and use the false positive rate encountered in bone sections without tumor as a threshold below which the bone section is classified as tumor free. However, this, as well as more elaborate approaches, should be the subject of further studies.

From the clinical point of view, the aim for the future is to scan the complete mandibular resection surface by Raman spectroscopy during the mandibulectomy procedure. The result should be delivered to the surgeon in less than 20 minutes. If the result demonstrates bone resection surfaces are tumor free, the reconstruction surgery can start, and it is guaranteed that tumor was not left in the bone of the patient. If the result is the resection surface(s) contain(s) tumor, the surgeon can resect an extra bone slice during the first surgery, aiming for a tumor-free patient, adequate resection.

Future studies should clarify whether this could improve the number of tumor free bone resections, and consequently reduce the extent of adjuvant treatment. Equally essential, having a method for intra-operative assessment of bone resection surfaces, might give surgeons the confidence to adjust initial cut line and resect the bone closer to the suspected tumor border. In this way, healthy bone might be spared, which will positively influence the reconstruction and reduce the possible post-operative complications.

### **Raman pathology system for assessment of soft tissue resection margins**

The Raman needle probe system could be implemented for assessment of the entire soft tissue resection margin during OCSCC surgery. The Raman instrument could be placed in the operating room. After resection of the specimen, one operating room assistant could be responsible for using the Raman needle probe to inspect the resection margins of the specimen. The assistant should place the needle probe perpendicularly to the surgical cut surface. The assistant could use the automatic depth scan to know what is the smallest distance between the surgical cut surface and the tumor border. This means that the resection margin of every resected specimen could be evaluated during the operation. If the margin is inadequate in a certain location, the surgeon would be informed, and he/she could perform an extra-resection at the inadequate place. In this way, a resection that would be inadequate turns into an adequate resection. Further studies are being developed to assure that the location of inadequate margins can be informed to the surgeon in an accurate, simple and elegant manner (26).

Clinical studies have been initiated to monitor whether the use of the Raman needle probe system for assessment of soft tissue resection margins during OCSCC surgery will impact positively the outcome of the surgical procedures. The use of this objective tool should increase the number of adequate margins, lower the rate of adjuvant radiation therapy, and decrease the mortality rate of the patients that undergo OCSCC surgical procedures.

The fiber-optic Raman needle probe system has a depth sensitivity that is different from the depth sensitivity of the setup used in the previous studies. Therefore, more studies need to be performed to determine the optimal water concentration cut-off to determine the tumor border from the water profile with high accuracy.

Also, more research need to be conducted to know what other sampling/measuring strategies can be developed to more reliably and accurately determine the distance between the tumor border and the resection surface of OCSCC specimens.

## References

1. Koljenović S., Bakker Schut T. C., Wolthuis R., *Journal of Biomedical Optics*. 2005;10(3): :031116.
2. Krishna H., Majumder S. K., Chaturvedi P., *J Biophotonics*. 2014;7(9):690–702.
3. Guze K., Pawluk H. C., Short M., *Head Neck*. 2015;37(4):511–7.
4. Short M. A., Lam S., McWilliams A., *Opt Lett*. 2008;33(7):711–3.
5. McGregor H. C., Short M. A., McWilliams A., *J Biophotonics*. 2017;10(1):98–110.
6. Teh S. K., Zheng W., Ho K. Y., *Br J Cancer*. 2008;98(2):457–65.
7. Bergholt M. S., Zheng W., Lin K., *Analyst*. 2010;135(12):3162–8.
8. Duraipandian S., Bergholt M. S., Zheng W., *J Biomed Opt*. 2012;17(10).
9. Bergholt M. S., Lin K., Wang J., *J Biophotonics*. 2016;9(4):333–42.
10. Barroso E. M., Smits R. W. H., Bakker Schut T. C., *Anal Chem*. 2015;87(4):2419–26.
11. Caspers P. J., Lucassen G. W., Carter E. A., *J Invest Dermatol*. 2001;116(3):434–42.
12. Barroso E. M., Bakker Schut T. C., Caspers P. J., *J Raman Spectrosc*. 2018.
13. Barroso E. M., Smits R. W. H., Van Lanschot C. G. F., *Cancer Res*. 2016;76:5945–5953.
14. Barroso E. M., ten Hove I., Bakker Schut T. C., *European Journal of Cancer*. 2018.
15. Binahmed A., Nason R. W., Abdoh A. A., *Oral Oncol*. 2007;43:780–4.
16. Schusterman M. A., Harris S. W., Raymond A. K., *Head & Neck*. 1993;15:204–207.
17. Brown J. S., Kalavrezos N., D’Souza J., *British Journal of Oral and Maxillofacial Surgery*. 2002;40:275–284.
18. Bilodeau E. A. and Chiosea S., *Head and Neck Pathology*. 2011;5:2016–220.
19. Smits R. W. H., ten Hove I., Koljenović S., *Journal of Oral & Maxillofacial Surgery*. Submitted and under revision.
20. Maciejewski A., Szymczyk C., *J Reconstr Microsurg*. 2007;23:1–10.
21. Holzle F., Kesting M. R., Holzle G., *Int J Oral Maxillofac Surg*. 2007;36:802–6.
22. Markowitz B. L., Calcaterra T. C., *Clin Plast Surg*. 1994;21:9–14.
23. Nieberler M., Häusler P., Drecolli E., *Cancer Cytopathology*. 2014;122:646–56.
24. Nieberler M., Häußler P., Kesting M. R., *Ann Surg Oncol*. 2016.

25. Helliwell T., Woolgar J., *The Royal College of Pathologists*. 2013.

26. van Lanschot C. G. F., Mast H., Hardillo J. A., *Submitted to Annals of Surgery*.





# ***CHAPTER 9***

***Summary, Sumário, Samenvatting***



## Summary

Clinical necessities in surgical oncology are based on the same fundamental issue: lack of pre- and intra-operative methods with sufficient and/or clinically relevant sensitivity and specificity. This thesis provides a technical solution for these clinical necessities in head and neck surgical oncology.

In this thesis we investigated the potential of Raman spectroscopy for ex-vivo intra-operative surgical guidance.

This thesis shows that oral cavity squamous cell carcinoma (OCSCC) can be discriminated from surrounding healthy soft tissue and healthy bone using Raman spectroscopy with a high sensitivity and specificity (respectively, sensitivity of 99% and 96% and specificity of 92% and 83%). The discrimination is mainly based on the water concentration of these tissues, determined by using the Raman spectrum. OCSCC has more water content than the surrounding healthy tissue or bone. The information on the water concentration also proved to be useful for detection of the OCSCC border.

To guarantee that the calculation of the water concentration and the processing of the spectra is not influenced by noise or signal that did not result from Raman scattering, a method (multiple regression fitting, MRF) for subtraction of luminescence background was created. Its performance was compared to the current most used method (polynomial baseline fitting, PBF). Results indicate that MRF is more robust and therefore preferable to PBF.

Additionally, a Raman needle probe for intra-operative assessment of soft tissue resection margins was developed and is being optimized to guide surgeons towards an adequate OCSCC resection.

Finally, intra-operative use of Raman pathology systems for assessment of soft tissue resection margins and bone resection surfaces may affect positively the outcome of head and neck surgery. The intra-operative use of these tools may: decrease the number of inadequate margins, lower the rate of adjuvant radiation therapy, and decrease the mortality rate of the patients that undergo OCSCC surgery.



## Sumário

As necessidades clínicas em oncologia cirúrgica baseiam-se na mesma questão fundamental: falta de métodos pré e intra-operatórios com suficiente e/ou clinicamente relevante sensibilidade e especificidade. Esta tese fornece uma solução para estas necessidades clínicas em oncologia cirúrgica de cabeça e pescoço.

Nesta tese, foi investigado o potencial de espectroscopia de Raman para a orientação cirúrgica intra-operatória a partir de espécimes (ex-vivo).

Esta tese demonstra que, usando espectroscopia de Raman, o carcinoma de células escamosas da cavidade oral (CCEO) pode ser discriminado de tecido mole saudável circundante e de osso saudável com elevada sensibilidade e especificidade (respectivamente, sensibilidade de 99% e 96%, e especificidade de 92% e 83%). A discriminação é fundamentalmente baseada na concentração de água existente nesses tecidos que é determinada a partir do espectro Raman. CCEO tem maior concentração de água do que o tecido mole saudável circundante e o osso. A informação referente à concentração de água também provou ser útil para a detecção da borda do tumor.

Para garantir que o cálculo da concentração de água e o processamento dos espectros não sejam influenciados pelo ruído ou sinal que não resultou de dispersão Raman, foi criado um método (multiple regression fitting, MRF) para a subtração de fundo de luminescência. A performance deste método foi comparada ao método mais utilizado actualmente (polynomial baseline fitting, PBF). Os resultados indicam que o método MRF é mais robusto e, por conseguinte, preferível ao PBF.

Para além disso, foi desenvolvida uma sonda de agulha Raman, para a avaliação intra-operatória das margens de ressecção de tecido mole. Presentemente, a sonda está a ser optimizada para orientar os cirurgiões a obter margens adequadas aquando a ressecção de CCEO.

Por último, o uso intra-operatório de sistemas patológicos baseados em tecnologia Raman, para a avaliação das margens de ressecção do tecido mole e das superfícies ósseas de ressecção, pode afectar positivamente o resultado da cirurgia oncológica de cabeça e pescoço. O uso intra-operatório destes equipamentos possibilita: a diminuição do número de margens inadequadas, a redução da dose de radiação da terapia adjuvante e a diminuição da taxa de mortalidade dos pacientes que foram submetidos a cirurgia para remoção de CCEO.



## Samenvatting

Klinische benodigdheden in de oncologische chirurgie zijn gebaseerd op hetzelfde fundamentele probleem: gebrek aan pre- en intra-operatieve methoden met voldoende en/of klinisch relevante sensitiviteit en specificiteit. Dit proefschrift biedt een technische oplossing voor deze klinische noodzaak in hoofd-hals oncologische chirurgie.

In dit proefschrift hebben we het potentieel van Raman spectroscopie voor ex-vivo intra-operatieve chirurgische begeleiding onderzocht.

Dit proefschrift laat zien dat plaveiselcelcarcinoom (PCC) van de mondholte onderscheiden kan worden van omringend gezond weefsel en bot met het gebruik van Raman spectroscopie, met een hoge sensitiviteit en specificiteit (respectievelijk, een sensitiviteit van 99% en 96% en een specificiteit van 92% en 83%). De discriminatie is voornamelijk gebaseerd op de waterconcentratie van deze weefsels, bepaald met behulp van het Raman spectrum. Het PCC heeft meer waterinhoud dan het omringende gezonde weefsel of gezond bot. De informatie over de waterconcentratie bleek ook van nut voor de detectie van de tumor grens.

Om te garanderen dat de berekening van de waterconcentratie en de verwerking van de spectra niet wordt beïnvloed door ruis of signalen, die niet het resultaat zijn van Raman verstrooiing, is voor dit proefschrift een methode (multiple regressie fitting, MRF) voor het aftrekken van de luminescentie achtergrond gemaakt. De uitkomst werd vergeleken met de huidige meest gebruikte methode (polynoom baseline fitting, PBF). De resultaten geven aan dat MRF meer robuust is en de voorkeur heeft boven PBF.

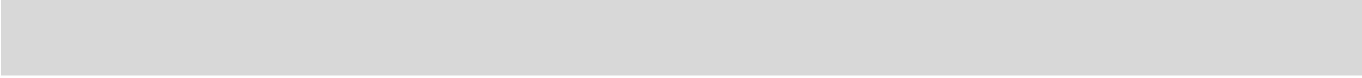
Daarnaast is er een Raman-probe ontwikkeld voor intra-operatieve beoordeling van de resectiemarges voor zachte weefsels en wordt deze geoptimaliseerd om de chirurgen te begeleiden naar een adequate tumor resectie.

Ten slotte kan het intra-operatieve gebruik van Raman pathologie systemen voor de beoordeling van resectiemarges voor zachte weefsels en bot resectievlakken de uitkomst van hoofd-hals chirurgische ingrepen positief beïnvloeden. Het intra-operatieve gebruik van deze hulpmiddelen zou: het aantal inadequate marges kunnen verlagen, de toepassing van adjuvante radiotherapie verlagen en de mortaliteit verlagen van de patiënten, die een operatie ondergaan wegens een PCC van de mondholte.









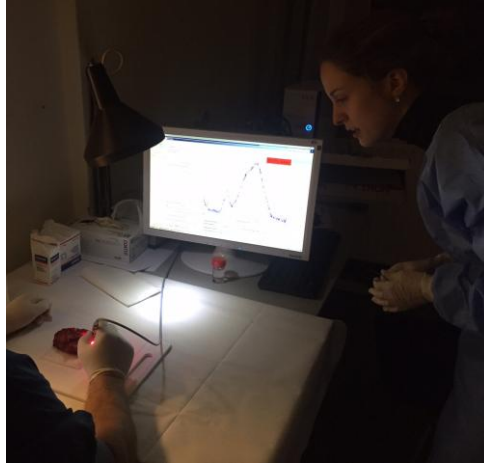
# ***CHAPTER 10***



***About the author***



## Biography



Elisa Barroso was born in 1988. Her father, Manuel Cunha Barroso, and her mother, Maria de Lurdes da Cunha Lamego Barroso, have stimulated her to pursue intellectual growth. Since always, Elisa has been following their advice.

In 2006, she started a bachelor in Biomedical Engineering at the School of Management and Industrial Studies (ESEIG) from Polytechnic Institute of Porto. She finished the bachelor's degree in 2009. Right after, in September 2009, she started a master's degree in Biomedical Engineering at the Faculty of Engineering from University of Porto. During the second year of her master's degree, she started her career in science, working in collaboration with the Institute of Science and Innovation in Mechanical and Industrial Engineering (INEGI), Porto, Portugal.

After finishing her master's degree, she decided to continue with scientific research. Therefore, she worked as a research fellow in two more projects (the project NOISYRIS, Recognition of Periocular Region, in the Tele-communications Institute from Covilhã; and the project PTDC/EIA-EIA/099458/2008IPATIMUP: Universal evaluation system of diseases based on molecular markers in IPATIMUP (Institute of Pathology and Molecular Immunology from University of Porto), Porto, Portugal).

The scientific experiences and the research developed in Portuguese institutes made Elisa curious about how the scientific research is developed internationally. To experience that, she decided to apply for PhD positions abroad and since 2013 she has been dedicated to the department of Maxillofacial surgery and to the Raman group of Erasmus University Medical Center, Rotterdam, The Netherlands. This book is the result of her dedication.

## List of publications

**E. M. Barroso**, I. ten Hove, T. C. Bakker Schut, H. Mast, C. G. F. van Lanschot, R. W. H. Smits, P. J. Caspers, R. Verdijk, V. Noordhoek Hegt, R. J. Baatenburg de Jong, E. B. Wolvius, G. J. Puppels S. Koljenović. Raman spectroscopy for assessment of bone resection margins in mandibulectomy for oral cavity squamous cell carcinoma. *European Journal of Cancer*. 2018; 92: 77-87.

**E. M. Barroso**, T. C. Bakker Schut, P. J. Caspers, I. P. Santos, E. B. Wolvius, S. Koljenović, G. J. Puppels. Characterization and subtraction of luminescence background signals in high-wavenumber Raman spectra of human tissue. 2018. DOI:10.1002/jrs.5338.

I. P. Santos, **E. M. Barroso**, T. C. Bakker Schut, P. J. Caspers, C. G. F. van Lanschot, D-H. Choi, M. F. Van der Kamp, R. W. H. Smits, R. Van Doorn, R. Verdijk, V. Noordhoek Hegt, J. H. von der Thusen, C. H. M. van Deurzen, L. B. Koppert, G. J. L. H. van Leenders, P. C. Ewing-Graham, L. C. van Doorn, C. M. F. Dirven, M. B. Busstra, J. A. U. Hardillo, A. Sewnaik, I. ten Hove, H. Mast, D. Monserez, C. A. Meeuwis, T. Nijsten, E. B. Wolvius, R. Baatenburg de Jong, G. J. Puppels, S. Koljenović. Raman spectroscopy for cancer detection and cancer surgery guidance: translation to the clinics. *The Analyst*. 2017;142(17):3025-3047. DOI: 10.1039/C7AN00957G.

**E. M. Barroso**, R. W. H. Smits, C. G. F. van Lanschot, P. J. Caspers, I. ten Hove, H. Mast, A. Sewnaik, J. A. U. Hardillo, C. A. Meeuwis, R. Verdijk, V. Noordhoek Hegt, R. Baatenburg de Jong, E. B. Wolvius, T. C. Bakker Schut, S. Koljenović, G. J. Puppels. Water concentration analysis by Raman spectroscopy to determine the location of the tumor border in oral cancer surgery. *Cancer Research*. 2016; 76(16). DOI:10.1158/0008-5472.CAN-16-1227.

**E. M. Barroso**, R. W. H. Smits, T. C. Bakker Schut, I. ten Hove, J. A. U. Hardillo, E. B. Wolvius, R. Baatenburg de Jong, S. Koljenović, G. J. Puppels. Discrimination between oral cancer and healthy tissue based on water content determined by Raman Spectroscopy. *Analytical Chemistry*. 2015; 87(4):2419-2426. DOI: 10.1021/ac504362y.

## PhD Portfolio

Name PhD candidate	Elisa Maria L. Barroso
Erasmus MC department	Oral and maxillofacial surgery
Research school	Molecular Medicine
PhD period	May 2013 – May 2018
Promotor	Prof. dr. E. B. Wolvius

Summary of PhD training and teaching

---

### PhD training:

---

#### General Courses, seminars, and workshops

Biomedical English Writing Course	2013
Scientific Integrity	2014
VENI Masterclass	2017
Workshop Writing Successful Grant Proposals	2017
Oral and Maxillofacial surgery Research meetings (every month)	2014-2017
Maxillofacial surgery Raman research monthly meeting	2014-2017
3 Quarterly Progress Meeting – Raman group	2014-2017

#### Oral presentations at conferences

<i>Daniel den Hoed Day</i> Rotterdam, The Netherlands	2015
<i>Voorjaarsvergadering NVMKA</i> Rotterdam, The Netherlands	2015
<i>SPEC</i> Montreal, Canada	2016

<i>NWHHT Jonge Onderzoekers Dag</i> Rotterdam, The Netherlands	2017
<i>Erasmus MC Cancer Institute Research Day</i> Rotterdam, The Netherlands	2017
<i>Trends in Head and Neck Oncology (THNO)</i> Nice, France	2017

#### **Attendance to national/international congresses with poster presentation**

<i>Daniel den Hoed Day</i> Rotterdam, The Netherlands	2013
<i>SPEC, Shedding new light on disease</i> Krakow, Poland	2014
<i>10<sup>th</sup> ORLIAC meeting (International Academic conference in Otorhinolaryngology)</i> Manila, Philippines	2018

---

#### **Teaching and supervision activities:**

---

##### **Supervising students:**

3 Bachelor students (6 months supervision per student) 2015- 2018

---

#### **Awards and Patents:**

---

Best Poster award - SPEC 2014 Shedding New Light on Disease - 17-22 August 2014 Krakow, Poland. Towards Raman-guided tumor surgery: discriminating squamous cell carcinoma from healthy tissue based on water content.

PCT/NL2016/050041 - TISSUE SAMPLE ANALYSIS. European Patent Office (ISA/EP), Netherlands Patent Office, The Hague.

## Curriculum Vitae

**Name:** Elisa Maria Lamego Barroso

**Date of birth:** 18-09-1988

**Nationality:** Portuguese

**Languages:** Portuguese (native), English (B2), Dutch(B1).

**Address:** Weena 951, 3013 AL, Rotterdam, The Netherlands

**You can find me:** linkedin.com and researchgate.net

**Institutional email:** e.barroso@erasmusmc.nl

**Personal email:** elisa\_barroso\_bio@hotmail.com

---

### Scientific Experience:

---

#### May 2013 to May 2018

*Researcher, Molecular Medicine PhD Student: Development of Raman spectroscopy tools for surgery guidance in head & neck oncology. Erasmus MC, University Medical Center Rotterdam, 3015 CE Rotterdam, The Netherlands.*

#### January 2013 to May 2013

*Research Fellow, working on the Project PTDC/EIA-EIA/099458/2008IPATIMUP: Universal evaluation system of diseases based on molecular markers. IPATIMUP (Institute of Pathology and Molecular Immunology from University of Porto), Porto, Portugal.*

#### December 2011 to December 2012

*Research Fellow, working on the Project NOISYRIS - Recognition of Periocular Region. Telecommunications Institute, Covilhã, Portugal.*

#### September 2010 to August 2011

*Research Fellow, working on the Project Bio-computational study of tinnitus. INEGI - Institute of Science and Innovation in mechanical and industrial engineering, Porto, Portugal.*

---

**Other Working Experience:**

---

September 2009 to December 2009

*Biology, Physics and Chemistry Tutor, Centro de Estudos mentes brilhantes, Vila Nova de Famalicão, Portugal.*

April 2009 to June 2009

*Internship at the Department of Facilities and Equipments, EPE - Centro Hospitalar do Tâmega e Sousa, Penafiel, Portugal.*

---

**Education:**

---

May 2013 to May 2018

*PhD, Molecular Medicine at the Erasmus MC, University Medical Center Rotterdam, 3015 CE Rotterdam, The Netherlands.*

From 2009 to 2011

*Master in Biomedical Engineering at the University of Porto - Faculty of Engineering.*

From 2006 to 2009

*Biomedical Engineering degree at the School of Management and Industrial Studies (ESEIG) from Polytechnic Institute of Porto.*

---

**Organizing conferences/events:**

---

*EPIC Biophotonics Workshop - 'Intra-Operative Assessment of Tumor Resection Margins'. 2-3 July 2014, Erasmus Medical Center 'Centrum Locatie' Lecture Hall 3 Wytemaweg 80, Rotterdam, The Netherlands.*

---

**Awards:**

---

*Best Poster award - SPEC 2014 Shedding New Light on Disease - 17-22 August 2014 Krakow, Poland. Towards Raman-guided tumor surgery: discriminating squamous cell carcinoma from healthy tissue based on water content.*

---

**Patents:**

---

*PCT/NL2016/050041 - TISSUE SAMPLE ANALYSIS. 18 January 2016 filed. European Patent Office (ISA/EP), Netherlands Patent Office, The Hague.*

---

**Feature publications:**

---

**E. M. Barroso**, I. ten Hove, T. C. Bakker Schut, H. Mast, C. G. F. van Lanschot, R. W. H. Smits, P. J. Caspers, R. Verdijk, V. Noordhoek Hegt, R. J. Baatenburg de Jong, E. B. Wolvius, G. J. Puppels S. Koljenović. Raman spectroscopy for assessment of bone resection margins in mandibulectomy for oral cavity squamous cell carcinoma. *European Journal of Cancer*. 2018; 92: 77-87.

I. P. Santos, **E. M. Barroso**, T. C. Bakker Schut, P. J. Caspers, C. G. F. van Lanschot, D-H. Choi, M. F. Van der Kamp, R. W. H. Smits, R. Van Doorn, R. Verdijk, V. Noordhoek Hegt, J. H. von der Thusen, C. H. M. van Deurzen, L. B. Koppert, G. J. L. H. van Leenders, P. C. Ewing-Graham, L. C. van Doorn, C. M. F. Dirven, M. B. Busstra, J. A. U. Hardillo, A. Sewnaik, I. ten Hove, H. Mast, D. Monserez, C. A. Meeuwis, T. Nijsten, E. B. Wolvius, R. Baatenburg de Jong, G. J. Puppels, S. Koljenović. Raman spectroscopy for cancer detection and cancer surgery guidance: translation to the clinics. *The Analyst*. 2017;142(17):3025-3047. DOI: 10.1039/C7AN00957G.

**E. M. Barroso**, R. W. H. Smits, C. G. F. van Lanschot, P. J. Caspers, I. ten Hove, H. Mast, A. Sewnaik, J. A. U. Hardillo, C. A. Meeuwis, R. Verdijk, V. Noordhoek Hegt, R. Baatenburg de Jong, E. B. Wolvius, T. C. Bakker Schut, S. Koljenović, G. J. Puppels. Water concentration analysis by Raman spectroscopy to determine the location of the tumor border in oral cancer surgery. *Cancer Research*. 2016; 76(16). DOI:10.1158/0008-5472.CAN-16-1227.

**E. M. Barroso**, R. W. H. Smits, T. C. Bakker Schut, I. ten Hove, J. A. U. Hardillo, E. B. Wolvius, R. Baatenburg de Jong, S. Koljenović, G. J. Puppels. Discrimination between oral cancer and healthy tissue based on water content determined by Raman Spectroscopy. *Analytical Chemistry*. 2015; 87(4):2419-2426. DOI: 10.1021/ac504362y.

**E. M. Barroso**, G. Santos, L. Cardoso, C. Padole, H. Proença. Periocular Recognition: How much facial expressions affect performance? *Pattern Analysis and Applications*. 2015;19(2). DOI: 10.1007/s10044-015-0493-z.

**E. M. Barroso**, G. Santos, H. Proença. Facial expressions: Discriminability of facial regions and relationship to biometrics recognition. *Computational Intelligence in Biometrics and Identity Management (CIBIM)*, 2013, IEEE Workshop on Singapore. Volume: 77-80. DOI: 10.1109/CIBIM.2013.6607918.

**E. M. Barroso**, Z. Ma, J. M. R. S. Tavares, F. Gentil. Computational algorithms for segmentation of the human ear. III *ECOMAS, Thematic Conference on Computational Vision and Medical Image Processing: VipIMAGE 2011*, Olhão, Algarve, Portugal.

